1-1-2013

Imaging and Understanding Atomic-Scale Adhesion and Wear: Quantitative investigations Using in situ TEM

Tevis Jacobs
University of Pennsylvania, tevis@seas.upenn.edu

Imaging and Understanding Atomic-Scale Adhesion and Wear: Quantitative investigations Using in situ TEM

Abstract
The underlying physics governing tribological interactions - adhesion, friction, lubrication, and wear - are poorly understood. Significant progress has been enabled by nanoscale studies using the atomic force microscope (AFM). However, AFM lacks direct access to the contact geometry and structure. In this thesis, nanoscale adhesion and wear tests were performed inside of a transmission electron microscope (TEM), enabling real-time in situ interrogation of the contact in vacuum. Quantitative data was extracted using custom analysis routines to resolve tip shape, volume changes, and adhesive forces with unprecedented resolution.

From in situ adhesion tests, a novel method was developed to extract the work of adhesion (0.66Â±0.14 J/m^2) and range of adhesion (0.25Â±0.06 nm) between silicon and diamond. The latter quantity has not previously been measured experimentally. TEM adhesion tests and complementary atomistic simulations reveal an order-of-magnitude reduction in apparent work of adhesion as tip roughness increased from atomic-scale to a root-mean-square value of 1 nm. Using an existing analytical model, an empirically derived roughness-independent adhesion parameter was extracted. In situ wear tests of silicon on diamond at low load revealed the mechanism of wear to be consistent with atom-by-atom processes. The rate of atomic removal varied exponentially with average normal stress, consistent with stress-mediated chemical reaction kinetics. This yields a physically reasonable activation energy (0.85Â±0.06 eV), and activation volume (6.7Â±0.3 Ã?). This framework can be generalized to understand and potentially predict wear in many materials undergoing atom-by-atom removal.

Together, these investigations advance the scientific understanding of nanoscale adhesion and wear and help bridge the gap between experiments and atomistic simulations. Three examples are demonstrated where nanometer-scale trends can be predicted using continuum approaches: nanoscale adhesive forces can be calculated using an interaction potential; apparent work of adhesion depends on nanoscale root-mean-square roughness; and the rate of atomic-scale wear reactions is determined by the average normal contact stress. These examples, while only demonstrated in the specific systems studied, suggest strategies and future research directions for understanding, predicting, and controlling tribological phenomena.

Degree Type
Dissertation

Degree Name
Doctor of Philosophy (PhD)

Graduate Group
Materials Science & Engineering

First Advisor
Robert W. Carpick

Keywords
Adhesion, AFM, Nanoscale, Roughness, TEM, Wear

Subject Categories
Mechanical Engineering | Mechanics of Materials

IMAGING AND UNDERSTANDING ATOMIC-SCALE ADHESION AND WEAR: QUANTITATIVE INVESTIGATIONS USING *IN SITU* TEM

Tevis David Bartow Jacobs

A DISSERTATION

in

Materials Science and Engineering

Presented to the Faculties of the University of Pennsylvania

in

Partial Fulfillment of the Requirements for the

Degree of Doctor of Philosophy

2013

Supervisor of Dissertation

*Signature*_____

Robert W. Carpick, Professor and Chair, Mechanical Engineering & Applied Mechanics

Graduate Group Chairperson

*Signature*_____

Russell J. Composto, Professor, Materials Science & Engineering

Dissertation Committee

Daniel S. Gianola, Assistant Professor, Materials Science & Engineering

John L. Bassani, Richard H. and S.L. Gabel Professor, Mechanical Engineering & Applied Mechanics

Ju Li, Battelle Energy Alliance Professor of Nuclear Science and Engineering
and Professor of Materials Science and Engineering, Massachusetts Institute of Technology

IMAGING AND UNDERSTANDING ATOMIC-SCALE ADHESION AND WEAR: QUANTITATIVE INVESTIGATIONS USING *IN SITU* TEM

To my family

ACKNOWLEDGMENTS

First and foremost, I wish to thank my advisor, a source of inspiration and guidance throughout the process.

I want to thank Prof. Dan Gianola, Prof. John Bassani, and Prof. Ju Li for serving on my PhD committee and providing scientific guidance and support along the way.

I have far too many other people to thank. I could not have completed this without help from countless people. Here is a short (and partial) list of the many people who have helped me throughout my PhD.

I am grateful for helpful discussions and collaborations with Prof. Kevin Turner. Also, many thanks to Dr. Dave Grierson for scientific discussions and programming assistance. Dr. Doug Yates, Dr. Lolita Rotkina, Dr. Jamie Ford, and Dr. Ryan Major provided a great deal of microscopy and equipment assistance.

Direct scientific and technical assistance with this work was provided by Joel Lefever, Alex Goodman, and Sarah Badin. Graham E. Wabiszewski performed AFM on the indenter tip (Chapter 3) and provided much other technical help. I wish to thank Peter Rockett for help with design, and also manufacturing of the fixture described in Chapter 3.

I wish to thank my qualifying committee, Prof. Vaclav Vitek, Prof. Mahadevan Khantha, Prof. Charles McMahan, and Prof. I-Wei Chen, for challenging me and spurring the creation of the analysis in Chapter 6.

I have been fortunate to have excellent collaborators at various institutions: at the US Naval Academy: Prof. Judith Harrison Dr. Pamela Keating Dr. Kate Ryan, and Dr.

Marcel Fallet; at National Chung Cheng University (Taiwan): Prof. Yeau-Ren Jeng, Dr. Kent Wu; at the Center for Integrated Nanotechnology (Sandia): Dr. Jianyu Hwang, Dr. Jiangwei Wang, Dr. Yang Liu; and at Advanced Diamond Technologies, Inc: Dr. Nicolaie Moldovan, Dr. Hongjun Zeng, and Dr. John Carlisle.

I wish to thank Pat Overend, Vicky Lee, Irene Clements, Maryeileen Griffith, Sue Waddington-Pilder, Olivia Brubaker, and Desirae Johnson for support and much logistical help.

I wish to thank the current, former (and honorary) members of the Carpick Research Group for support, assistance, guidance, and much fun.

Use of the facilities of the Pennsylvania Regional Nanotechnology Facility is acknowledged. Also, funding from the National Science Foundation (Grants CMMI-0826076 and IGERT DGE-0221664) is gratefully acknowledged.

ABSTRACT

IMAGING AND UNDERSTANDING ATOMIC-SCALE ADHESION AND WEAR: QUANTITATIVE INVESTIGATIONS USING *IN SITU* TEM

Tevis D. B. Jacobs

Robert W. Carpick

The underlying physics governing tribological interactions – adhesion, friction, lubrication, and wear - are poorly understood. Significant progress has been enabled by nanoscale studies using the atomic force microscope (AFM). However, AFM lacks direct access to the contact geometry and structure. In this thesis, nanoscale adhesion and wear tests were performed inside of a transmission electron microscope (TEM), enabling real-time *in situ* interrogation of the contact in vacuum. Quantitative data was extracted using custom analysis routines to resolve tip shape, volume changes, and adhesive forces with unprecedented resolution.

From *in situ* adhesion tests, a novel method was developed to extract the work of adhesion (0.66±0.14 J/m^2) and range of adhesion (0.25±0.06 nm) between silicon and diamond. The latter quantity has not previously been measured experimentally. TEM adhesion tests and complementary atomistic simulations reveal an order-of-magnitude reduction in *apparent* work of adhesion as tip roughness increased from atomic-scale to a root-mean-square value of 1 nm. Using an existing analytical model, an empirically derived roughness-independent adhesion parameter was extracted. *In situ* wear tests of silicon on diamond at low load revealed the mechanism of wear to be consistent with atom-by-atom processes. The rate of atomic removal varied exponentially with average

normal stress, consistent with stress-mediated chemical reaction kinetics. This yields a physically reasonable activation energy (0.85±0.06 eV), and activation volume (6.7±0.3 Å). This framework can be generalized to understand and potentially predict wear in many materials undergoing atom-by-atom removal.

Together, these investigations advance the scientific understanding of nanoscale adhesion and wear and help bridge the gap between experiments and atomistic simulations. Three examples are demonstrated where nanometer-scale trends can be predicted using continuum approaches: nanoscale adhesive forces can be calculated using an interaction potential; apparent work of adhesion depends on nanoscale root-mean-square roughness; and the rate of atomic-scale wear reactions is determined by the average normal contact stress. These examples, while only demonstrated in the specific systems studied, suggest strategies and future research directions for understanding, predicting, and controlling tribological phenomena.

TABLE OF CONTENTS

LIST OF TABLES

LIST OF FIGURES

LIST OF SYMBOLS

Latin Characters

A	amplitude of sine wave for artificial roughness
$A_{contact}$	contact area
$A_{1:2}$	Hamaker constant between materials 1 and 2
$a_{contact}$	contact radius
b	Burger's vector
c	constant term
C, D	empirical constants used in the Lennard-Jones interatomic potential
D_0	minimum separation or cut-off distance of the van der Waals potential
d_{slide}	sliding distance
E^*	effective modulus of two materials in contact
E_1, E_2	elastic modulus of two materials in contact
$E_{interaction}$	interaction energy between two atoms
f	frequency
F	force (type indicated by subscript: $F_{adhesive}$, $F_{applied}$, etc.)
H	hardness of material
h	height of AFM tip
h_P	Planck's constant
$K_{Archard}$	dimensionless wear coefficient
$k_{Archard}$	dimensional wear coefficient
k	rate of reaction
k_B	Boltzmann constant
l	lattice constant of a crystalline material
N	number (atoms, defects, etc.)
n	power exponent in a power-law shape
r	cylindrical polar coordinate, radial dimension
R^2	regression coefficient
R_1, R_2, R_{tip}	radius of the body indicated by the subscript
R_a	average surface roughness
R_{eff}	effective radius of two bodies in contact
R_q	root-mean-square surface roughness
T	temperature
t_{slide}	time in sliding contact
v	sliding velocity
v_{track}	velocity of growth of the wear track
V_{lost}	volume removed due to wear
W_{adh}	work of adhesion between two surfaces
z	cylindrical polar coordinate, height dimension
z_0	the equilibrium separation distance between two flat surfaces in contact

Greek Characters

Δ	measured cantilever deflection
ΔA_{act}	activation area
ΔF_{act}	Helmholtz free energy of activation
ΔG_{act}	Gibbs free energy of activation on
ΔS_{act}	activation entropy
ΔU_{act}	activation energy
ΔV_{act}	activation volume
ΔW_{act}	work done during transition from initial state to activated state
δ	contact deformation
ε	strain
θ	angle
λ	wavelength of sine wave for artificial roughness
μ_T	Tabor parameter
τ	shear stress
ν_1, ν_2	Poisson ratio of two materials in contact
ξ	pressure dependence of shear stress
ρ, ρ_{surf}	number density of atoms in a volume, surface, respectively
σ	stress

LIST OF ACRONYMS

AFM	atomic force microscopy
DLC	diamond-like carbon
DMT	Derjaguin-Müller-Toporov contact model
FIB	focused ion beam
GNP	gross national product
JKR	Johnson-Kendall-Roberts contact model
MD	molecular dynamics
MEMS	microelectronic mechanical systems
NEMS	nanoelectronic mechanical systems
RMS	root mean square
SEM	scanning electron microscopy
TEM	transmission electron microscopy
UNCD	ultrananocrystalline diamond

CHAPTER 1: The importance of nanotribology

Tribology is the study of sliding surfaces and related phenomena including friction, adhesion, lubrication, and wear. The study of tribology draws insights from a broad range of disciplines, from physics and chemistry to materials science and mechanical engineering. The lessons learned apply equally broadly: to other scientific fields, such as geology and biology, and to industries from manufacturing and transportation to medical devices and food processing technology. The *study* of tribological topics can be traced back at least 500 years, with diagrams in Leonardo da Vinci's notebooks (*1*). The *use* of tribological concepts dates back much further; wall paintings show ancient Egyptians using greased or rolling contacts to move heavy objects almost 4000 years ago (*2*). Evolution has been "using" these concepts even longer – 85 million year-old fossils of the hadrosaurid dinosaur show evidence that differentially wearing dental structures created self-sharpening teeth (*3*).

The field of tribology was named and its importance fully recognized after a 1966 United Kingdom government report (described in Ref. (*4*)) estimated that a sum of money equal to 4% of gross national product was wasted annually due to friction and wear, and one fourth of that sum could be recovered through greater attention to tribology: friction, adhesion, lubrication and wear. Subsequently, more comprehensive studies have shown it to be true across many countries and have *increased* the recoverable estimate to roughly 1.5% of GNP (*5*) or more than 100 billion dollars annually in the US alone. These reports motivated significant research activity, and entire scientific journals, professional societies, and annual national and international meetings

are devoted to research in the field. Enormous progress has been made in the measurement and control of systems with sliding interfaces; an example success story is the automobile industry, where improvements in material selection, component design, and engine operating conditions resulted in a 25% increase in average fuel economy between 1980 and 2005, despite an almost 100% increase in average horsepower over the same period (*6*).

1-1: Motivation for the study of nanotribology

Much of the aforementioned progress, however, has been enabled through trial-and-error, empiricism, and the creation and use of phenomenological laws. The interaction of two bodies making contact and/or sliding will be governed by the complex interaction of a large number of physical parameters: the composition, material properties, and bulk shape of the two bodies forming the contact; the topography, chemistry, crystallinity and even identity (if oxidized, contaminated, or passivated) of the surfaces of those bodies; the sliding conditions (speed, normal load, direction); and the environment (air, vacuum, lubricant). Further, the interface is evolving dynamically, as bonds can form across the interface, deformation and wear can change the geometry of the bodies, and material removal or the formation of "tribo-layers" can even change the identity of the materials in contact. While significant advances in models and experiments were made during the 1930s and 1940s by Bowden and Tabor (*7*) (for instance, the realization that friction can be modeled as scaling with the *true* area of contact), the field of tribology has suffered from a lack of fundamental, physics-based

models in tribology. To this day, there are *no* models that can predict friction coefficients or wear rates from first principles (*8*) – despite considerable economic motivation and scientific effort.

One promising path to create fundamental models for tribology is to study contact at the nanometer-scale. It has long been known that nearly all real macroscopic surfaces are rough, and so the contact of two apparently flat bodies occurs at only a relatively small number of local high points, or *asperities*. To further complicate the contact, roughness occurs over many length scales, with "protuberances on protuberances on protuberances" (*9*) or fractal-like structures; thus, the actual geometries of contact may be orders of magnitude smaller than the apparent dimensions of the bodies. This fractal-like behavior is limited in the small wavelength by the discrete nature of atoms. Therefore, the fundamental behavior of even micro- and macro-scale contacts is typically governed by nanoscale asperity contacts, and by atomic-scale processes that occur at these contact points.

Recent scientific and industrial progress at the nanoscale has enabled direct experimental studies of nanoscale single asperities. Most significantly for tribology is the development, proliferation, and diversification of atomic force microscopy – which measures the interaction between a sharp nanoscale asperity and nearly any surface of interest. The atomic force microscope (AFM) can easily measure forces with piconewton resolutions and can resolve topography on the picometer scale (*10*) – in some modes resolving the atomic lattice (*11*) or even single molecules (*12*). Further, it can be performed with precisely controlled sliding velocity, well-characterized surfaces, and controlled environments such as dry nitrogen, liquid, or ultra-high vacuum. This has

enabled unprecedented resolution of and control over all of the many variables associated with a sliding contact. This allowed the careful variation of a small number of variables to determine their action, and has facilitated numerous breakthrough investigations in single-asperity friction, adhesion, and wear (as reviewed, for example, in Ref. (*13*)).

Examples of scientific breakthroughs enabled by the AFM include (among many others): the demonstration (*14*) of Bowden and Tabor's concept of friction scaling with true area of contact (discussed above); the direct measurement of intramolecular and intermolecular forces in organic proteins (*15*); and the determination of the effect of atomic corrugation on friction and the demonstration of "superlubricity" (*16*). Examples of commercial successes include the hard disk industry, where AFM-based studies led to precisely designed surface roughness and improved materials selection to enable exponential progress in areal storage density (*6*), and also microelectronic mechanical systems (MEMS), where AFM-based insights enabled the solution of adhesion and release problems with microfabricated accelerometers, gyroscopes, and active-mirror projectors (*6*).

At the same time, advances in computing power and the development of atomistic simulation techniques have enabled similar problems of nanometer-scale asperities making contact and sliding to be studied using simulations (as reviewed, for example, in Ref. (*17*). Experiments performed at the nanoscale have the additional benefit of being able to be directly compared against these simulations for complementary studies that yield even more accurate, generalizable, and physically realistic data than either can in isolation.

In summary, the investigation of a single, sliding contact at the nanoscale presents one of the most promising pathways to fundamental, predictive, scientific models of adhesion, friction, and wear at all length scales. However, while the atomic force microscope has enabled unprecedented resolution and control of all variables associated with sliding contact, it does not enable direct visualization or investigation of the contact itself. This problem is common to tribological testing at all length scales, and requires additional complementary analysis techniques to provide a fuller understanding of the nature of contact.

1-2: Motivation for in situ *investigations into tribology at the nanoscale*

In addition to all the complexities of tribological contacts that were discussed in Sect. 1-1, the contacting interface is – by definition – buried between two bodies, which further complicates observation and investigation. As will be discussed in Chapters 2 and 3, this problem is often solved by performing a contact or sliding test using one apparatus (a pin-on-disk tribometer or an AFM, for example) then removing one or both surfaces from the apparatus and taking them to an external microscope or spectroscope for analysis, typically exposing them to air or some alternate environment in the process. Investigations using this *ex situ* investigation approach have yielded very useful information, but are fundamentally limited by not knowing which phenomena were caused by sliding, and which others occurred during the removal, transfer, and insertion into the subsequent characterization tool. Additionally, once removed from the tribological test apparatus, it can be quite difficult to find the exact location of sliding,

and it is nearly impossible to remount the surfaces in the same positions and orientations for continuation of the test after examination without a disruptive effect. More recently, various researchers have incorporated a microscopy or spectroscopy technique into the tribological testing apparatus (*8*). These *in situ* investigations evaluate the surfaces in real time either by collecting data when the surfaces are not in contact (but without interruption of the test or change of environment) (for example, Refs. (*18*, *19*)) or while the two surfaces are in direct contact (for example, Refs. (*20*, *21*)).

The investigations presented in this thesis use both types of *in situ* investigations. As will be discussed in Chapter 3, the tribological test apparatus used here is similar in function to an atomic force microscope, but the surfaces are mounted inside of a transmission electron microscope. In this way, real-time video can be captured of the surfaces in contact, to monitor contact forces, observe dynamic events such as snap-in and pull-off, and to directly observe mechanisms of wear, such as fracture, the formation of debris, or plastic deformation. Yet this real-time video must be low-enough magnification to observe the full range of motion, and also the motion of sliding and vibration of the apparatus reduce the resolution that is possible. Therefore, in addition, the contact can be separated without breaking the vacuum or changing the test conditions to take higher resolution images in which the sub-surface atomic lattice of crystalline materials is easily visible. Once out of contact, the characterization tools of analytical electron microscopy can be used to probe the identity, structure, and bonding state of materials.

The materials chosen for investigation in the present investigations are silicon, diamond-like carbon (DLC), and ultrananocrystalline diamond (UNCD). Silicon was

chosen because of its technological relevance and extensive prior study. As the foundational material for the semiconductor industry, it has been extensively characterized: including its material and mechanical properties and its deformation mechanisms. Additionally, it is the most common material used in micro- and nanoelectronic mechanical systems (MEMS/NEMS) and other devices such as atomic force microscopy probe tips. Diamond-like carbon coatings were chosen for study because they have gained extensive use as hard, wear resistant materials in devices such as hard disks (*6*). They are also being used or considered for use in a wide variety of applications as protective coatings (*22*) from car engines to razor blades. Ultrananocrystalline diamond was chosen because it is a promising coating material that has properties such as stiffness, hardness, and inertness that approach those of single crystal diamond, yet can be conformally coated onto components (*23*). While its use is not as widespread as DLC, it is considered to be a promising material for use in a variety of applications such as MEMS devices with sliding contacts and scanning probe microscopy probes (*24*, *25*).

1-3: Structure of the present thesis

This thesis begins by describing in Chapter 2 relevant prior literature on adhesion and wear at the nanoscale, highlighting key results from numerical and experimental investigations – both *in situ* and *ex situ*. The experimental tools and analysis techniques used to investigate adhesion and wear are described in Chapter 3, including details of the *in situ* test apparatus, and a description of the models used and calculations performed.

Chapters 4 and 5 describe *in situ* TEM adhesion testing and its analysis to uncover the fundamental physics governing adhesion at the nanoscale. Specifically, in Chapter 4, a novel analysis method is applied to adhesion tests performed with detailed tip characterization to uncover fundamental parameters governing adhesion, which had not previously been experimentally accessible. In Chapter 4, similar adhesion tests are analyzed in the context of tip topography to demonstrate the effect of nanometer- and sub-nanometer-scale roughness on the adhesion of sharp tips, such as those used for probe-based microscopy and manufacturing. Chapters 6 and 7 describe advances in the modeling and prediction of gradual, atom-by-atom wear at the nanoscale. Chapter 6 reframes a previously proposed model of wear based on reaction rate kinetics; a case study of reaction rate theory is reviewed in detail, then insights from this case study are directly applied to nanoscale wear. Then, building on insights from the previous chapter, Chapter 7 describes the application of reaction rate theory to wear tests performed and characterized inside the TEM, and the extraction of the fundamental parameters governing wear of silicon. Finally, conclusions drawn from the previous chapters are discussed in Chapter 8, along with suggested future lines of inquiry.

1-4: References

(1) Marder, M. Friction: Terms of detachment. *Nature Materials* **2004**, *3*, 583–584.
(2) Dowson, D. *History of Tribology*; 2nd ed. Wiley: New York, NY, 1998.
(3) Erickson, G. M.; Krick, B. A.; Hamilton, M.; Bourne, G. R.; Norell, M. A.; Lilleodden, E.; Sawyer, W. G. Complex dental structure and wear biomechanics in hadrosaurid dinosaurs. *Science* **2012**, *338*, 98–101.
(4) Jost, H. P. Tribology: the first 25 years and beyond-achievements, shortcomings and future tasks. *Industrial Lubrication and Tribology* **1992**, *44*, 22–7.
(5) Jost, H. Tribology—Origin and future. *Wear* **1990**, *136*, 1–17.
(6) Mate, C. M. *Tribology on the Small Scale: A Bottom Up Approach to Friction, Lubrication, and Wear*; Oxford University Press: Oxford, UK, 2008.
(7) Bowden, F. P.; Tabor, D. *The Friction and Lubrication of Solids*; Oxford university press, 2001; Vol. 1.
(8) Sawyer, W. G.; Wahl, K. J. Accessing Inaccessible Interfaces: In Situ Approaches to Materials Tribology. *MRS Bull.* **2008**, *33*, 1145–1148.
(9) Archard, J. F. Elastic deformation and the laws of friction. *Proc. Roy. Soc. A* **1957**, *243*, 190–205.
(10) Meyer, E.; Hug, H. J.; Bennewitz, R. *Scanning Probe Microscopy: the Lab on a Tip*; Springer, 2003.
(11) Lee, C.; Li, Q.; Kalb, W.; Liu, X. Z.; Berger, H.; Carpick, R. W.; Hone, J. Frictional characteristics of atomically thin sheets. *Science* **2010**, *328*, 76–80.
(12) Gotsmann, B.; Schmidt, C.; Seidel, C.; Fuchs, H. Molecular resolution of an organic monolayer by dynamic AFM. *European Physical Journal B* **1998**, *4*, 267–268.
(13) Carpick, R.; Salmeron, M. Scratching the surface: Fundamental investigations of tribology with atomic force microscopy. *Chem. Rev.* **1997**, *97*, 1163–1194.
(14) Carpick, R. W.; Agrait, N.; Ogletree, D. F.; Salmeron, M. Measurement of interfacial shear (friction) with an ultrahigh vacuum atomic force microscope. *J. Vac. Sci. Tech. B* **1996**, *14*, 1289–1295.
(15) Rief, M.; Oesterhelt, F.; Heymann, B.; Gaub, H. E. Single molecule force spectroscopy on polysaccharides by atomic force microscopy. *Science* **1997**, *275*, 1295–1297.
(16) Dienwiebel, M.; Verhoeven, G.; Pradeep, N.; Frenken, J.; Heimberg, J.; Zandbergen, H. Superlubricity of Graphite. *Phys. Rev. Lett.* **2004**, *92*, 126101.
(17) Szlufarska, I.; Chandross, M.; Carpick, R. W. Recent advances in single-asperity nanotribology. *J. Phys. D* **2008**, *41*, 123001.
(18) Korres, S.; Dienwiebel, M. Design and construction of a novel tribometer with online topography and wear measurement. *Rev. Sci. Instrum.* **2010**, *81*, 063904.
(19) Argibay, N.; Bares, J. A.; Sawyer, W. G. Asymmetric wear behavior of self-mated copper fiber brush and slip-ring sliding electrical contacts in a humid carbon dioxide environment. *Wear* **2010**, *268*, 455–463.
(20) Ovcharenko, A.; Halperin, G.; Etsion, I. In situ and real-time optical investigation of junction growth in spherical elastic–plastic contact. *Wear* **2008**, *264*, 1043–1050.
(21) Wahl, K. J.; Sawyer, W. G. Observing interfacial sliding processes in solid-solid contacts. *MRS Bull.* **2008**, *33*, 1159–1167.
(22) Robertson, J. Diamond-like amorphous carbon. *Mater. Sci. Eng.: R: Reports* **2002**, *37*, 129–281.
(23) Espinosa, H.; Prorok, B.; Peng, B.; Kim, K.; Moldovan, N.; Auciello, O.; Carlisle, J.; Gruen, D.; Mancini, D. Mechanical properties of ultrananocrystalline diamond thin films relevant to MEMS/NEMS devices. *Exp. Mech.* **2003**, *43*, 256–268.
(24) Krauss, A. R.; Auciello, O.; Gruen, D. M.; Jayatissa, A.; Sumant, A.; Tucek, J.; Mancini, D. C.; Moldovan, N.; Erdemir, A.; Ersoy, D. Ultrananocrystalline diamond thin films for MEMS and moving mechanical assembly devices. *Diamond and Related Materials* **2001**, *10*, 1952–1961.

(25) Liu, J.; Grierson, D.; Moldovan, N.; Notbohm, J.; Li, S.; Jaroenapibal, P.; O'Connor, S.; Sumant, A.; Neelakantan, N.; Carlisle, J. Preventing nanoscale wear of atomic force microscopy tips through the use of monolithic ultrananocrystalline diamond probes. *Small* **2010**, *6*, 1140–1149.

CHAPTER 2: Adhesion and Wear at the Nanoscale – A Review

Despite hundreds of years of study on adhesion, friction, and wear, the field of tribology is undergoing rapid and fundamental expansion; as discussed, this is made possible by the convergence of nanotechnology, increases in microscopy (and particularly *in situ* techniques), and expanding computational and simulation capability. For example, while Leonardo da Vinci uncovered the basic trends of friction in the fifteenth century (*1*), it is only in the last two decades that we have made the nanoscale observations to prove why this behavior should hold (see, for example, Ref. (*2*). Likewise, the last few decades have brought major advances in the fields of adhesion and wear, with very significant results arising from simulations and experiments of nanoscale contacts. Therefore these recent advances will be reviewed here, both as context for the present investigations and also as standards by which the present results can be compared.

2-1: Structure of the present chapter

While this thesis focuses on adhesion and wear at the *nanoscale*, Sect. 2-2 presents a very brief review of the models from traditional continuum contact mechanics, starting with simple models of two spheres in contact, then moving to continuum models of more complex geometry. This section on continuum results is included for two reasons: first, because there are certain cases where trends and prediction from continuum mechanics *do* hold true at the nanoscale; and second, because even in cases where continuum trends breakdown, there exist no other well-established models to compare

against. Section 2-3 presents literature on rough surfaces and the effect of roughness on adhesion. Section 2-4 briefly reviews significant results from macro-scale wear, then goes on to discuss in detail nanoscale wear studies performed using the atomic force microscope. Finally, Sect. 2-5 presents prior investigations into nanoscale wear that have used complementary *ex situ* and *in situ* techniques to directly image the contacting bodies.

2-2: Relevant results from continuum contact mechanics

2-2-1: The importance of continuum results in a discussion of nanoscale contacts

There is no reason to assume that continuum models should apply at the nanometer length scale. These models assume that bodies can be treated as continuous media with smooth surfaces, in which stresses and strains are well defined and smoothly varying. As contacting bodies scale down to nanometer dimensions, atomic-scale detail becomes relevant and these underlying assumptions almost certainly break down. Indeed, nanoscale experiments and simulations into the application of continuum predictions have yielded mixed results. Luan and Robbins (*3*, *4*) have shown, using atomistic simulations of bodies in contact, that continuum trends may or may not apply depending on the atomic arrangement at the surface. For instance, regarding the normal pressure inside the contact as a function of radius (shown in Fig. 2.1), they show that continuum predictions do the following: apply nearly perfectly for a bent crystal in commensurate contact; accurately describe *average* behavior for a bent crystal in

incommensurate contact or an amorphous surface; and are categorically incorrect for a stepped crystal. Likewise, Mo *et al.* (*5*, *6*) used atomistic simulations to show that friction of nanoscale contacts is well-described by continuum contact mechanics predictions in cases of high adhesion, where as the agreement is poor for non-adhesive contacts. Finally, Carpick *et al.* (*7*) showed that an atomic force microscope tip sliding on mica obeys the continuum contact mechanics prediction of the real contact area (the matching continuum model is discussed more fully in Ref. (*8*)). In summary, the trends predicted by continuum models may or may not hold in nanoscale contacts, but cannot be automatically assumed to do so.

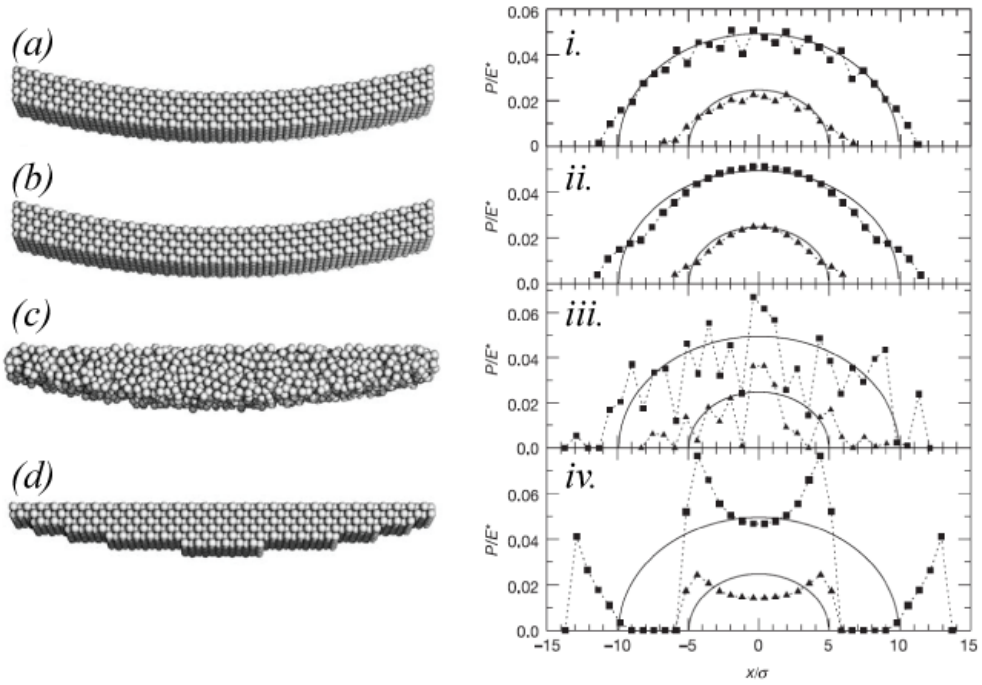

Figure 2.1: Pressure distributions in nanoscale contacts obey predictions of continuum contact mechanics in some cases, and deviate significantly in others; the difference appears to arise due to atomic-scale surface detail. These results represent atomistic simulations performed on four different cases of nanoscale contacts. The pressure distribution with position in the contact is shown for contact between the crystal shown (a-d) and a flat crystal substrate of the same material; two different loads are shown for each case. Pressure distributions are shown for: (i), a bent crystal (a) brought into incommensurate contact; (ii), a bent crystal (b) brought into

commensurate contact; (iii), an amorphous crystal; and (iv) a stepped crystal. In this figure only, P represents local surface pressure, x represents position in the contact, which is normalized by σ, the atomic diameter. Figure reproduced with permission from Ref. (*4*).

Unfortunately, however, no firmly established, generally agreed-upon replacement models exist for adhesion, friction, or wear at the nanoscale. This represents a general problem: except in limited cases of first-principle atomistic simulations, *some* model is needed either to compare results against or to compute the values of needed intermediate parameters (stress, contact area, deformation, etc.). Therefore, in many investigations that are on the frontier of research into nanoscale phenomena (such as those reviewed in Ref. (*9*), and also the present thesis), continuum predictions are used as a first approximation. It is understood that they may be in error. In cases where measured results do not agree, this demonstrates where novel models are needed. In cases where physically reasonable results *are* calculated using continuum predictions, then further work is required to determine why those predictions hold and to determine their range of applicability. In conclusion, continuum mechanics is used at various points in this thesis, either for calculation of values or for comparison; as shown in the ensuing chapters, in some cases it works well, in other cases it does not.

2-2-2: Relevant results from sphere-on-sphere continuum contact mechanics[1]

The contact mechanics of two bodies being pressed together and pulled apart, and the corresponding behavior of the contact area, contact stiffness, deformations, stresses, and strains, have been actively investigated at least since 1881 (*10*). The details of these models are beyond the scope of this thesis and can be found in Ref. (*11*), with a concise review presented in Ref. (*12*). Thus, only the most salient results are presented here.

Based on geometric considerations and the theory of elasticity, the Hertz analysis (*10*) showed that when two non-adhesive spheres of radii R_1 and R_2 are pressed into contact with a loading force $F_{applied}$ (as shown in Fig. 2.2), the region around the contact deforms, with the center displacing by an amount δ in the normal direction, and forming a circular contact area $A_{contact}$ having radius $a_{contact}$, as given by (*11*):

$$a_{contact} = \left(\frac{3F_{applied}R_{eff}}{4E^*} \right)^{1/3}, \tag{2.1}$$

$$\delta = \frac{a_{contact}^2}{R_{eff}} = \left(\frac{9F_{applied}^2}{16R_{eff}E^{*2}} \right)^{1/3}. \tag{2.2}$$

The effective radius R_{eff} and the effective modulus E^* are defined as

$$R_{eff} = \left[\frac{1}{R_1} + \frac{1}{R_2} \right]^{-1}, \tag{2.3}$$

[1] Portions of this section appear in print. Adapted with permission from Jacobs, T. D. B.; Mate, C. M.; Turner, K. T.; Carpick, R. W. Understanding the tip-sample contact: An overview of contact mechanics at the nanoscale. Invited chapter for the book Scanning Probe Microscopy for Industrial Applications: Nanomechanical Characterization. D. G. Yablon, Ed. Wiley, New York, NY. IN PRESS. (Expected, 2013.).

$$E^* = \left[\frac{1-\nu_1^2}{E_1} + \frac{1-\nu_2^2}{E_2} \right]^{-1}, \tag{2.4}$$

where E is Young's modulus, ν is the Poisson ratio, and subscripts 1, 2 designate the different spheres. It should be noted that the mathematics of Hertz's famous equations (and subsequent models described in this chapter) describe a paraboloid of revolution rather than a sphere, but these shapes are approximately equivalent in the limit where the body radius is large relative to the contact radius (as discussed explicitly in Ref. (*13*)). For the remainder of the chapter, they will be referred to as "spheres" in accordance with the original models.

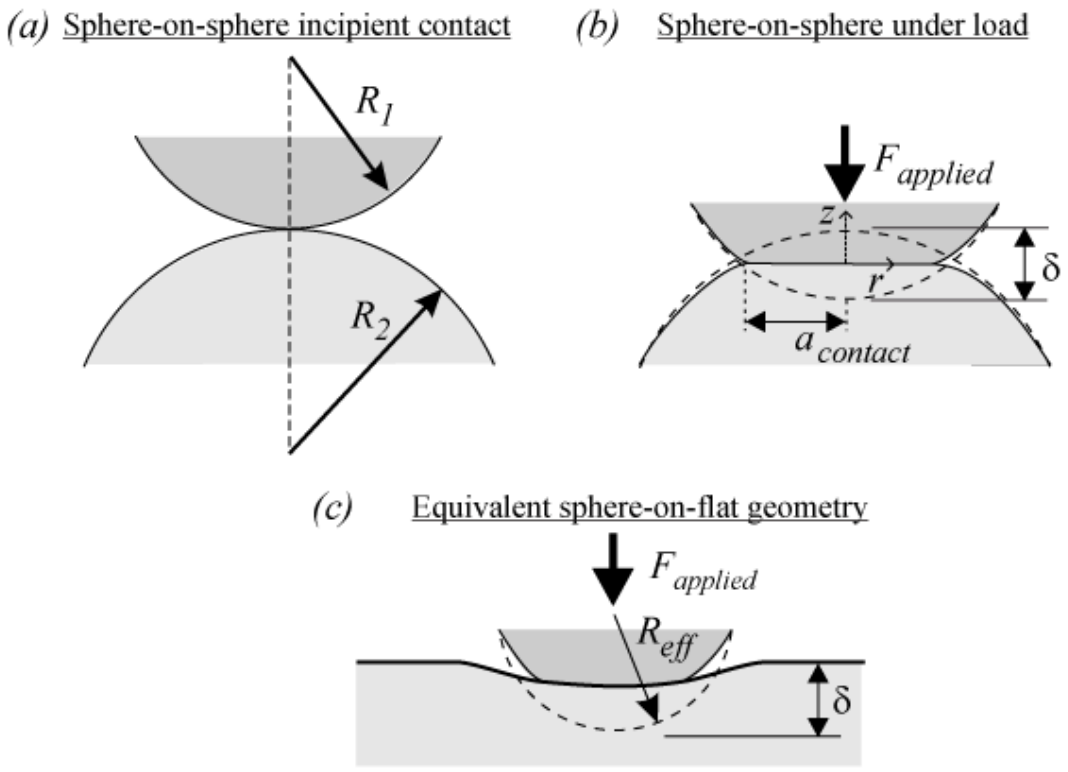

Figure 2.2: The Hertz model describes non-adhesive contact between two spheres using continuum contact mechanics. Two spherical protrusions are shown in side view when they are just touching (a). In (b), the two protrusions are pressed together with a vertical loading force $F_{applied}$ to generate a circular contact area with radius $a_{contact}$ and area $A_{contact} = \pi a_{contact}^2$ due to elastic deformation. The total elastic deformation normal to the contact area is δ. The axes *r, z* (used in subsequent equations) are indicated, with an origin at the center of the contact. The dashed lines show the undeformed profiles of the protrusions. Note that the extent of compression has been significantly exaggerated in this figure for clarity, see Sect. 2.1 for limits of applicability of the Hertz model. A sphere-on-flat geometry (c), in which the sphere has radius R_{eff} (defined in Eq. 2.3), has identical stress and displacement profiles to the case shown in (b).

Initial results for adhesive spheres came from Bradley (*14*) for rigid spheres, and for elastic spheres from two separate groups: Derjaguin, Müller and Toporov (DMT) (*15*) and Johnson, Kendall and Roberts (JKR) (*16*). Derjaguin *et al.* used a standard Hertzian solution with the adhesive load arising from a uniformly distributed adhesive stress,

which effectively acts only to increase the total contact load beyond the applied value. Thus, Eqs. 2.1-2.4 still apply, with $F_{applied}$ replaced by $F_{total} = F_{applied} + F_{adhesive}$. Johnson *et al.* (*16*) used an energy balance approach to model pull-off as a crack-like separation of the two materials. This results in a new set of equations, related to but different from those of Hertz. Both models make well-defined predictions for the spatial distribution of stresses, and for the total load and contact area as a function of deformation, as shown in Fig. 2.3.

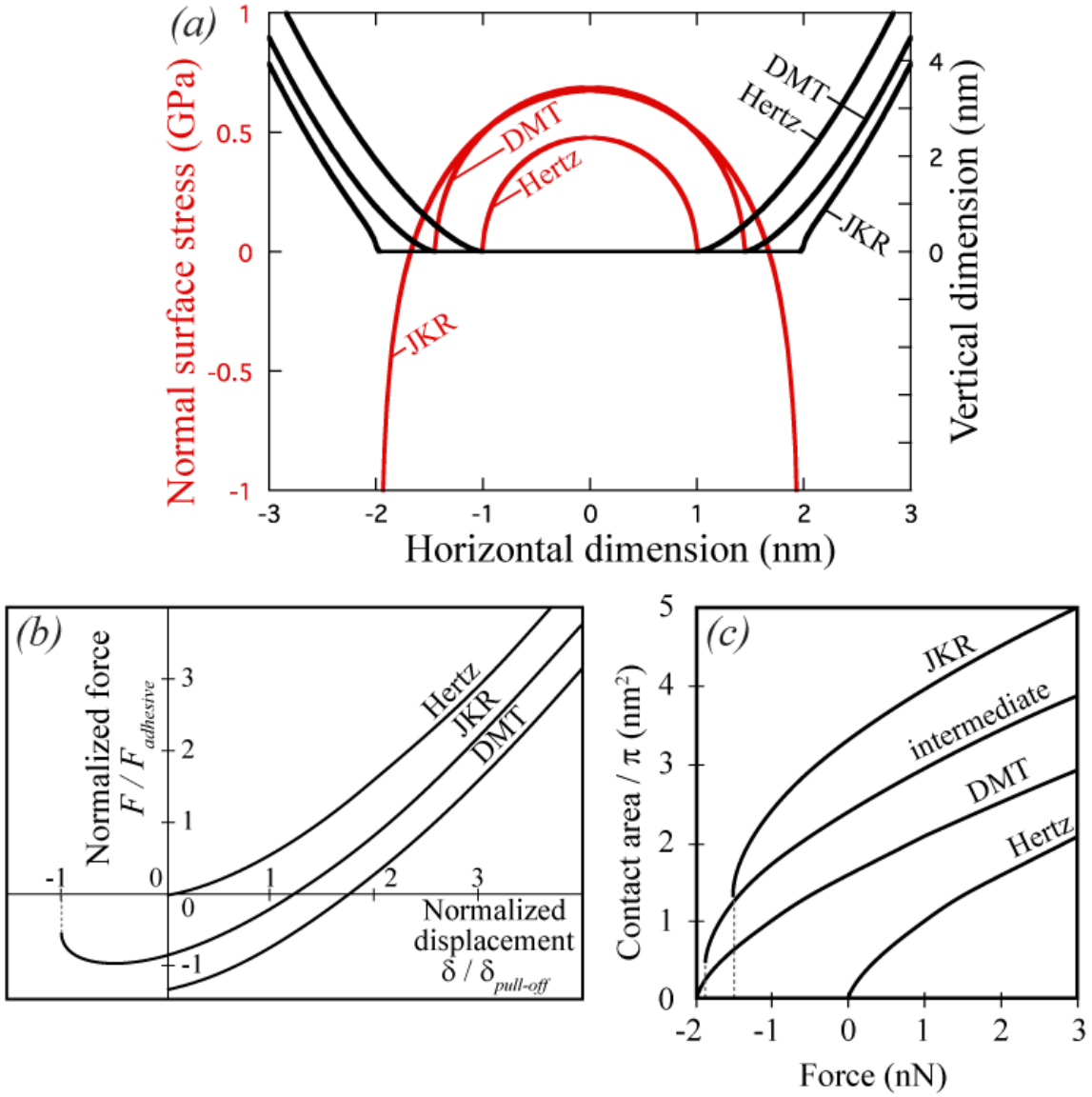

Figure 2.3: Continuum mechanics models have been developed to describe contact in the presence of adhesion. (a) Three different deformed profiles of a spherical tip are shown in black, as predicted by the Hertz, DMT, and JKR models. The corresponding stress profiles under the tip are shown in red for each case. (b) Normalized load is shown as a function of displacement for the non-adhesive (Hertz) case, as well as for both limits of the adhesive case (JKR and DMT). All loads are normalized by the JKR pull-off force; displacements are normalized by the displacement at the pull-off point in the JKR model. (c) The contact area is shown as a function of load for all three models, as well as for an example contact from the intermediate region between JKR and DMT. It is assumed that R_{eff} = 1 nm, E = 0.75 GPa, and W_{adh} = 0.318 J/m^2. The image in (c) is reproduced with permission from Ref. (*17*).

There are several key differences between the DMT and JKR models. The DMT model assumes that the normal stress inside the contact is everywhere compressive, that the additional deformation of the body due to adhesion is small and delocalized, and that the contact area goes smoothly to zero during pull-off. In contrast, the JKR model assumes that the stress towards the outside of the contact is highly tensile (with a singularity at the outermost edge), that the deformation caused by adhesion is non-uniform and most significant towards the edge of contact, and that the contact area is still finite immediately prior to contact separation. Another difference is the specific predicted value of the adhesive force $F_{adhesive}$ where:

$$F_{adhesive,DMT} = 2\pi R_{eff} W_{adh}; \qquad F_{adhesive,JKR} = \frac{3}{2}\pi R_{eff} W_{adh} \text{,} \tag{2.5; 2.6}$$

where the work of adhesion W_{adh} represents the energy per unit are required to separate two flat surfaces from contact to infinite separation.

While the DMT and JKR models were initially believed to be in conflict, Tabor (*18*) recognized that the differences in behavior could be described as two ends of a continuum. He defined a transition parameter μ_T, later designated the Tabor parameter:

$$\mu_T = \left(\frac{R_{eff} W_{adh}}{E^{*2} z_0^3} \right)^{1/3} . \tag{2.7}$$

The parameter z_0 is the equilibrium separation between the two materials. For the remainder of this thesis, the parameter z_0 will be called – in accordance with J. A. Greenwood (*13*) – the "range of adhesion"; this is because for realistic models of adhesion between surfaces (such as the Lennard-Jones interatomic potential (*19*), discussed in Sect. 2-2-3), the equilibrium separation *determines* the length scale of the

adhesion interaction. Tabor's parameter compares the elastic deformation caused by adhesion against the range of action of adhesion. For soft, highly adhesive materials, the former term dominates (large values of μ_T) and the JKR model applies. For stiff, low-adhesion materials, the latter term dominates (small μ_T) and the DMT model applies. Maugis (*20*) later proved Tabor's conclusions analytically and demonstrated a spectrum of behavior for intermediate conditions. The Maugis parameter (equal to $1.16\mu_T$) can be used to determine approximate limits of applicability, with values below 0.1 corresponding to the DMT regime, values above 5 corresponding to the JKR regime, and all other values falling into the "intermediate" regime.

2-2-3: Modeling adhesion for non-spherical geometries

It is common in adhesive contact mechanics to integrate a general adhesion interaction law (defining surface forces as a function of separation distance) over the geometry of the surfaces in contact. In his analytical study, Maugis (*20*) described the adhesion of two contacting spheres (modeled mathematically as paraboloids). He used principles from fracture mechanics, but with the addition of adhesion between parts of the spheres that were *near to* contact, but not *in* contact. To determine the adhesive stress acting at any point, he defined an *interaction potential*, a function that determines the force per unit area acting between two opposing differential elements of surface for any value of separation distance between those elements. He used the simplest possible interaction potential: the square well or "Dugdale" potential, shown in Fig. 2.4(a), where the adhesive stress has a constant value below a critical separation and is zero otherwise.

As Maugis describes, the Dugdale potential was used to simplify the mathematics, whereas the actual adhesive interaction potential is better described by a Lennard-Jones interaction potential (*21*) (shown in Fig. 2.4(c)).

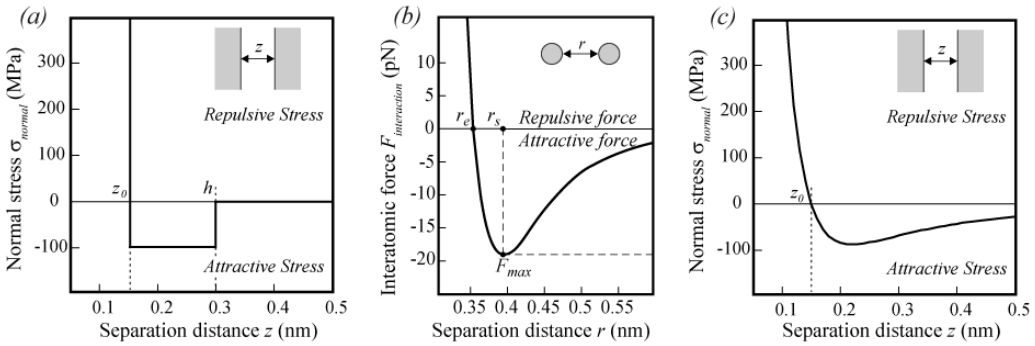

Figure 2.4: An interaction potential defines the adhesive force between two bodies as a function of separation distance. A simple square-well potential is shown in (a), equivalent to the one used by Maugis (*20*). A more realistic surface interaction potential is based on the Lennard-Jones 6-12 *interatomic* surface potential (shown in (b)). The interatomic potential can be integrated to yield the functional form of the Lennard-Jones 3-9 *surface* potential (c). Either (a) or (c) can be integrated element-by-element over the surface of two bodies that are in or near contact, this yields the total force acting between the two bodies.

The physical form of the *Lennard-Jones 3-9 surface potential* is motivated by the Lennard-Jones interatomic potential, defined as:

$$F_{interaction}\left(r\right) = -\frac{dE_{interaction}\left(r\right)}{dr} = -24C\left[\frac{D^6}{r^7} - \frac{2D^{12}}{r^{13}}\right], \tag{2.8}$$

where C and D are empirical parameters used to scale the strength (C) and length scale (D) of the interaction that describes the force between atoms separated by a distance r, as shown in Fig. 2.4(b). While the first term ($\propto r^{-7}$) was physically derived based on van der Waals interactions, the second term ($\propto r^{-13}$) arose from choosing a convenient mathematical expression for the repulsive energy. The net Lennard-Jones energy or force between two bodies can then be calculated by integrating Eq. 2.8 over the volumes of the

two bodies. For two parallel surfaces separated by a distance z, the normal stress σ_{normal} acting between the two surfaces can be integrated straightforwardly (as was done in Ref. (*22*)). The result is commonly written in the following form (*13*):

$$\sigma_{normal}(z) = \frac{F_{surfaces}}{A_{surfaces}} = -\frac{8W_{adh}}{3z_0}\left[\left(\frac{z_0}{z}\right)^3 - \left(\frac{z_0}{z}\right)^9\right], \tag{2.9}$$

and is plotted in Fig. 2.4(c). Equation 2.9 demonstrates the point made in Sect. 2-2-1 that the length scale of the adhesive interaction is a function of the equilibrium separation z_0 and, for this reason, z_0 is referred to in this thesis as the "range of adhesion". Note that the Lennard-Jones 3-9 surface potential (Eq. 2.9) is not typically written in terms of the constants C and D from Eq. 2.8. In accordance with the approach used by Maugis, many authors (*12*, *13*, *22-26*) have integrated the Lennard-Jones 3-9 surface potential over a wide variety of geometries (spheres, paraboloids, power-law shapes, etc.) to determine the total force of attraction acting between two bodies.

The approach of using a surface potential (defined for two infinite flat surfaces) and integrating it, element by element, over an arbitrary geometry relies on the so-called *Derjaguin approximation* (as discussed in Ref. (*21*)). This assumes that the local contribution of *body forces* can be approximated by a local contribution of *surface stresses*. This is mathematically exact for infinite flat planes, but becomes less clear as the in-plane size of a differential element of surface shrinks to the size scale of the separation distance. Further, it neglects any tangential component of surface stress, thus assuming that two curved or angled surfaces have equivalent interaction to two flat, co-planar surfaces at the same value of separation. These assumptions have been shown to be inexact but reasonable as long as one of the bodies is flat (*27*). Moreover, this

integration approach has been very widely used in prior investigations and models at the macroscale (see, for example, Chapters 13-17 of Ref. (*21*)) and microscale (see, for example, Ref. (*28*)). Therefore, it will be used in the present thesis (Chapter 4) and, as with all other continuum concepts, will be used with caution.

2-2-4: The generality of measurements of work of adhesion and range of adhesion, and the difficulty of their measurement

The calculated values obtained by integrating a surface potential over the shape of a body have been shown to be relatively insensitive to the precise form of the assumed potential. Various authors have generalized Maugis' results using different potentials including van der Waals (or exponentially shaped) adhesion with hard-wall repulsion (*29*), a Lennard-Jones 3-9 surface potential (*12*, *26*), and an artificial triangular potential (*26*). The results (on spheres and also on other shapes) show a strong dependence on the length scale and integrated area of the potential, but a relatively small effect on the exact form of the potential. Therefore, in modeling and testing adhesive contacts, the chosen values of the adhesion parameters (W_{adh}, z_0) are more important than the assumed shape of the underlying potential.

The advantage of this insight is that results calculated using these methods are generalizable and relatively insensitive to errors in approximating the correct form of the underlying potential. The disadvantage of this insight is that it is not clear what values of (W_{adh}, z_0) should be used as inputs into the potential. For the strict Lennard-Jones case (van der Waals attraction, Pauli repulsion), the parameters (W_{adh}, z_0) can be

mathematically defined in terms of (C, D) in Eq. 2.8 (as is done in Ref. (*30*)). However, in the general case, there are additional components of attraction and repulsion that will cause deviations away from these values.

The difficulty of measurement and estimation of W_{adh} and z_0 represents a significant limitation of this interaction potential approach. Pull-off forces can be measured experimentally, but for any shape other than a perfect paraboloid, the pull-off force varies with *both* work of adhesion W_{adh} and range of adhesive z_0. So, while many analytical models (for example, Refs. (*25*, *31*)) can predict the equation for pull-off force as a function of these two variables, it is common to *assume* a value for one (usually z_0) and then calculate a value for the other based on the experimental measurement. As discussed further in Chapter 4, it is common to approximate z_0 based on intuition and order of magnitude arguments. As of yet, there are no demonstrated methods for reliably measuring this parameter experimentally.

2-2-5: Concluding remarks about continuum contact mechanics and the use of adhesion potentials

As shown in this section, there is a rich body of literature describing all aspects of contact between continuum bodies. Well-established, experimentally validated models make specific predictions for the contact area, contact stiffness, deformations, stresses, and strains for spheres in contact. The generalization of these models to contacts between bodies of arbitrary geometries is on equally firm footing. Less well established is the range of applicability of these models, and the modifications (if any) to

assumptions or parameters that are required as contacts shrink to the nanoscale. Another shortcoming of these models is the difficulty of experimentally determining the input parameters that should be used. This is the topic of Chapter 4. Finally, another topic not covered by these models is the effect of surface roughness on contact and adhesion (discussed in the next section).

2-3: Relevant prior work on adhesion as a function of roughness[2]

As discussed in Sect. 2-2, the work of adhesion, W_{adh}, between two surfaces is an important property of an interface that governs adhesion forces and contact stresses, and can strongly influence friction and wear between two bodies (*21*). As mentioned, continuum mechanics models assume a single, constant value of W_{adh}, which represents the energy per unit area to separate two perfectly flat surfaces from equilibrium contact to infinite separation. Knowledge of W_{adh} is important for research and applications in many areas, including thin film coatings (*32*), biological and biomimetic adhesion (*33*), composites (*34*), and micro/nanoelectronic mechanical systems (MEMS/NEMS) (*35*). A common method to characterize the work of adhesion between two surfaces is to use an atomic force microscope (AFM) to measure the force, $F_{adhesive}$, required to separate a

[2] Much of this section appears in print: Adapted with permission from Jacobs, T. D. B.; Ryan, K. E.; Keating, P. L.; Grierson, D. S.; Lefever, J. A.; Turner, K. T.; Harrison, J. A.; Carpick, R. W. The Effect of Atomic-Scale Roughness on the Adhesion of Nanoscale Asperities: A Combined Simulation and Experimental Investigation. *Tribol. Lett.* **2013**, 50, 81–93. Copyright 2013 Springer.

nanoscale tip of radius R_{tip} from a nominally flat sample, using Eq. 2.5 or 2.6. This method assumes small strains, that the materials are homogeneous, isotropic, and linearly elastic, and that the tips are perfectly smooth with a paraboloidal geometry (i.e. a three-dimensional revolution of a parabola).

2-3-1: Relevant models of roughness and adhesion based on contact mechanics or van der Waals adhesion

Previous experimental and theoretical work has demonstrated that pull-off forces are highly sensitive to surface roughness. For example, Fuller and Tabor examined adhesion between rubber spheres with radii from 7 to 53 mm and (nominally planar) roughened stiff surfaces (*36*). They found a 90% drop in the apparent work of adhesion as the average roughness R_a, of the flat surface increased from 0.12 μm to 1.4 μm, as shown in Fig. 2.5(a). Separate studies on micromachined surfaces showed a four-fold reduction in adhesion as the root mean square (RMS) roughness (designated R_q) increased from 3 to 10 nm (*37*) and a ten-fold reduction for surfaces where RMS roughness increased from 10 to 40 nm (*38*). When adhesion studies were performed using micron-scale colloidal beads (*39*, *40*) (radii 2 - 10 μm) or intentionally flattened AFM probes (*41*) (flattened areas 600 - 47,000 nm^2) on surfaces of varying roughness, all showed more than an order of magnitude reduction in pull-off force with increasing roughness (RMS roughness ranging from approximately 1 nm to 10 nm in both studies). However, there have been very few experimental investigations into the effect of roughness on contacts where one body is a nanoscale tip, as is the case in tip-based

microscopy and manufacturing. In one such study, adhesion tests using AFM probes with tip radii of 200 nm showed a roughly four-fold reduction in adhesion force as the RMS roughness of the surface increased from 5 - 15 nm, but there was a significant degree of scatter in the data (*42*).

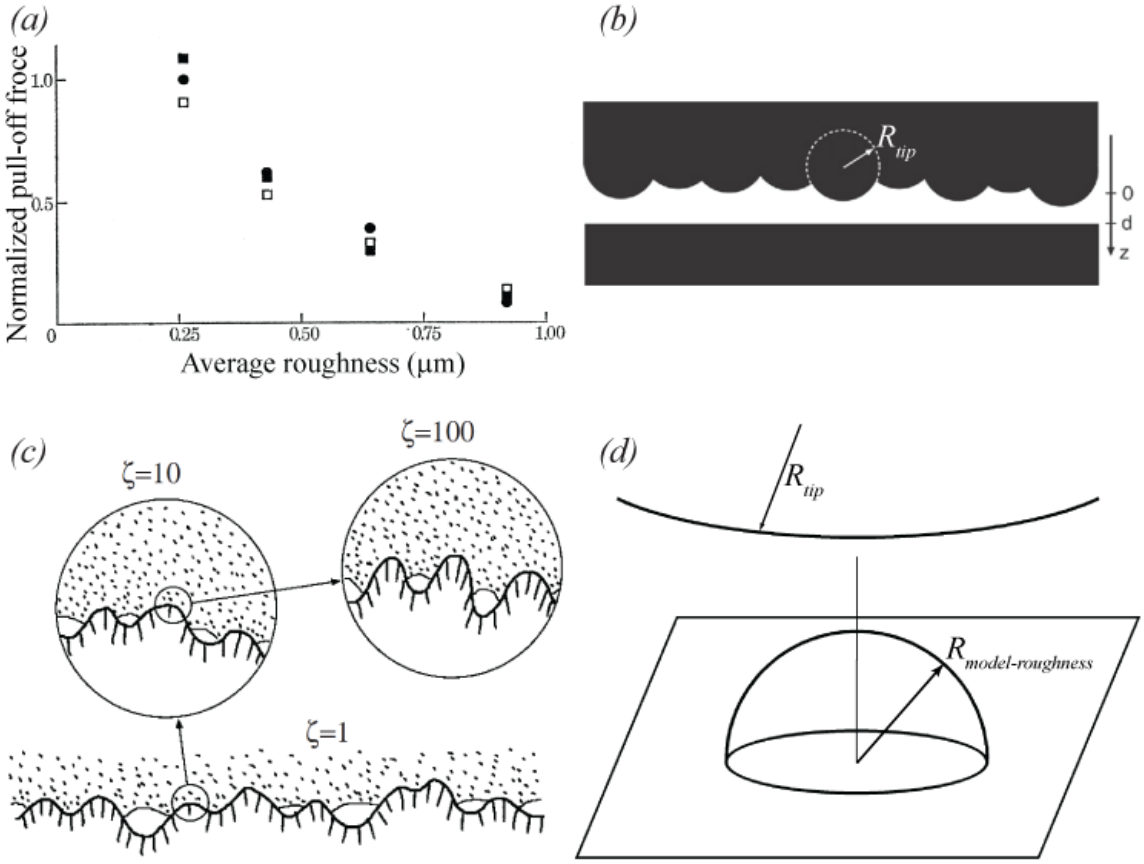

Figure 2.5: Roughness has been experimentally demonstrated to dramatically reduce adhesion; various analytical equations have been proposed for a wide variety of model systems. Fuller and Tabor (*36*) demonstrated a reduction in pull-off force (a) for millimeter-scale smooth rubber spheres in contact with Perspex flats of varying roughness on the sub-micrometer-scale. Different sets of points represent different radii of the spheres, but in all cases, an order of magnitude reduction in pull-off force is observed as roughness increases. Greenwood and Williamson's (*43*) model rough surface (b) is used by Fuller and Tabor along with continuum contact mechanics models to describe the data shown in (a). Subsequent models, also based on contact mechanics, have been proposed for self-affine surfaces with multi-scale roughness (c). Finally, another avenue of roughness modeling uses simplified geometries (d) combined with van der Waals adhesion. The images in (a), (b), (c), and (d) are reproduced with permission from Refs. (*36*), (*44*), (*45*), and (*46*), respectively.

Numerous models have been constructed that examine the effect of roughness on the contact mechanics of nominally planar surfaces. Greenwood and Williamson's seminal work (*43*) described the effect of roughness on the contact area and deformation under load of two non-adhesive half spaces. The roughness was represented by a set of non-interacting asperities with identical radii and a Gaussian distribution of heights, as shown in Fig. 2.5(b). Hertzian mechanics was then applied to determine the forces and deformations of the resulting multi-asperity contact. A key finding was that, even for small levels of roughness, the true contact area is a small fraction of the apparent area. The *adhesion* of rough surfaces with an assumed geometry similar to that used by Greenwood and Williamson was later examined by Fuller and Tabor (*36*) (for the JKR limit of adhesion) and Maugis (*47*) (for the DMT limit). In all cases, the authors demonstrate that results of these models agree qualitatively with experiments. However, describing the rough surface as a number of identical asperities with a Gaussian distribution of asperity heights fails to capture both the multiscale nature of roughness that many real surfaces possess and the significant effect of elastic coupling between asperities. An approach that overcomes these limitations is the work of Persson, in which a rough surface is treated as an elastic body with self-affine fractal topography containing roughness on many length scales (*44*) (Fig. 2.5(c)). This model is thought to be more realistic than those reviewed above, and proposes that there is no direct, universally applicable relationship between root-mean-square roughness and adhesion. Nevertheless, in the experimental testing of this model (*48*), the experimental and model data display an order of magnitude (though not-quite-monotonic) drop in adhesion as root-mean-square roughness increases from 40 - 200 nm . Whether roughness is modeled at one or

multiple scales, all models predict a rapid decrease in adhesion force with increasing roughness because the real contact area is reduced.

Recent experimental work indicates that it is not sufficient to consider only the asperities that are in intimate contact (as is done in the models discussed above), especially for stiff materials. DelRio *et al.* (*37*) used adhesion experiments on micromachined cantilevers as well as numerical simulations to show that up to 65% of the total adhesive force arises due to the van der Waals attraction from portions of the surfaces that are *near* to contact, but not *in* contact. This study represents an extreme case of microfabricated and highly planarized surfaces, but nevertheless demonstrates that the attractive force between near-to-contact regions should not be neglected. Therefore, in another avenue of roughness modeling, the van der Waals attraction is integrated between model interfaces to calculate the total adhesive force between them (*41*, *46*, *49*). In this approach, a smooth sphere (radius R_{tip}) in contact with a rough surface is approximated as the same sphere in contact with a single small asperity (of radius $R_{model\text{-}roughness}$) situated on a perfectly smooth surface (as shown in Fig. 2.5(d)). In the latter configuration, the attractive force between the surfaces can be derived analytically by assuming van der Waals adhesion (*21*, *49*). There are multiple approaches discussed in Refs. (*41*, *46*) for determining how the real roughness of a surface should be distilled into the single parameter $R_{model\text{-}roughness}$. The simplest of these approaches is the *modified Rumpf model* (discussed in detail in Ref. (*46*)), in which $R_{model\text{-}roughness}$ depends only on the RMS roughness R_q of the surface. (The value is determined as the hemispherical radius needed such that a densely packed network of

hemispherical features would have an equivalent value of R_q to the real, rough surface.) The adhesion force is then given by:

$$F_{adhesive} = \frac{A_{1:2} R_{tip}}{6 D_0^2} \left[\left(1 + \frac{R_{tip}}{1.48 R_q} \right)^{-1} + \left(1 + \frac{1.48 R_q}{D_0} \right)^{-2} \right], \tag{2.10}$$

where $A_{1:2}$ is the Hamaker constant between the two materials, and D_0 is the equilibrium spacing of the materials in contact in a van der Waals model (discussed in much more detail in Sect. 4-3-2). Thus, for a given set of materials (constant R_{tip}, $A_{1:2}$, D_0), the effect of surface roughness is captured completely by R_q. Subsequent models (*41*, *46*) refine the definition of $R_{model\text{-}roughness}$ slightly, but use the same general approach. These models also predict a precipitous drop in adhesion force with increasing roughness because roughness increases the average separation between the two bodies.

Taken together, all of the above models represent significant progress on this topic; however, none of them systematically characterizes adhesion on the sub-nanometer scale, and all of them assume that the rough surface has an overall shape (excluding the roughness) that is nominally planar. Therefore, none are well suited for understanding the effect of roughness of a highly curved tip such as an asperity with nanometer-scale dimensions. While it may seem that there is little mathematical difference between a smooth nanoscale tip on a rough surface and a rough nanoscale tip on a smooth surface, in fact, there two important considerations that come up in the latter case. First, it is not trivial to characterize the roughness on a highly curved surface. It is difficult to measure the topography of a sharp tip in detail and, once measured, the topography cannot be easily reduced to a single parameter such as root-mean-square roughness. Second, if

measurements of rough planar surfaces are being made using a nanoscale tip that is assumed to be perfectly smooth, then systematic errors are being introduced into those measurements – and the magnitude of those errors are not easily quantified since the roughness of the tip is unknown.

There has been some initial progress on ultra-small-scale roughness and curved tips. Using MD simulations of a larger curved surface (R_{tip} = 441 nm), Mulakaluri and Persson (*50*) applied the self-affine fractal model to show an order of magnitude drop in adhesion as roughness increased from 0.1 to 1.2 nm. Luan and Robbins (*3*) used atomistic simulations on tips that are closer to AFM dimensions (R_{tip} approximately 30 nm) to examine the effect of surface topography. They demonstrated a factor of 2 - 4 change in adhesion of amorphous surfaces as compared to bent or cut crystalline surfaces. Finally, a recent MD study using flat surfaces showed that the adhesion of a model diamond nanocomposite (on a diamond counter-surface) decreased four-fold when RMS roughness increased from 1.2 to 1.5 Å (*51*). While these studies have clearly shown the significance of sub-nanometer-scale roughness on adhesion, none systematically examined this effect, and none contained experimental data demonstrating the effect of sub-nanometer-scale roughness on the effective work of adhesion between a tip and a substrate. In Chapter 5, *in situ* adhesion tests are reported which allow the concurrent measurement of tip geometry and adhesive force to enable this type of comparison.

2-3-2: Concluding remarks about roughness and its effect on adhesion

Much progress has been made in determining the variation of adhesion with roughness on nominally planar surfaces. However, two primary questions that remain are the effect of sub-nanometer-scale roughness on adhesion, and also the effect of such roughness on highly curved probe tips such as those used in probe-based microscopy and nanomanufacturing. The first question concerns fundamental limits of how small roughness can be and what effect it has when it reaches those limits. Even a multi-scale self-affine model of roughness must have a short wavelength cut-off at which it can no longer hold. The second question is of scientific relevance as important quantities are routinely measured using rough nanoscale AFM probes, and of practical relevance as adhesion represents a significant limitation in the commercialization of nanoscale devices and manufacturing. These questions will be addressed in part in Chapter 5.

2-4: A review of nanoscale wear tests performed using the atomic force microscope and their comparison to macro-scale wear

2-4-1: A brief review of relevant results from wear at macroscopic length scales

While there are many different wear mechanisms that apply for different conditions and material systems, the most broadly applicable to macro-scale systems is the Archard equation. As famously cataloged by Meng and Ludema (*52*), there are at least 16 distinct wear mechanisms used in prior literature (such as adhesive wear, abrasive wear, fretting, scuffing) – most of which are not rigorously or consistently defined – and there are at least 182 different equations that have been proposed to

describe different types of wear. The authors describe how the vast majority of these are empirical, and many seem to apply to one particular system or even just to one particular scientific manuscript. The most widely used of these many equations to characterize the kinetics of a particular wear process is the Archard equation (*53*) or some closely-related variant. The Archard equation assumes that the volume removed V_{lost} is proportional to the product of applied load $F_{applied}$ and sliding distance d_{slide} and is commonly expressed as:

$$V_{lost} = K_{Archard} d_{slide} \frac{F_{total}}{H}, \tag{2.11}$$

where $K_{Archard}$ is the *dimensionless wear coefficient*, and H is the hardness of the softer material. While this form of the Archard wear law was derived using simple arguments based on fully plastic material removal (*54*), the equation is frequently generalized to a wide variety of materials, and is expressed more generally (for instance, in Ref. (*55*)) as:

$$V_{lost} = k_{Archard} d_{slide} F_{total}, \tag{2.12}$$

where $k_{Archard}$ represents the dimensional wear coefficient, and is often quoted in units of [mm^3/(Nm)]. As Rabinowicz (*56*) discusses in the celebratory 100th volume of the journal *Wear*, the Archard equation applies directly to the most common wear mechanisms (adhesive and abrasive wear, in his description), and can be used to characterize wear in other wear mechanisms even if its physical interpretation in those cases is not as clear.

The Archard equation is extremely useful for characterizing wear in practical settings and empirically predicting the service life of engineering components (*55*, *57*). There are numerous examples of Archard-like behavior on the macro-scale (for example,

Ref. (*58*)) and even the micro-scale (for example, Ref. (*59*)). However, these are often composed of multi-asperity contacts and their behavior should be expected to differ from that of a single asperity. Additionally, the atomic-scale details and interactions of the surfaces in contact are likely to dominate the kinetics of wear of a single asperity. Therefore, there is no reason *a priori* to assume that the Archard wear equation should describe wear at the nanoscale. However, just like with continuum contact mechanics in Sect. 2-2, Archard's equation represents a standard for comparison in measurements of nanoscale wear – either to demonstrate agreement or deviation and regimes where different models are required.

Even in cases where Archard's law *does* apply, however, the equation remains fundamentally empirical and the wear coefficient is an experimentally measured parameter that cannot be predicted ahead of time. More generally, a fundamental, predictive understanding of wear remains elusive at all length scales remains elusive. Therefore, just as nanoscale studies are providing a clearer picture of friction at all length scales (see Chapter 1), it is hoped that nanoscale wear studies will provide a clearer picture of the scientifically based mechanisms underlying material removal and of the kinetics that govern those.

2-4-2: Nanoscale wear tests using the atomic force microscope and deviations from the Archard equation

As discussed, the atomic force microscope (AFM) has become a standard tool for studying nanoscale contact phenomena by sliding a single asperity across a well-defined

surface. It therefore has been widely used to induce and detect wear on a surface of interest. Early studies using these techniques (for example, Refs. (*60-62*)), typically used very high loads (in the range of 1 μN to 1 mN) and observed catastrophic wear processes such as deep scratches and plowing – akin to those seen on the macro-scale. They demonstrated a damage threshold, below which the large-scale wear could be prevented; this result is also in accordance with macro-scale behavior (*63*). However, in the last decade, a large number of detailed experimental studies have investigated nanoscale contacts under nanoscale loads (1 nN – 1 μN) using standard contact-mode AFM techniques. These have characterized the wear that occurs below this damage threshold.

A number of experimental studies have characterized wear progression in sharp tips or flat surfaces composed of a variety of materials (including silicon and silicon nitride (*64-66*), diamond and related materials (*67-69*), and minerals such as sodium chloride (*70*), mica (*71*, *72*), and calcite (*73*)) under various loads, velocities, and environments. The first trend that emerged from many of these studies is that Archard's equation is inadequate for describing wear in nanoscale single asperity sliding contacts. Most significantly, the dimensional wear rate $k_{Archard}$ is typically not constant with sliding distance (*65*, *66*, *74*) – neither for wearing surfaces (Fig. 2.6(a)) nor for wearing probes (Fig. 2.6(b)). Not only does $k_{Archard}$ consistently decrease over the course of the test, but also the measured quantity is of limited utility since its value depends on the length of the interval over which it is being measured. Further, a non-linear dependence of wear rate on applied load has been observed for both single asperity wear (i.e. tip wear) (*66*) and for surface wear (*73*). Finally, while there are limited studies of the effect of sliding

speeds, the nanoscale wear rates do not appear to be independent of velocity (*75*, *76*). As a consequence new models have been put forth to explain the progression of wear in these experiments (*73*, *77*, *78*). The most widely supported of these assume that wear is occurring in an atom-by-atom fashion.

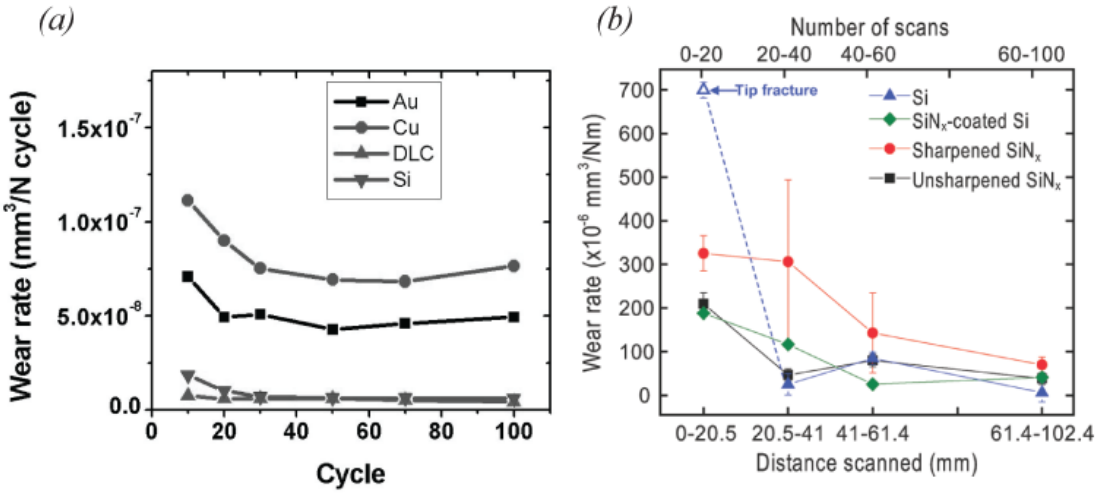

Figure 2.6: Nanoscale wear tests performed in the AFM demonstrate varying wear rates with sliding distance, in contrast to the macroscale Archard equation. *Substrate* wear was measured (a) during sliding of a diamond-coated AFM tip over flat surfaces of various materials (legend) (*64*). The sliding was performed at 500 nN; while not directly specified, one "cycle" appears to correspond to 4 μm of sliding. In separate experiments, *tip* wear was measured (b) during sliding of AFM tips of various materials (legend) on flat substrates of ultrananocrystalline diamond (*79*). The latter experiment was conducted under 0 nN of applied load, i.e. under the action of adhesion. The images in (a) and (b) are reproduced with permission from Refs. (*64*) and (*79*), respectively.

2-4-3: Nanoscale wear laws based conceptually on reaction rate theory

Some of these AFM-based wear tests have allowed observations which suggest that atom-by-atom wear is occurring (*65*, *69*, *76*, *79*, *80*). In other words, that surface modification is occurring by the removal of individual atoms or, at most, extremely small

clusters of atoms rather than by larger-scale modification such as fracture or plastic deformation. There has not been *direct* experimental evidence for this claim, but three observations suggest that is may be accurate: (1) the rate of wear in the low-load regime is very low – in some cases calculated to be as small as one atom per millimeter of sliding (*65*, *68*); (2) there has been crystalline structure observed in the redeposited wear debris (*80*) (indicating small enough debris particles that ordering is possible); and (3) the smoothness of the profiles of worn probes indicates a very small unit of wear events (*69*, *79*). Many equations have been proposed to describe wear in this regime, for example Refs. (*65*, *70*, *71*, *73*, *77*, *81*); they are all based (at least conceptually) on formalisms developed for thermally activated processes (for example, atomic diffusion in a crystal). Each model is briefly described below; in some cases, the models disagree with one another or even inaccurately represent the underlying thermally activated model. This will be discussed more rigorously in Chapter 6, where a review is presented of the kinetics of stress-mediated thermally activated processes and implications for nanoscale wear are discussed.

In an early study by Park *et al.* (*73*), a silicon nitride probe tip was raster-scanned across a surface step of calcite in an aqueous environment. Scanning increased the rate of dissolution of ions at the step edge and, in particular, induced nucleation of a double-kink. Simultaneous topographic images showed that, as these double kinks nucleated on the step edge and grew laterally, the step receded by one lattice spacing l per dissolution (or wear) event. Thus, the velocity of growth of the wear track, v_{track} (the distance the step recedes in nanometers per second), is proportional to the time-rate of wear, $\Gamma_{atom\text{-}loss}$.

When the rate v_{track} is plotted against the applied normal contact force F_N, there is an exponential dependence, as shown in Fig. 2.7(a). These authors were the first to model wear behavior using Arrhenius kinetics and transition state theory.

In their model, Park *et al.* describe a form for the rate of growth of the wear track v_{track} due to kink nucleation that is based on reaction rate theory:

$$v_{track}\left[\frac{m}{s}\right] = v_{track,0}\exp\left(-\frac{\Delta U_{act} - \sigma_{rr}\Delta V_{act}}{k_B T}\right), \tag{2.13}$$

where $v_{track,0}$ represents a constant, ΔU_{act} and ΔV_{act} represent the activation energy and activation volume of kink nucleation, k_B is Boltzmann's constant, T is absolute temperature, and σ_{rr} is the Hertzian radial stress, evaluated at the edge of the contact – the largest tensile stress predicted by the Hertz model. In this picture, v_{track} varies exponentially with changes in the stress and, by fitting the experimental data, an activation volume can be directly extracted. Since temperature was not varied, the activation energy cannot be directly measured. Instead, the authors estimate values for all non-measurable quantities in Eq. 2.13 and then solve the equation for ΔU_{act}.

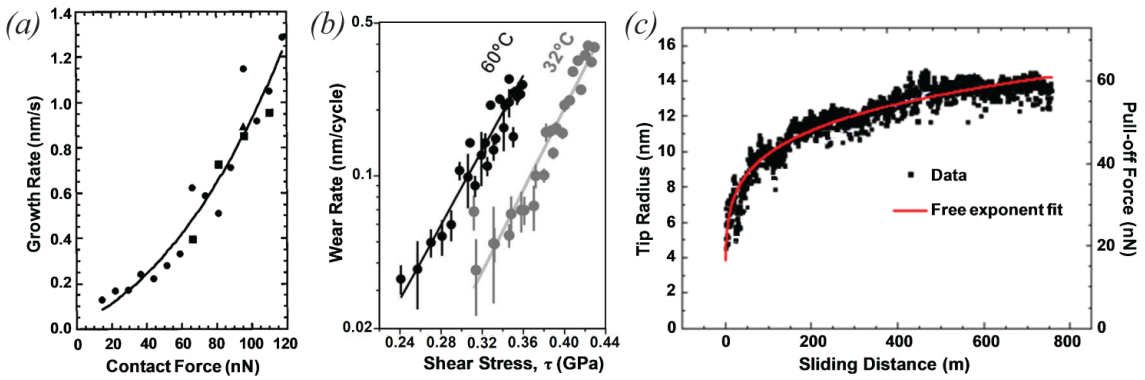

Figure 2.7: Several AFM-based investigations into nanoscale wear of surfaces and tips have been analyzed assuming an exponential dependence of wear rate on load or stress in the contact. Park (*73*) calculated the growth rate of wear pits (a) on a calcite surface during sliding with a silicon nitride tip in an aqueous solution. Sheehan (*70*) measured the wear rate (b) of a sodium chloride substrate during sliding with a silicon nitride tip at two different temperatures in an environment of dry nitrogen. Gotsmann and Lantz (*65*) calculated the change in tip radius with sliding (c). In all cases, points represent experimental data and the solid line represents a fit to that data using a model in which the wear rate varies exponentially with contact stress. The images in (a), (b), and (c) are reproduced with permission from Refs. (*73*), (*70*), and (*65*), respectively.

Similar experiments were performed by Sheehan (*70*) on NaCl in nitrogen environments at different relative humidities and at two different temperatures (32 °C and 60 °C), as shown in Fig. 2.7(b)). In this study, step edge recession was also monitored, and the rate of volume loss $\dot{V}_{wear}$ [nm/cycle] from the surface was calculated. The author's analysis built on that of Park *et al*. (*73*), but instead of using the radial Hertzian stress σ_{rr}, he proposed that the sub-surface Hertzian shear stress τ_{Hertz} would have the most significant effect on atomic-scale wear. This stress was evaluated at a depth of one monoatomic step of the NaCl. Thus, Sheehan fit the measured data using the following equation, based on a slightly different interpretation of reaction rate theory:

$$\dot{V}_{lost}\left[\frac{nm}{cycle}\right] = \dot{V}_{lost,0}\exp\left(-\frac{\Delta U_{act} - \tau_{Hertz}\Delta V_{act}}{k_B T}\right), \tag{2.14}$$

As with the Park study, the measurements of wear rate versus stress are fitted and a value for the activation volume is extracted from the best-fit curve. Additionally, by introducing temperature variation, Sheehan's data is the first to measure changes in wear rate with temperature and thus is the first set of data where the stress-free activation energy barrier could be directly accessed. However, having only two temperature data points over a limited temperature range leads to large uncertainty in this value.

Gotsmann and Lantz (*65*) applied Arrhenius kinetics to the wear of the scanning tip rather than the scanned surface, as had been done previously. In this investigation, the radius change of silicon probe tips was monitored *in situ* during extremely long-distance scanning at a variety of applied loads over a polymer (polyaryletherketone) surface. Sharp, conical tips with initial radii of 3-5 nm were scanned for hundreds of meters. An *in situ* force-displacement test was performed at regular intervals to measure pull-off force $F_{adhesive}$, which was used to calculate the tip radius. During sliding, the tip radius changes as shown in Fig. 2.7(c). By assuming that the tip is wearing away as a truncated cone, the authors model the change in height of the conical tip using a modified version of the reaction rate law:

$$\frac{\partial h}{dt_{slide}}\left[\frac{nm}{s}\right] = l f_{att}\exp\left(-\frac{\Delta U_{act}}{k_B T} + \frac{\tau_{friction}\Delta V_{act}}{k_B T}\right), \tag{2.15}$$

where l is the lattice constant of the material, assumed equal to thickness of one atomic layer of material. The authors modify the above equation by using the geometry of a

cone (with opening angle θ_{cone}) and by assuming a form for the frictional shear stress $\tau_{friction}$ adapted from the work of Briscoe and Evans (*82*), which is empirically derived, but can be motivated using a thermally activated model of friction (*83*):

$$\tau_{friction} = \tau_0 + \xi\sigma_{normal,mean} + \frac{k_B T}{\Delta V_{act,friction}} \ln\left(\frac{v}{v_0}\right), \tag{2.16}$$

where $\sigma_{normal,mean}$ is the average normal stress in the contact, k_B is Boltzmann's constant, T is the absolute temperature, v is the sliding velocity and $\Delta V_{act,friction}$ is the activation volume of the friction process (not the activation volume of the wear process $\Delta V_{act,wear}$, designated in elsewhere in this document as ΔV_{act}). The parameters ξ, τ_0, and v_0 are experimentally measured constants defining: the pressure dependence of shear stress, the value of the shear stress extrapolated to zero pressure, and a characteristic velocity, respectively. The authors then make some simplifying assumptions specifically: (1) that the activation volumes associated with friction and wear are identical; (2) that the cone truncates in a flat plateau of radius a_{flat}, such that $\sigma_{normal,mean} = (F_{adhesive} + F_{adhesive})/(\pi a_{flat}^2)$; and (3) that the adhesive force scales linearly with radius a_{flat} of the flat tip apex (i.e. $F_{adhesive} = c \times a_{flat}$, where c is a constant). Under these assumptions, the result is a differential equation relating the apex radius a_{flat} to the sliding distance d_{slide}:

$$\frac{\partial a_{flat}(d_{slide})}{\partial d_{slide}} = \tan(\theta_{cone}) \exp\left[-\frac{\Delta U_{act}}{k_B T} + \frac{\Delta V_{act}}{k_B T}\left(\tau_0 + \xi \frac{F_{applied} + c a_{flat}}{\pi a_{flat}^2}\right)\right]. \tag{2.17}$$

Equation 2.17 is numerically solved for a_{flat} and fit to the experimental tip wear data using an effective activation energy (ΔU_{act} - $\Delta V_{act}\tau_0$) and an effective activation volume

($\xi\Delta V_{act}$) as fitting parameters. Note that while the rate of wear exhibits the familiar exponential dependence on stress in this model, the shape of the curve in Fig. 2.7(c) reflects the fact that the contact stresses change as wear progresses and the tip gets blunter. Bhaskaran *et al.* (*68*) used the same model to analyze data from a related study of a silicon-containing diamond like carbon (DLC) tip over a silica surface.

Additional thermally activated models of atomic-scale wear have been proposed, though other studies did not directly measure or calculate values for activation parameters. Kopta and Salmeron (*71*) examined wear of muscovite mica samples during AFM scanning in humid air. Specifically, the authors observed that 2 Å-deep wear scars appeared in the mica after a certain number of scans, indicating detachment of the top layer of SiO_4 tetrahedra. Significantly, wear pits only developed after a characteristic number of scans, which depended on the total applied load $F_{applied}$. The authors modeled this behavior as thermally activated cleavage of Si-O bonds, detaching single SiO_4 tetrahedra and leaving behind point defects not observable in the AFM images. The rate of creation of point defects as a function of applied load $\dot{N}_{def}\left(F_{applied}\right)$ was modeled as:

$$\dot{N}_{def}\left(F_{applied}\right) = \rho_{surf} A_{contact} f_{att} \exp\left[\frac{\Delta U_{act} - \delta\left(\Delta U_{act}\right)}{k_B T}\right] \tag{2.18}$$

where ρ_{surf} is the surface density of atoms, and $\delta(\Delta U_{act})$ represents a load-dependent reduction in activation barrier that the authors estimate using scaling arguments. When the density of defects reaches a critical level, a large section of the top layer detaches, creating a detectable wear pit. While the authors are able to accurately fit their data using

a form of Eq. 2.18, they did not directly extract the activation parameters. Further evidence for their description of wear progression in mica (individual bond scission events leading to larger-scale displacement of mica layers) was later validated directly using lattice-resolved friction images of the evolving mica surface (*72*). The latter authors also investigate the effect of solution pH on wear progression and find further support for this argument based on thermally activated bond-breaking.

A theoretical model of thermally activated sample wear has been developed by D'Acunto (*77*, *81*), in which the transitioning atoms undergo a diffusion-like hopping process. This model considers wear of sample atoms in two ways: (1) the atom can be pulled onto the tip due to van der Waals attraction; or (2) it can be dragged along the surface by shear forces. In this model, the two processes are modeled using Arrhenius rate laws with independent activation barriers. This model usefully considers the question of what happens to the atoms after they are worn away, which is not considered in the other models. The barrier for jumping between the tip and sample is taken as the attractive term in the equation for the van der Waals force, and is thus dependent on tip/sample separation. The barrier for jumping laterally is taken as the height of the corrugations of the sample's potential energy surface. According to the assumptions in the paper, the barrier for lateral jumps is significantly lower and therefore this is taken as the primary wear mechanism. While this model is also based on an Arrhenius rate law, results cannot be compared directly with Refs. (*65*, *70*, *73*) since the activation barrier (taken as the energy surface corrugation) is independent of normal or frictional forces.

2-4-4: Concluding remarks about AFM-based nanoscale wear tests

In summary, many nanoscale wear experiments have been performed using the atomic force microscope. While the Archard equation has previously been shown to describe wear in a wide variety of systems and conditions on the macroscale, it does not adequately describe the wear of nanoscale contacts. For several systems under a variety of low-load sliding conditions, wear at the nanoscale appears to occur in an atom-by-atom fashion. Further, experimental data in many of these studies can be well fit with an exponential dependence on load or stress in the contact. However, various authors fit their experimental data using different equations; some of these are mutually contradictory, others lack a solid foundation in chemical kinetics. In Chapter 6, a more rigorous framing is presented of wear via stress-mediated thermally activated reactions, and the interpretation of various activation parameters is more thoroughly discussed.

2-5: Investigations into nanoscale wear using ex situ *and* in situ *imaging; demonstrated nanoscale wear mechanisms*

2-5-1: Imaging a wearing probe using ex situ *electron microscopy*

In addition to the AFM-based wear experiments discussed above, there have been many excellent wear investigations using periodic *ex situ* imaging of the scanning probes to measure changes in geometry of the wearing materials. The most thorough of these were performed by Chung and co-workers (*64*, *67*, *74*) and by Liu and co-workers (*69*, *79*). These allowed the identification of material removal mechanisms and, in some cases, allowed the measurement of volume lost during sliding.

Chung and Kim imaged silicon probes after AFM scanning on silicon and diamond-like carbon (DLC) surfaces (*74*). Very impressive, high resolution images were taken of the tips, as is shown in Fig. 2.8(i-ii); however, oxidation upon exposure to air, contamination during scanning and irreproducible mounting in the TEM (see Sect. 3-1) precluded direct comparison of the nanoscale tip shape before and after sliding. Instead, wear mechanisms are inferred from characteristics of tip appearance after sliding. The authors conclude that fracture of the ultra-sharp silicon probes was common upon initial contact in AFM, but that this can be avoided with slow, careful approach. In cases where fracture was avoided, TEM images of tips after scanning showed flattening in a manner that might be consistent with gradual modification of the amorphous oxide layer and, for sufficiently long scans, the underlying silicon. Another investigation using nanocrystalline diamond-coated silicon AFM probes sliding under 1 - 5 μN of load showed some probes that appeared to have been flattened gradually, and others that showed evidence of a sudden, large fracture event (*74*). More recently, Liu *et al.* used periodic TEM of AFM probes to image silicon, silicon nitride, and ultrananocrystalline diamond probes at regular intervals during sliding (*69*, *79*). In contrast to prior work, the authors were systematic about imaging at regular intervals using similar orientation in the TEM, to allow direct analysis of tip shape evolution, as shown in Fig. 2.8(a-f). In agreement with Chung and Kim, Liu *et al.* saw fracture in the silicon tip and also wear that appeared to be gradual. Volume removal in silicon nitride and UNCD probes was more consistently gradual. Further, the study by Liu *et al.* used quantities measured in the TEM (such as tip radius) to improve the accuracy of assumptions and input parameters for calculating quantities such as work of adhesion in the AFM.

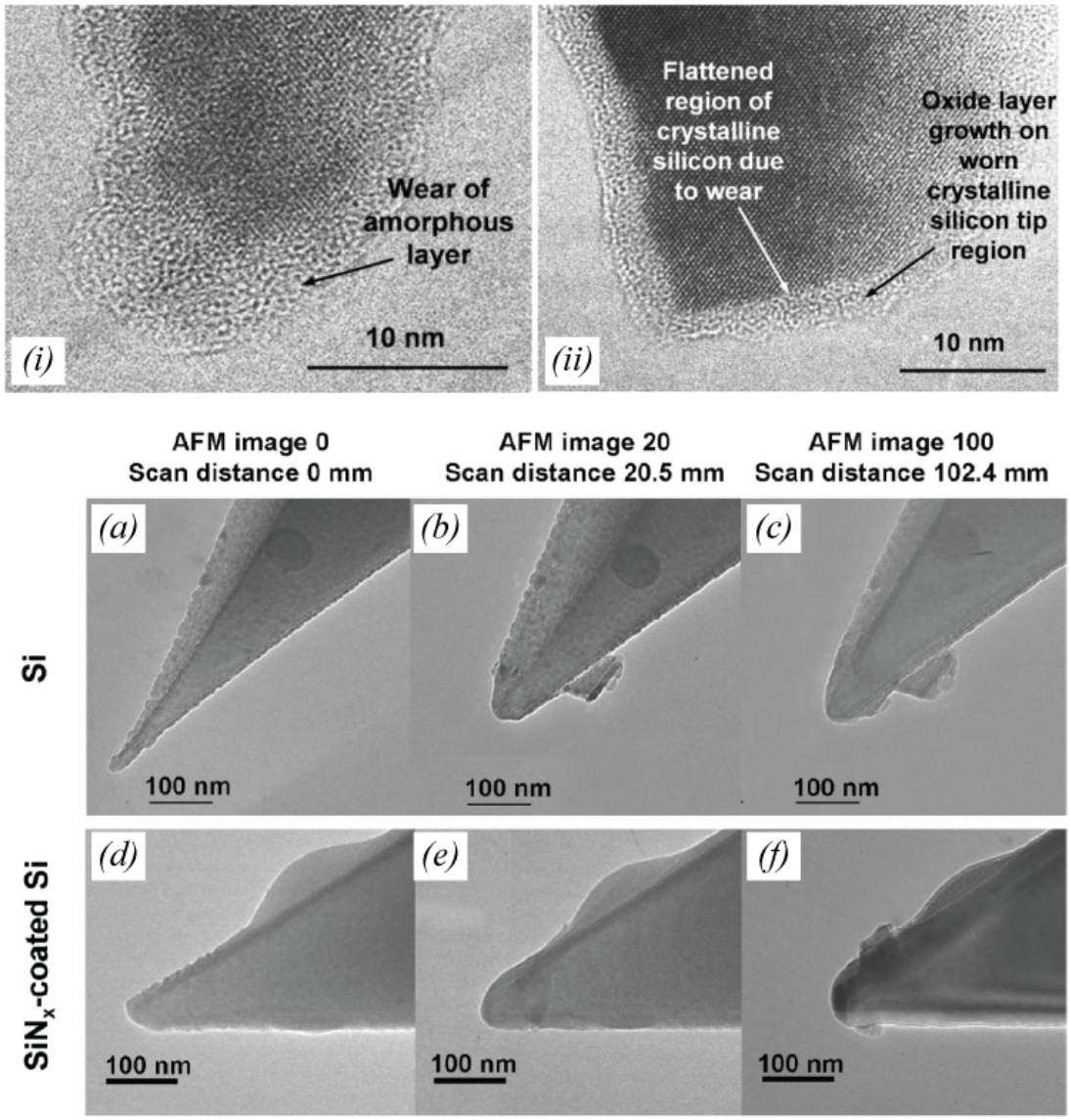

Figure 2.8: Using *ex situ* TEM imaging at intervals during an AFM-based wear test allows visualization of the tip geometry and provides some evidence of wear mechanisms. Chung and Kim (*64*) imaged a silicon tip after sliding on a (100) silicon surface in air under a load of 10 nN. After 32 μm of sliding (i), the authors assert that wear occurred only in the "amorphous layer" (of unspecified composition); by contrast, in after 320 μm of sliding, they believe that wear progressed into the crystalline silicon, then a thin oxide has developed over the worn surface after the wear test, but prior to insertion into the TEM. In a separate investigation, Liu *et al.* (*79*) investigated wear in silicon probes (a-c) and similar probes coated with silicon nitride (d-f). The silicon probe shows evidence of both fracture (as demonstrated by the broken piece adhered to the side in (b)) and gradual wear (as evidenced by rounded tip profiles in (b) and (c)). By contrast, the silicon nitride-coated probe appears to have worn gradually throughout testing. The images in (i-ii) and (a-f) are reproduced with permission from Refs. (*74*) and (*79*), respectively.

In some of the above-mentioned investigations, the amount of removed material was quantified. In Ref. (*64*), the authors made a "quantitative estimate of wear" (pg. 138) of silicon and silicon nitride probes from SEM images of the AFM tip, as shown in Fig. 2.9(a). The resolution of the measurement was limited by the resolution of the imaging, measuring typical minimum volumes of 10^7 nm^3 removed. The measurements appear to deviate significantly from Archard's wear law, as volume lost does not scale linearly with load or with sliding distance. However, the authors still quote values for the wear coefficient, $k_{Archard}$. In Ref. (*67*), the authors report wear rates of $4.3\text{-}5.8\times10^{-6}$ $mm^3/(Nm)$ for the first 300 μm of sliding and $3.9\text{-}5.0\times10^{-7}$ $mm^3/(Nm)$ after 1500 μm of sliding, implying that wear slows down as sliding continues. The authors attribute this to the decreasing contact pressure due to the flattening of the probe. Additionally, in both of their investigations Liu and coworkers (*69*, *79*) carefully measured the volume lost in their studies with the highest volume resolution yet demonstrated using direct visualization. An example of such a measurement is included in Fig. 2.9(b), and can measure minimum volume loss of approximately 10^5 nm^3.

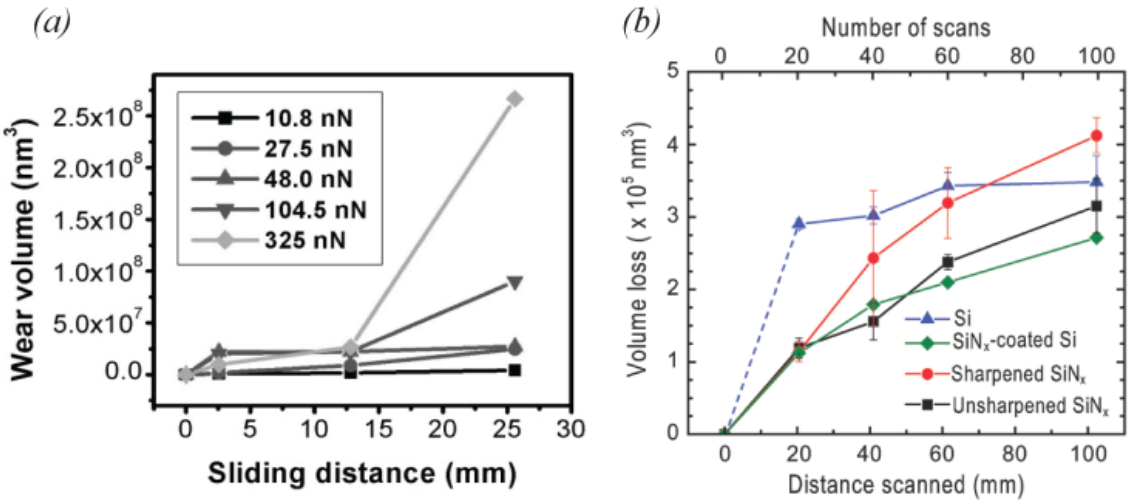

Figure 2.9: Periodic *ex situ* TEM images have been used to calculate the amount of volume lost from the wearing tips; removed quantities as small as 10^5 nm^3 have been observed. Worn volume has been measured (a) for a silicon tip sliding on a (100) silicon substrate at various applied loads (legend). In a separate study, wear was quantified (b) for tips of various materials (legend) sliding without applied load over ultrananocrystalline diamond. The images in (a) and (b) are reproduced with permission from Refs. (*64*) and (*79*), respectively.

Taken together, these *ex situ* investigations have advanced the field by significantly improving the volume resolution of tip wear, and demonstrating certain mechanisms by which nanoscale wear can occur. The limitation of these studies is the interruption of the wear test and the difficulty associated with transferring the AFM probe back and forth to another apparatus. Thus, high-resolution snap-shots of the probes are only available at widely spaced intervals and it is not possible to tell under which conditions wear occurred. For instance, fracture occurred during the first 20 mm of sliding of the tip shown in Fig. 2.8(b), but it is unclear under what conditions it occurred and how much gradual wearing took place before and after. Also, there is surface contamination and oxide visible in Fig. 2.8(i-ii) and other figures from that investigation, but it is impossible to know whether these were present during the sliding, or formed

afterwards. To address these latter questions, fully *in situ* wear investigations are required.

2-5-2: Fully in situ *investigations into nanoscale wear*

There have been several investigations involving contact and lateral sliding conducted using *in situ* testing inside of TEM, dating back to 1996 (*84-86*). Several recent examples of this are shown in Fig. 2.10. For example, many different material pairs have been slid relative to one another, with observation of the resulting deformation and material removal. In work sliding a gold-coated diamond indenter across a silicon surface, fracture and the formation of wear debris in the silicon is clearly visible (*87*) (Fig. 2.10(a-b)). When a tungsten asperity is slid over gold, sliding induces the build-up of sub-surface dislocations and plastic deformation, which is clearly visible in the TEM (*88*) (Fig. 2.10 (c-d)). In contrast, if both sides of the contact are gold, then a pillar-like neck forms (*88*) (as has been shown previously (in Ref. (*85*) and elsewhere), bridging the contact and accommodating all lateral motion in liquid-like fashion (Fig. 2.10(e-g)). Finally, scoop out of wear particles from an aluminum alloy has been observed, along with their subsequent agglomeration (*89*) (Fig. 2.10(h-i). Other fully *in situ* studies have resolved changes in bonding configurations of diamond-like carbon surfaces (*90*) and visualized rolling and deformation of onion-like particles composed layered solid lubricant materials (*91*, *92*).

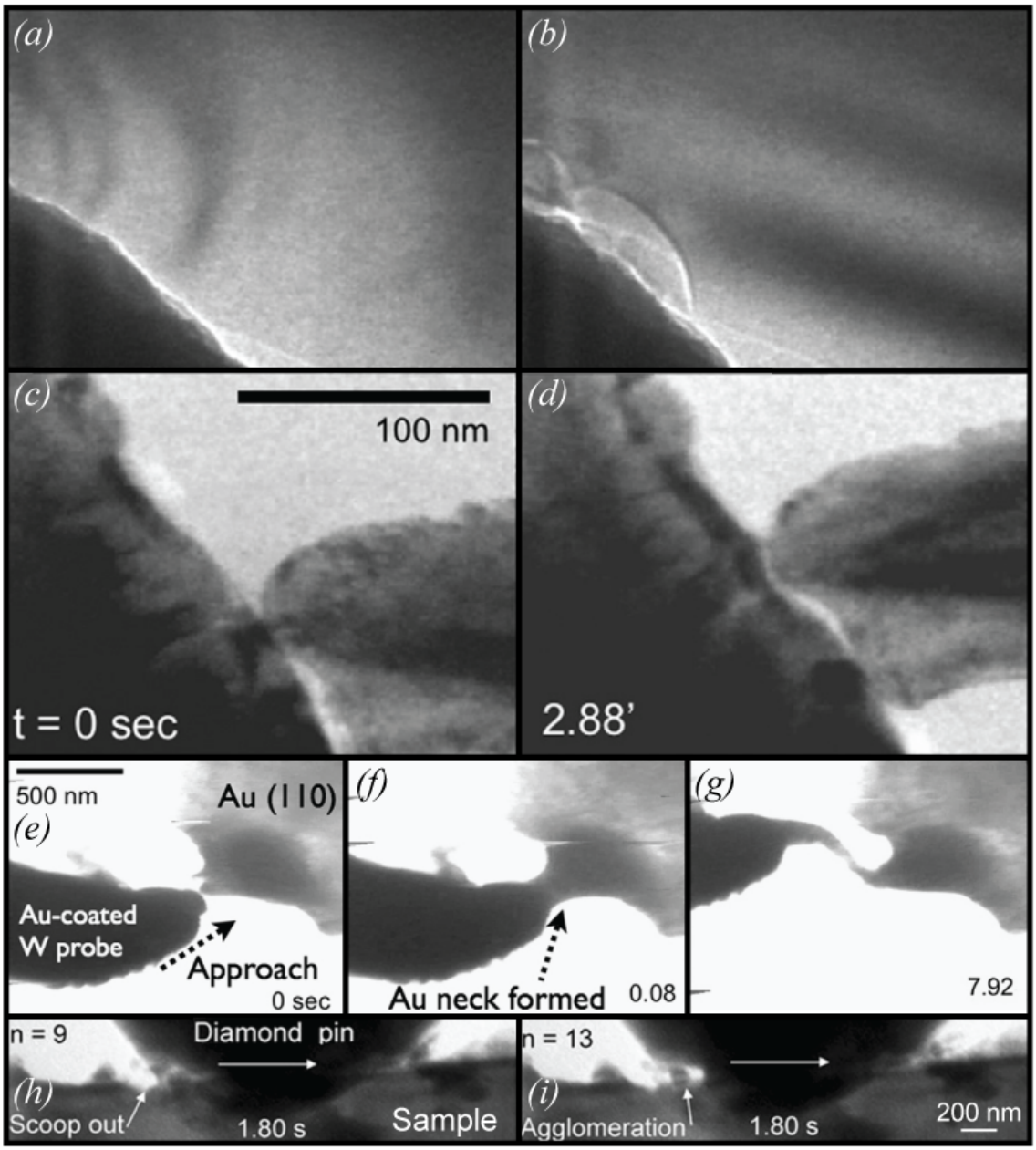

Figure 2.10: Several fully *in situ* wear studies have directly visualized wear processes in real time. In (a-b) (*87*), a gold-coated indenter tip (darker, bottom left) was slid against a thin silicon wedge (lighter, upper right). Initially, semi-circular contrast fringes are visible (a) due to lattice strain; then fracture in the silicon (b) relieves the strain (leaving only linear fringes that arise due to thickness variations). The magnification is only reported as "12 kX"; the images shown in (a) and (b) are estimated (by the present author) to be roughly 1 μm in width. In (c-d) (*88*), a sharp tungsten tip (right side) is slid against a thin gold sample (left). A segment of the surface region in the gold sample initially has a lighter appearance (c), then becomes darker after the tip is slid across it (d). Since this contrast change remains after separation of the contact, it is attributed to

the creation and pile-up of dislocations and sub-surface damage to the lattice. In (e-g) (*88*), a gold-coated tungsten probe (left) is brought into contact with a gold surface feature (top, right). An elongated neck forms and all lateral motion is accommodated plastically in this necked region. Finally, in (h-i) (*89*), a diamond "pin" is slid across a "sample" composed of an aluminum alloy. On various passes (denoted *n*) different behavior is apparent, including "scoop out" of material from the aluminum alloy (h) and later agglomeration of worn material into larger wear particles (i). The images in (a-b), (c-g), and (h-i) are reproduced with permission from Refs. (*87*), (*88*), and (*89*), respectively.

These impressive studies demonstrate some of the deformation mechanisms that are active at the nanoscale, for instance: fracture; sub-surface plastic deformation; neck-formation and deformation; and exfoliation of layered materials. Any and all of these can contribute to the volume loss during sliding that is described as "wear." However, none of these direct, fully *in situ* studies suggests a deformation mechanism that is compatible with the gradual, progressive material removal seen in Sect. 2-2-1. Further, none of the prior *in situ* work has carefully measured nor controlled the conditions of sliding, such as the sliding distance, the normal load, and the geometry at contact. So while these studies depict the way in which material was deformed and removed in specific cases, they cannot shed light on the kinetics of wear, nor the conditions (i.e. stress) under which different mechanisms are active.

2-5-3: Concluding remarks about ex situ *and fully* in situ *nanoscale wear tests*

Impressive nanotribological studies have been performed using complementary *ex situ* and *in situ* microscopy to characterize nanoscale wear. The investigations with *ex situ* imaging involved sliding under well-controlled conditions (using the AFM), enabled improved resolution of tip wear, and suggested possible wear mechanisms, but suffered

from large intervals of sliding between imaging and lacked the ability to correlate TEM observations with sliding events. In contrast, the fully *in situ* wear tests enabled short sliding times and unparalleled real-time visualization of the mechanisms of material deformation and removal, but suffered an almost total lack of quantification of the sliding conditions (distance, load, velocity). The apparatus, methodology, and analysis techniques described in the following chapter have been devised to enable future wear testing that combines the advantages of AFM testing with the advantages of fully *in situ* visualization.

2-6: References

(1) Marder, M. Friction: Terms of detachment. *Nature Materials* **2004**, *3*, 583–584.
(2) Gnecco, E.; Bennewitz, R.; Gyalog, T.; Meyer, E. Friction experiments on the nanometre scale. *J. Phys.: Condens. Matter* **2001**, *13*, R619.
(3) Luan, B.; Robbins, M. Contact of single asperities with varying adhesion: Comparing continuum mechanics to atomistic simulations. *Phys. Rev. E* **2006**, *74*, 026111.
(4) Luan, B.; Robbins, M. O. The breakdown of continuum models for mechanical contacts. *Nature* **2005**, *435*, 929–932.
(5) Mo, Y.; Turner, K. T.; Szlufarska, I. Friction laws at the nanoscale. *Nature* **2009**, *457*, 1116–1119.
(6) Mo, Y.; Szlufarska, I. Roughness picture of friction in dry nanoscale contacts. *Phys. Rev. B* **2010**, *81*.
(7) Carpick, R. W.; Agrait, N.; Ogletree, D. F.; Salmeron, M. Measurement of interfacial shear (friction) with an ultrahigh vacuum atomic force microscope. *Journal of Vacuum Science & Technology B: Microelectronics and Nanometer Structures* **1996**, *14*, 1289–1295.
(8) Johnson, K. Adhesion and friction between a smooth elastic spherical asperity and a plane surface. *P Roy Soc Lond A Mat* **1997**, *453*, 163–179.
(9) Szlufarska, I.; Chandross, M.; Carpick, R. W. Recent advances in single-asperity nanotribology. *J Phys D Appl Phys* **2008**, *41*, 123001.
(10) Hertz, H. On the contact of elastic solids. *J. reine angew. Math* **1881**, *92*, 110.
(11) Johnson, K. L. *Contact Mechanics*; 2011; pp. 1–467.
(12) Greenwood, J. Adhesion of elastic spheres. *P Roy Soc Lond A Mat* **1997**, *453*, 1277–1297.
(13) Greenwood, J. A. Adhesion of small spheres. *Philosophical Magazine* **2009**, *89*, 945–965.
(14) Bradley, R. S. The cohesive force between solid surfaces and the surface energy of solids. *Philosophical Magazine* **1932**, *13*, 853–862.
(15) Derjaguin, BV; Muller, V.; Toporov, Y. P. Effect of contact deformations on the adhesion of particles. *J. Coll. Int. Sci.* **1975**, *53*, 314–326.
(16) Johnson, K. L.; Kendall, K.; Roberts, A. D. Surface energy and the contact of elastic solids. *Proceedings of the Royal Society of London. A. Mathematical and Physical Sciences* **1971**, *324*, 301–313.
(17) Carpick, R. W.; Ogletree, D. F.; Salmeron, M. A general equation for fitting contact area and friction vs load measurements. *J. Coll. Int. Sci.* **1999**, *211*, 395–400.
(18) Tabor, D. Surface forces and surface interactions. *J. Coll. Int. Sci.* **1977**, *58*, 2–13.
(19) Lennard-Jones, J. E. On the determination of molecular fields. II. From the equation of state of a gas. *Proceedings of the Royal Society of London. Series A, Containing Papers of a Mathematical and Physical Character* **1924**, *106*, 463–477.
(20) Maugis, D. Adhesion of spheres: the JKR-DMT transition using a Dugdale model. *J. Coll. Int. Sci.* **1992**, *150*, 243–269.
(21) Israelachvili, J. N. *Intermolecular and Surface Forces*; Academic Press, 2011.
(22) Muller, V. M.; Yushchenko, V. S.; Derjaguin, B. V. On the influence of molecular forces on the deformation of an elastic sphere and its sticking to a rigid plane. *J. Coll. Int. Sci.* **1980**, *77*, 91–101.
(23) Feng, J. Q. Adhesive Contact of Elastically Deformable Spheres: A Computational Study of Pull-Off Force and Contact Radius. *J. Coll. Int. Sci.* **2001**, *238*, 318–323.
(24) Feng, J. Q. Contact behavior of spherical elastic particles: a computational study of particle adhesion and deformations. *Colloids and Surfaces A: Physicochemical and Engineering Aspects* **2000**, *172*, 175–198.
(25) Zheng, Z.; Yu, J. Using the Dugdale approximation to match a specific interaction in the

adhesive contact of elastic objects. *J. Coll. Int. Sci.* **2007**, *310*, 27–34.
(26) Grierson, D. S.; Liu, J.; Carpick, R. W.; Turner, K. T. Adhesion of nanoscale asperities with power-law profiles. *J. Mech. Phys. Sol.* **2013**, *61*, 597–610.
(27) Argento, C.; Jagota, A.; Carter, W. C. Surface formulation for molecular interactions of macroscopic bodies. *J. Mech. Phys. Sol. 45*, 1161–1183.
(28) DelRio, F. W.; Dunn, M. L.; Boyce, B. L.; Corwin, A. D.; de Boer, M. P. The effect of nanoparticles on rough surface adhesion. *J. Appl. Phys.* **2006**, *99*, 104304.
(29) Barthel, E. On the description of the adhesive contact of spheres with arbitrary interaction potentials. *J. Coll. Int. Sci.* **1998**, *200*, 7–18.
(30) Yu, N.; Polycarpou, A. A. Adhesive contact based on the Lennard–Jones potential: a correction to the value of the equilibrium distance as used in the potential. *J. Coll. Int. Sci.* **2004**, *278*, 428–435.
(31) Grierson, D.; Flater, E.; Carpick, R. Accounting for the JKR-DMT transition in adhesion and friction measurements with atomic force microscopy. *J. Adhes. Sci. Technol.* **2005**, *19*, 291–311.
(32) Volinsky, A. A.; Moody, N. R.; Gerberich, W. W. Interfacial toughness measurements for thin films on substrates. *Acta Mater* **2002**, *50*, 441–466.
(33) Gao, H.; Wang, X.; Yao, H.; Gorb, S.; Arzt, E. Mechanics of hierarchical adhesion structures of geckos. *Mechanics of Materials* **2005**, *37*, 275–285.
(34) Finnis, M. W. The theory of metal-ceramic interfaces. *J. Phys.: Condens. Matter* **1999**, *8*, 5811.
(35) Maboudian, R. Critical Review: Adhesion in surface micromechanical structures. *Journal of Vacuum Science & Technology B: Microelectronics and Nanometer Structures* **1997**, *15*, 1.
(36) Fuller, K.; Tabor, D. Effect of Surface-Roughness on Adhesion of Elastic Solids. *P Roy Soc Lond A Mat* **1975**, *345*, 327–342.
(37) DelRio, F. W.; de Boer, M. P.; Knapp, J. A.; David Reedy, E.; Clews, P. J.; Dunn, M. L. The role of van der Waals forces in adhesion of micromachined surfaces. *Nature Materials* **2005**, *4*, 629–634.
(38) Tayebi, N.; Polycarpou, A. A. Reducing the effects of adhesion and friction in microelectromechanical systems (MEMSs) through surface roughening: Comparison between theory and experiments. *J. Appl. Phys.* **2005**, *98*, 073528.
(39) Ramakrishna, S. N.; Clasohm, L. Y.; Rao, A.; Spencer, N. D. Controlling Adhesion Force by Means of Nanoscale Surface Roughness. *Langmuir* **2011**, *27*, 9972–9978.
(40) Segeren, L.; Siebum, B.; Karssenberg, F. G.; Van den Berg, J.; Vancso, G. J. Microparticle adhesion studies by atomic force microscopy. *J. Adhes. Sci. Technol.* **2002**, *16*, 793–828.
(41) Katainen, J.; Paajanen, M.; Ahtola, E.; Pore, V.; Lahtinen, J. Adhesion as an interplay between particle size and surface roughness. *J. Coll. Int. Sci.* **2006**, *304*, 524–529.
(42) Liu, D. L.; Martin, J.; Burnham, N. A. Which fractal parameter contributes most to adhesion? *J. Adhes. Sci. Technol.* **2010**, *24*, 2383–2396.
(43) Greenwood, J.; Williamson, J. Contact of Nominally Flat Surfaces. *Proc. Roy. Soc. A* **1966**, *295*, 300–319.
(44) Persson, B. N. J. Contact mechanics for randomly rough surfaces. *Surf Sci Rep* **2006**, *61*, 201–227.
(45) Persson, B. N. J.; Albohr, O.; Tartaglino, U.; Volokitin, A. I.; Tosatti, E. On the nature of surface roughness with application to contact mechanics, sealing, rubber friction and adhesion. *J. Phys.: Condens. Matter* **2004**, *17*, R1–R62.
(46) Rabinovich, Y. Adhesion between nanoscale rough surfaces I. Role of asperity geometry. *J. Coll. Int. Sci.* **2000**, *232*, 10–16.
(47) Maugis, D. On the contact and adhesion of rough surfaces. *J. Adhes. Sci. Technol.* **1996**, *10*, 161–175.
(48) Persson, B. Elastoplastic Contact between Randomly Rough Surfaces. *Phys. Rev. Lett.* **2001**, *87*.

(49) Rumpf, H. *Particle Technology*; Chapman and Hall: London, UK.
(50) Mulakaluri, N.; Persson, B. Adhesion between elastic solids with randomly rough surfaces: Comparison of analytical theory with molecular-dynamics simulations. *EPL (Europhysics Letters)* **2011**, *96*, 66003.
(51) Piotrowski, P. L.; Cannara, R. J.; Gao, G.; Urban, J. J.; Carpick, R. W.; Harrison, J. A. Atomistic Factors Governing Adhesion between Diamond, Amorphous Carbon and Model Diamond Nanocomposite Surfaces. *J. Adhes. Sci. Technol.* **2010**, *24*, 2471–2498.
(52) Meng, H. C.; Ludema, K. C. Wear models and predictive equations - their form and content. *Wear 181*, 443–457.
(53) Archard, J. F. Contact and rubbing of flat surfaces. *J. Appl. Phys.* **1953**, *24*, 981–988.
(54) Archard, J. The wear of metals under unlubricated conditions. *Proc. Roy. Soc. A* **1956**, *236*, 397–410.
(55) Mate, C. M. *Tribology on the Small Scale: A Bottom Up Approach to Friction, Lubrication, and Wear*; Oxford University Press: Oxford, UK, 2008.
(56) Rabinowicz, E. The least wear. *Wear* **1984**, *100*, 533–541.
(57) Stachowiak, G.; Batchelor, A. W. *Engineering tribology*; Butterworth-Heinemann, 2011.
(58) Jia, K.; Fischer, T. Sliding wear of conventional and nanostructured cemented carbides. *Wear* **1997**, *203*, 310–318.
(59) Beerschwinger, U.; Albrecht, T.; Mathieson, D.; Reuben, R. L.; Yang, S. J.; Taghizadeh, M. Wear at microscopic scales and light loads for MEMS applications. *Wear* **1995**, *181*, 426–435.
(60) Sundararajan, S.; Bhushan, B. Micro/nanotribology of ultra-thin hard amorphous carbon coatings using atomic force/friction force microscopy. *Wear* **1999**, *225*, 678–689.
(61) Jiang, J.; Stott, F. H.; Stack, M. M. A mathematical model for sliding wear of metals at elevated temperatures. *Wear* **1995**, *181*, 20–31.
(62) Machcha, A. R.; Azarian, M. H.; Talke, F. E. An investigation of nano-wear during contact recording. *Wear* **1996**, *197*, 211–220.
(63) Lim, S.; Ashby, M. Overview no. 55 wear-mechanism maps. *Acta Metall.* **1987**, *35*, 1–24.
(64) Chung, K.; Kim, D. Fundamental investigation of micro wear rate using an atomic force microscope. *Tribol. Lett.* **2003**, *15*, 135–144.
(65) Gotsmann, B.; Lantz, M. Atomistic wear in a single asperity sliding contact. *Phys. Rev. Lett.* **2008**, *101*, 125501.
(66) Maw, W.; Stevens, F.; Langford, S.; Dickinson, J. Single asperity tribochemical wear of silicon nitride studied by atomic force microscopy. *J. Appl. Phys.* **2002**, *92*, 5103.
(67) Chung, K.-H.; Kim, D.-E. Wear characteristics of diamond-coated atomic force microscope probe. *Ultramicroscopy* **2007**, *108*, 1–10.
(68) Bhaskaran, H.; Gotsmann, B.; Sebastian, A.; Drechsler, U.; Lantz, M. A.; Despont, M.; Jaroenapibal, P.; Carpick, R. W.; Chen, Y.; Sridharan, K. Ultralow nanoscale wear through atom-by-atom attrition in silicon-containing diamond-like carbon. *Nature Nanotech.* **2010**, *5*, 181–185.
(69) Liu, J.; Grierson, D.; Moldovan, N.; Notbohm, J.; Li, S.; Jaroenapibal, P.; O'Connor, S.; Sumant, A.; Neelakantan, N.; Carlisle, J. Preventing nanoscale wear of atomic force microscopy tips through the use of monolithic ultrananocrystalline diamond probes. *Small* **2010**, *6*, 1140–1149.
(70) Sheehan, P. The wear kinetics of NaCl under dry nitrogen and at low humidities. *Chemical Physics Letters* **2005**, *410*, 151–155.
(71) Kopta, S.; Salmeron, M. The atomic scale origin of wear on mica and its contribution to friction. *J. Chem. Phys.* **2000**, *113*, 8249.
(72) Helt, J.; Batteas, J. Wear of mica under aqueous environments: direct observation of defect nucleation by AFM. *Langmuir* **2005**, *21*, 633–639.
(73) Park, N. S.; Kim, M. W.; Langford, S.; Dickinson, J. Atomic layer wear of single-crystal

calcite in aqueous solution using scanning force microscopy. *J. Appl. Phys.* **1996**, *80*, 2680–2686.
(74) Chung, K.; Lee, Y.; Kim, D. Characteristics of fracture during the approach process and wear mechanism of a silicon AFM tip. *Ultramicroscopy* **2005**, *102*, 161–171.
(75) Bhushan, B.; Kwak, K. J. Velocity dependence of nanoscale wear in atomic force microscopy. *Appl. Phys. Lett.* **2007**, *91*, 163113.
(76) Bhaskaran, H.; Sebastian, A.; Despont, M. Nanoscale PtSi Tips for Conducting Probe Technologies. *Ieee T Nanotechnol 8*, 128–131.
(77) D'Acunto, M. Theoretical approach for the quantification of wear mechanisms on the nanoscale. *Nanotechnology* **2004**, *15*, 795–801.
(78) Agrawal, R.; Moldovan, N.; Espinosa, H. D. An energy-based model to predict wear in nanocrystalline diamond atomic force microscopy tips. *J. Appl. Phys.* **2009**, *106*, 064311.
(79) Liu, J.; Notbohm, J. K.; Carpick, R. W.; Turner, K. T. Method for characterizing nanoscale wear of atomic force microscope tips. *ACS Nano* **2010**, *4*, 3763–3772.
(80) Gnecco, E.; Bennewitz, R.; Meyer, E. Abrasive wear on the atomic scale. *Phys. Rev. Lett.* **2002**, *88*, 215501.
(81) D'Acunto, M. Wear and diffusive processes. *Tribol. Int.* **2003**, *36*, 553–558.
(82) Briscoe, B.; Evans, D. The shear properties of Langmuir-Blodgett layers. *Proc. Roy. Soc. A* **1982**, *380*, 389–407.
(83) Sang, Y.; Dubé, M.; Grant, M. Thermal effects on atomic friction. *Phys. Rev. Lett.* **2001**, *87*, 174301.
(84) Naitoh, Y.; Takayanagi, K.; Tomitori, M. Visualization of tip-surface geometry at atomic distance by TEM-STM holder. *Surface Science* **1996**, *357*, 208–212.
(85) Kizuka, T. Atomic process of point contact in gold studied by time-resolved high-resolution transmission electron microscopy. *Phys. Rev. Lett.* **1998**, *81*, 4448–4451.
(86) Kizuka, T.; Yamada, K.; Deguchi, S.; Naruse, M.; Tanaka, N. Cross-sectional time-resolved high-resolution transmission electron microscopy of atomic-scale contact and noncontact-type scannings on gold surfaces. *Phys. Rev. B* **1997**, *55*, 7398–7401.
(87) Ribeiro, R.; Shan, Z.; Minor, A. M.; Liang, H. In situ observation of nano-abrasive wear. *Wear* **2007**, *263*, 1556–1559.
(88) Merkle, A. P.; Marks, L. D. Liquid-like tribology of gold studied by in situ TEM. *Wear* **2008**, *265*, 1864–1869.
(89) Anantheshwara, K.; Lockwood, A. J.; Mishra, R. K.; Inkson, B. J.; Bobji, M. S. Dynamical evolution of wear particles in nanocontacts. *Tribol. Lett.* **2011**, *45*, 229–235.
(90) Merkle, A.; Erdemir, A.; Eryilmaz, O.; Johnson, J.; Marks, L. In situ TEM studies of tribo-induced bonding modifications in near-frictionless carbon films. *Carbon* **2010**, *48*, 587–591.
(91) Lahouij, I.; Dassenoy, F.; Knoop, L.; Martin, J.-M.; Vacher, B. In Situ TEM Observation of the Behavior of an Individual Fullerene-Like MoS2 Nanoparticle in a Dynamic Contact. *Tribol. Lett.* **2011**, *42*, 133–140.
(92) Lahouij, I.; Dassenoy, F.; Vacher, B.; Martin, J.-M. Real Time TEM Imaging of Compression and Shear of Single Fullerene-Like MoS2 Nanoparticle. *Tribol. Lett.* **2011**, *45*, 131–141.

CHAPTER 3: Methodology – Using TEM to investigate nanoscale contact phenomena

The present chapter describes novel apparatuses and methodologies developed for investigating contact phenomena using a TEM. First, a novel fixture is described for *ex situ* imaging of AFM probes, including the improvements of the novel fixture beyond other fixtures for similar application that were used in prior investigations. Second, the apparatus and methodology are described for performing *in situ* adhesion and wear testing inside the TEM. Finally, the methodology and computational routines for data processing are described. These include methods for: assessing and comparing tip geometry; quantifying tip roughness; measuring dynamic events in videos; calculating relevant adhesion parameters; and quantifying volume change.

3-1: Examining AFM tips in the TEM (for ex situ *testing)*

For initial evaluation of AFM tip quality, and for *ex situ* imaging of AFM tips before and after testing in an AFM, it is useful to have a fixture for mounting AFM probes inside a TEM. A novel fixture was developed[3] for static imaging of AFM probes in a TEM that improved upon the previous state of the art.

[3] This fixture was developed in collaboration with Graham Wabiszewski (PhD Candidate, Department of Mechanical Engineering and Applied Mechanics, University of Pennsylvania) and Alex Goodman (then a senior at The Haverford School, Haverford, PA).

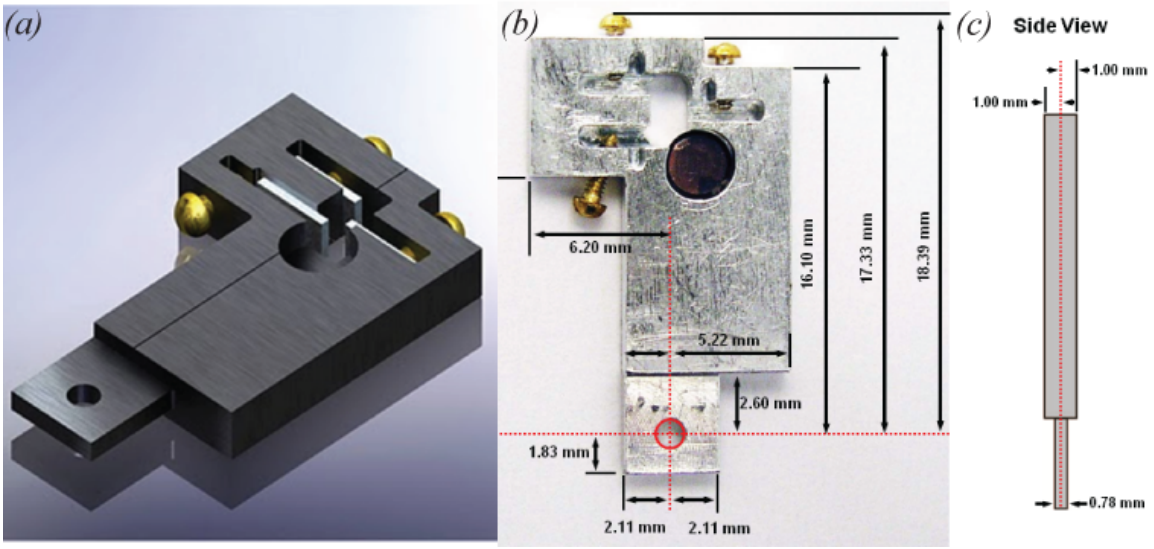

Figure 3.1: A novel fixture was developed to increase the throughput and reproducibility of AFM tip imaging. The novel fixture is shown in perspective (schematically in (a)) and in top view (optical photograph in (b)). The side-view dimensions are indicated in (c). Figure courtesy of Graham Wabiszewski (PhD Candidate, Department of Mechanical Engineering and Applied Mechanics, University of Pennsylvania).

3-1-1: Limitations of previous fixture designs for imaging of AFM probes using TEM

As discussed in Chapter 2, several authors (such as in Refs. (*1*-*6*)) have used TEM to image AFM probes. These authors do not describe the fixturing used; however, it is clear from the images in published articles and from personal communication (with authors from Ref. (*5*, *6*)) that reproducibility of probe alignment hampered the direct and meaningful comparison of TEM images taken before and after use of the probe. Typical approaches used double-sided carbon tape to mount the AFM chip onto a flexible metal strip, which was then inserted into a holding slot in an aluminum plate. The metal strip was secured to the plate with more carbon tape.

This earlier fixturing suffered three primary disadvantages. First, the mounting of the probes was largely irreproducible from one mounting to the next, hampering the ability to compare probes before and after testing in another apparatus. Specifically, the position of the sharp tip was able to deviate typically by several millimeters in all three spatial axes; and the orientation of the conical tip was able to rotate by several degrees about all three axes of rotation. Significant user skill was required to mount the probes in a *similar* position and orientation before and after testing; it was impossible to achieve identical (or even near-identical) position and orientation. Second, the use of carbon tape caused drift of the probes in the TEM and, in some cases, introduced additional contamination into the TEM chamber. Carbon tape is a double-sided conductive adhesive tape, which is a widely-used and highly flexible mounting tool for electron microscopy applications. However, the adhesive tape exhibits a time-dependent viscoelastic response causing positional drift with time, and also exhibits significant thermal expansion/contraction with small temperature changes. Thus, if the tape is stretched during mounting, or if the temperature inside the TEM chamber is different than that of the room, the tape will exhibit shape fluctuations and the mounted probe will translate with time, as is directly observable in the TEM. Additionally, uncovered portions of the adhesive tape can collect carbonaceous contamination and other ambient room debris prior to insertion into the TEM chamber. Contamination can then be introduced into TEM chamber when the electron beam irradiates the carbon tape (as it commonly does during initial low-magnification imaging of the probes) and decomposes the adhesive material into hydrocarbon contamination inside the chamber. Finally, the third primary disadvantage of previous mounting schemes is low throughput and

significant wasted user and instrument time. Only one probe can be inserted into the TEM at a time, so probes must be imaged sequentially with removal/re-insertion of the specimen transfer arm between each. Also, since no calibration grid or standard sample may be simultaneously mounted, then any beam alignment issues also require sample exchange.

3-1-2: Description of the novel fixture design for imaging of AFM probes using TEM

The newly designed fixture (shown in Fig. 3.1(a-c)) addresses each of the aforementioned problems. As is most apparent from Fig. 3.1(b), the new fixture allows for three probes to be mounted concurrently, along with a standard 3-mm calibration grid. This represents a roughly three-fold reduction in time spent on mounting and specimen exchange. Further, the probes are mounted, using setscrews, inside of a slot of well-defined width, length, and depth. The setscrew firmly positions the probe chip flush against the sidewall of the slot, which fixes the position probe tip with respect translation along the *y*-axis (vertical direction in Fig. 3(b)) and fixes the orientation of the probe tip with respect to rotation about the *x*-axis (horizontal direction in Fig. 3(b)) and the *z*-axis (normal to the image plane). The back wall and bottom surface of the slot serve to grossly position the probe with respect to the remaining degrees of freedom (translation along the *x*- and *z*-axis, rotation about the *y*-axis), such that the probe will always be accessible within the travel of the TEM goniometer.

There are several additional advantages of the new fixture. The slot geometries were designed to accommodate a wide range of commercial and custom AFM probes,

which can vary greatly in geometries and cantilever lengths/arrangements. The new fixture eliminates the use of carbon tape, and includes a mounting for a 3-mm calibration grid for rapid beam re-alignment. Finally, a separate mounting block was designed and created that securely holds the fixture in place while the user is mounting or removing probes.

3-1-3: An improvement in mounting reproducibility enabled by the novel fixture

The new fixture enables a significant improvement in reproducibility of probe mounting and therefore the fidelity of comparisons before and after remounting. As shown in Fig. 3.1(b), the probe is mounted such that the long axis of the conical probe tip lies parallel to *y*-axis, which is the axis about which the single-tilt specimen transfer arm can rotate. This enables rotation about the axis of the probe tip using the TEM's goniometer controls. Thus, for AFM probes made from single-crystal materials, TEM diffraction pattern imaging can be used to identify a specific high-symmetry orientation and all imaging can be performed at this specific orientation. Then, after the probe is removed, tested, and re-mounted, goniometer tilt can be used to return to the exact same orientation – as confirmed by the diffraction image. For non-crystalline or polycrystalline samples, a similar procedure can be used, but with apparent tip shape (observed by TEM imaging) as the metric for alignment. The latter method is far less reliably than the former method, but can be useful in cases where imperfections or small pieces of contamination on the shank of the tip break the rotational symmetry of the cone.

3-1-4: Examples of use of the novel fixture, and suggested applications beyond the present investigation.

Using this apparatus, a wide variety of commercial AFM probes as well as probes under development by collaborators have been imaged. The new fixture was used in initial probe selection (for the testing described in Chapters 4, 5 and 7) to evaluate the shape, sharpness, and presence of contamination on probes as received from the manufacturer. This fixture was also used in the *ex situ* UHV testing described in Chapter 4. Beyond the present applications, this fixture could potentially be useful in a wide array of AFM applications where knowledge of the tip shape is required. Many scanning probe microscopy techniques such as friction force microscopy, force spectroscopy, conductive AFM, and AFM nanoindentation, require knowledge of tip shape and size. Additionally, probe-based devices and manufacturing techniques require characterization of tip evolution and robustness. All of these could benefit from a simple, reproducible and reliable way to periodically and non-destructively image scanning probes.

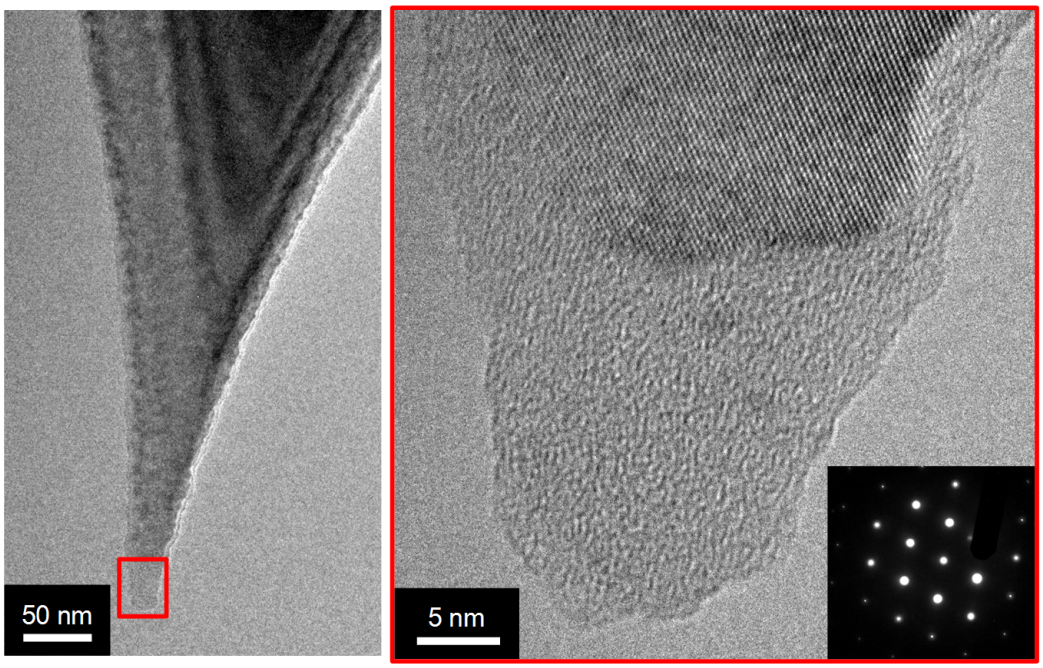

Figure 3.2: The novel fixture allows imaging of AFM probes with reproducible orientations. A typical AFM probes is shown at medium magnification (a) and high magnification (b). The advance of the current fixture is the ability to reproducibly mount the probe in the same imaging orientation following removal for characterization or testing in another apparatus. The diffraction pattern (inset in (b)) was used to accurately realign the tilt using the TEM's goniometer.

3-2: Apparatus and calibration for in situ *adhesion and wear tests inside the TEM*

3-2-1: Instrumentation

As discussed, while periodic *ex situ* imaging of AFM probes using the apparatus described in Sect. 3-1 is useful, significant insight about adhesion and wear can be gained from direct observation of a nanoscale asperity in real-time as it makes and breaks contact and/or slides across a surface. In order to accomplish this in the present work, adhesion and wear tests were conducted inside of a TEM, using an *in-situ* nanoindentation tool. Unless otherwise noted, the TEM was a JEOL 2010F with a field-

emission source and a Gatan Image Filter (GIF) for analytical techniques. It operates at an accelerating voltage of 200 keV, under a typical vacuum of 10^{-6} – 10^{-5} Pa (10^{-8} – 10^{-7} Torr). A point-to-point resolution of 0.23 nm has been measured on this instrument. Occasionally, a JEOL 2010 was also used; this microscope is similar in all respects to the 2010F previously described except that it contains a LaB_6 thermionic filament rather than a field emission source which results in lower spatial resolution (not characterized), and lacks the analytical capabilities.

The *in situ* indenter used in the present investigation was a Hysitron PI 95 TEM Picoindenter, which uses spring-loaded, three-plate capacitor drives for fine-scale, closed-loop actuation along the indentation axis (*7*, *8*) and a piezo-actuator for three-dimensional coarser positioning of the tip. Vibration of the indenter tip is controlled (though not eliminated) through a closed-loop feedback system, which actively cancels the resonance frequency of the transducer (119.8 Hz). Note that this is a particularly unfortunate frequency as it is a harmonic of the line frequency (60 Hz) that is used in the USA. This means that electrical noise at this frequency is common and, since the indenter controller used active damping to reduce vibration, this electrical noise is converted into mechanical noise. Since vibration adds uncertainty to the exact indenter position, it is characterized before every set of experiments using at least three separate ten-second noise tests, in which the input displacement is set to zero and the transducer measures the displacement caused by noise (e.g. ambient mechanical vibration, electrical noise in the feedback loop, etc.).

It should be noted that the original tool that was received from Hysitron had problems with vacuum leaks and extraordinarily slow pump down and was quickly

returned to Hysitron. The replacement tool solved these problems and was used for all testing in the present thesis. A newer model of the *in situ* indenter (Hysitron PI 95 Picoindenter with nanoECR upgrade) was subsequently purchased, which enabled electrical contact resistance measurements and the addition of electrical feed-throughs into the test region. However, this latter tool had unacceptably high levels of vibration, which were extensively investigated and potentially linked to coupling of electrical noise from the TEM goniometer into the transducer position measurement. Because of this vibration, the nanoECR tool was never used for scientific testing, and was eventually sent back to Hysitron for troubleshooting and replacement.

3-2-2: Modification for increasing the resolution of contact force measurement

While the nanometer-scale displacement control of the Hysitron tool is appropriate for investigating nanoscale contact phenomena, its minimum force resolution (hundreds of nanonewtons) is not. Typical adhesive and applied loads in the AFM range from 1-100 nN, which are well below the noise floor of the indenter. Therefore, in present work the force is *not* measured using the indenter, but rather by bringing the indenter tip into contact with a commercial AFM probe, itself a sensitive force measurement device. To achieve this, the AFM chip is mounted rigidly on the sample mount of the indenter, as shown in Fig. 3.3. Thus, the nanoscale tip, which is at the end of a long flexible cantilever, is accessible to the Hysitron indenter tip. The indenter tip (which is considerably flatter than the AFM tip) mimics the flat substrate that is inserted into a traditional atomic force microscope. Further, as with a traditional AFM, the force

in the contact is monitored by detecting the deflection of the cantilever – which has been calibrated prior to testing, see Sect. 3-2-4.

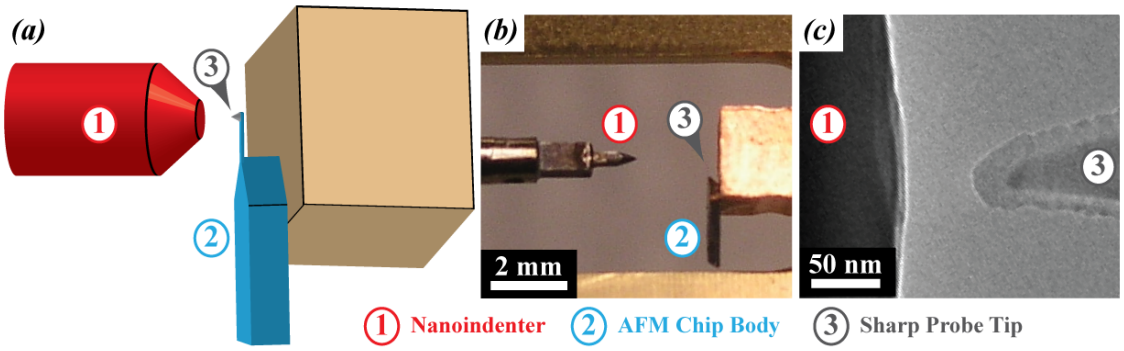

Figure 3.3: **A modified in situ indentation apparatus is used for adhesion and sliding tests.** The AFM probe is mounted on the sample surface such that the tip is accessible by the nanoindenter tip, as shown schematically in (a) and in an optical photograph in (b). Once inside the TEM (shown in (c)) the flat punch indenter (left, dark) is brought into adhesive or sliding contact with the nanoscale asperity (right, lighter grey). Figure reproduced with permission from Ref. (*1-6*, *9*).

3-2-3: Calibration of the indenter motion and the cantilever spring constant prior to testing

The three-dimensional piezoelectric positioning system was used for the vast majority of the testing described in later chapters since the transducer system is limited to motion along the indentation axis. Unlike the transducer, the piezoelectric stage is not "closed loop"; therefore it was calibrated using the TEM to measure the actual motion in each of the three dimensions as compared to the input value. Through an iterative process of parameter adjustment and motion measurement, the three independent conversion factors [V/nm] can be optimized. Additionally, the Hysitron control software permits active compensation to minimize motion in axes other than the desired axis of motion (e.g. when the user inputs a motion of 100 nm along the *x*-axis and the tip moves

by 100 nm in *x and* by 5 nm in *y*). Additional conversion factors [V/V] determine the amount of concurrent actuation of each "off-axis" piezo that is required during motion along each axis. These conversion factors are also optimized through an iterative process of adjustment and measurement.

To calibrate the spring constant of the cantilever (i.e. the force measurement device), the Sader method (*5*, *6*, *10*, *11*) was used. The plan-view dimensions of the cantilevers are measured using a white-light interferometer (NewView 6000, Zygo) or an SEM (FEI Strata Dual Beam 235 FIB/SEM), then the cantilever resonance curves are measured using an AFM (Asylum Research MFP-3D). Through extraction of the natural resonance frequency of the cantilever and also its quality factor, the cantilever's normal spring constant can be calculated (*7*, *8*, *10*, *11*).

3-3: Test methodology for in situ *adhesion and wear tests inside the TEM*

3-3-1: Mounting of AFM chips for testing

Prior to mounting, many commercial AFM probes are imaged using the technique described in Sect. 3-1; probes are selected for desired initial geometry and size. Following calibration (Sect. 3-2-3), the body of the 3 mm-long AFM chip is cleaved at roughly the midpoint to reduce the length dimension such that it will fit inside the sample mount of the nanoindenter. To prepare the chip for cleaving, surface flaws are introduced on the tip-side surface of the AFM chip using a diamond scribe. Then, the AFM chip is carefully broken using a three-point bend loading configuration that is introduced using two pairs of tweezers – one with a tine underneath the center of the AFM chip, the other

pair pushing down on the edges. It is easiest to do this cleaving on a lightly adhesive surface (such as "Post-It Note" tape, 3M Model 658, 3M), which has been mounted adhesive-side-up on top of double-sided tape. This lightly-adhesive surface assists in holding the chip in place during cleavage and minimizes the loss of the freshly cleaved pieces, yet is not so adhesive as to transfer adhesive material to the surfaces of the chips.

The cleaved AFM chip is then bonded to the sample mount using a TEM-compatible adhesive (Pelco Crystalbond 555). The chosen adhesive is solid at room temperature – thus providing a robust and rigid mounting of the base of the AFM chip – but flows like a liquid at temperatures exceeding 150° C. Therefore, the mounting is done on a hot plate that is mounted in the field of view of a binocular microscope. This is most easily done using a mounting fixture (such as a pair of self-closing tweezers) to securely hold the sample mount in place on the surface of the hot plate. The procedure is as follows:

1. An extremely small chip of adhesive is placed (at room temperature) on the sample mount.
2. The temperature of the hot plate is slowly increased (under observation) until the adhesive flows with a low apparent viscosity (as assessed qualitatively using tweezers to displace it). Care must be taken not to overheat the adhesive or it will decompose.

While the hot plate is heated and the adhesive is liquid-like, steps 3-7 are carried out:

3. Tweezers or a razor blade can be used to remove excess adhesive, such that a very thin film (with a small plan-view) remains on the sample mount. (The adhesive

should appear two-dimensional on the surface of the sample mount; if a "droplet" shape is observed, there is too much adhesive present.)

4. Tweezers are used to place the cleaved AFM chip on top of the adhesive.
5. Tweezers are used to apply pressure to the top surface of the cleaved AFM chip to ensure that it is flush against the top surface of the sample mount.
6. Tweezers are used to push the cleaved AFM chip around in the plane of view of the microscope to ensure that the sharp tip (located at the end of the cantilever) is located in the center of the sample mount.
7. Steps 5 and 6 are iterated until the AFM chip is satisfactorily mounted.
8. The hot plate is turned off and the sample mount allowed to cool until the adhesive becomes solid. (The cooling can be accelerated by removing the whole mounting apparatus (sample mount plus self-closing tweezers (or mounting clip)) from the hot plate onto a separate (heat-resistant) surface.)

As mentioned, care must be taken in mounting the AFM probe such that the sharp tip is centered on the sample mount so that it is accessible by the indenter tip. Also, the *least possible amount* of adhesive must be used (while still maintaining a secure bond). This ensures that the adhesive layer is extremely thin, such that the bottom surface of AFM chip is flat on the sample mount. (This ensures reproducible orientation of the AFM chip in the TEM, and ensures that the long axis of the conical tip is parallel to the axis of goniometer tilt (to enable the orientation method described in Sect. 3-1-3).

Finally, to ensure conductivity between the silicon probe (which is n-type doped to have low electrical resistance) and the brass sample mount, a conductive path should be painted using quick-drying carbon paint.

3-3-2: Materials selection and surface preparation for adhesion and wear testing

While the nanoindenter tips are interchangeable, the probe used for the majority of testing was a diamond flat punch tip with a diameter of 1 μm, which serves as the counter-surface for contact and/or sliding. As mentioned, a commercial AFM probe is rigidly mounted in place of a traditional indentation sample, such that its sharp (R = 2-100 nm) tip serves as a single-asperity contact. Various types of probes were used in the present investigation: wear and adhesion testing was conducted using silicon probes (Nanosensors PPP-CONT); adhesion testing was conducted using the same silicon AFM chips coated with either 20 nm of diamond-like carbon (DLC) using a plasma immersion ion deposition technique (as described in Ref. (*12*)) or with 100 nm of ultrananocrystalline diamond (UNCD) using hot-filament chemical vapor deposition (as described in Ref. (*13*). A single crystal diamond indenter tip was chosen, which has a truncated conical shape with a nominally-flat, (100)-oriented plateau apex approximately 1 μm in diameter. The topography of the diamond punch has characterized[4] using an AFM (MFP-3D, Asylum Research, Santa Barbara, CA); the RMS roughness was 0.091 nm, as measured over several 100x100 nm^2 areas. The diamond has been Boron-doped to impart conductivity and prevent the build-up of static charge in the TEM. Diamond was chosen as the counter-surface for adhesion and wear tests for its inertness, hardness, and wear resistance; since the indenter tip is too thick to be electron

[4] Topography measurements on the diamond punch was performed by Graham Wabiszewski (PhD Candidate, Department of Mechanical Engineering and Applied Mechanics, University of Pennsylvania)

transparent, then any deformation that occurs in the indenter tip will be mostly unobservable. Instead, the material selection is designed so that deformation, material removal, and wear will be primarily localized in the AFM tip – and thus clearly visible in the TEM.

Before testing, the diamond punch was cleaned using the following procedure (a minor modification of the manufacturer's recommendations):

1. The indenter tip is carefully removed from the nanoindenter (according to the manufacturer's instructions for tip removal) and mounted onto the threaded nut of the "cleaning puck" provided with the nanoindenter.
2. The cotton material on the end of a cotton swab is loosened (using a pair of tweezers to progressively clamp and pull) to achieve an expanded and significantly softer material.
3. This softened cotton swab is saturated with high-purity acetone and swiped repeatedly over the sharp apex of the indenter tip, moving in the direction from the threaded base of the tip towards the sharp apex. This step is intended to mechanically remove any loosely bonded debris.
4. The previous step is followed immediately by spraying the tip with high-purity methanol.
5. Then the tip (on the cleaning puck) is ultrasonicated for 15 minutes in each of three high-purity organic solvents (acetone, iso-propanol, methanol). While obvious, it must be noted that significant care must be taken during transfer of the cleaning puck from one beaker to another to prevent the cleaning puck from turning upside down and landing on the indenter tip apex.

6. Finally, the tip is replaced on the nanoindenter, and either the SEM (top-down) or the TEM (side-view) can be used to assess the cleanliness of the tip.
7. In cases where contamination was persistent and not removed by these steps, a focused ion beam (FEI Strata Dual Beam 235 FIB/SEM) was used to remove surface material (tens of nm of depth). Care was taken to minimize beam damage to the remaining diamond surface material (i.e., using a high incidence angle for the cut, and repeating the procedure with decreasing beam current to reduce the damage induced by the previous cut.)
8. Finally, while mounted on the indenter, a five-minute hydrogen treatment in a plasma cleaner (Gatan Solarus 950) is used to remove surface contamination. This last step ideally occurs immediately prior to insertion into the TEM to minimize re-adsorption of surface contamination.

3-3-3: Methodology for in situ *adhesion testing*

Once samples are mounted and cleaned (discussed above), the indenter is inserted into the TEM and adhesion and wear tests were conducted between nanoscale AFM tips and the 1-μm plateau of the nanoindenter tip.

Prior to testing, the AFM tip is imaged in its out-of-contact state using a variety of magnifications ranging from 19,100 – 573,000 times magnification, and periodically higher (up to 1,130,000 times magnification). These images are used to characterize the shape of the tip in detail before testing, and permit much higher magnification images than are achievable during testing (when the surfaces are moving). Then, to conduct an

adhesion test, the diamond punch was brought toward the AFM probe at a rate of 1 nm/s. As the AFM tip and sample near each other, there is a "snap-in" event where the cantilever suddenly deflects to allow the tip and sample to come into contact. This snap-in event is well known in AFM, and occurs when the gradient of the interaction force between the two surfaces exceeds the spring constant of the cantilever (*14*). At separation distances larger than this point, any instantaneous fluctuations in separation are damped out by the restoring force of the cantilever – this represents stable equilibrium. The snap-in point represents the transition to unstable equilibrium, where slight perturbations in separation lead to a reduction in system energy and cause the tip to accelerate irreversibly towards the surface (*14*). The indenter tip plateau is then retracted from the AFM chip at a rate of 1 nm/s. The tip/sample contact is held together by adhesion, which causes the cantilever to elastically deflect toward the contact during retraction of the sample. At all points in the test, this elastic deflection, Δ, of the cantilever can be measured in the TEM and multiplied by the spring constant of the cantilever, k_{lever}, in order to calculate the total interaction force ($F_{total} = k_{lever} \cdot \Delta$). This is identical to the evaluation of forces in AFM testing. Eventually, the force due to elastic bending of the cantilever exceeds the force of adhesion between the tip and sample, and there is a "pull-off" event where the tip suddenly detaches from the sample and returns to the initial rest position, where there is no load on the cantilever.

At this point, the video is stopped and another set of high resolution out-of-contact images of the tip is taken. Alternatively, in some cases, multiple adhesion events were conducted in one video prior to the capture of the high-resolution out-of-contact images. The majority of testing was recorded using a video-rate camera at approximately

30 frames per second, and captured using a commercially available digital video recorder. The remainder of the tests were recorded with lower frame rate (1-2 fps), but better contrast and resolution, using the Digital Streaming Video module of Digital Micrograph (Gatan, Inc., Pleasanton, CA) and captured using VirtualDub (http://www.virtualdub.org/). For all tests, high-resolution lattice-resolved images (573 kX or higher) were captured immediately before and after testing (as mentioned above); however the videos were recorded at lower magnification (typically ranging from 19.1 kX to 95.5 kX) so that the larger field of view of the video could capture a wider range of motion. Example videos of typical adhesion and wear tests can be found in the Supplemental Information of associated with Refs. (*9*) and (*15*), respectively.

3-3-4: Methodology for in situ *wear testing*

To conduct wear testing, the plateau of the indenter tip was slowly advanced as above until contact with the AFM tip was achieved, then it was advanced further until the tip reaches the out-of-contact equilibrium point of the AFM probe. This last step ensures that the contact experiences only an adhesive load, with no additional tensile or compressive load applied. The majority of wear tests with only the adhesive load applied; however additional applied load can be imparted by additional advancement of the indenter tip. Then the indenter tip is translated laterally relative to the AFM tip at a specified rate (typically 20 nm/s, occasionally 4 nm/s) by any arbitrary distance – most commonly in reciprocal strokes of 100 nm each. Finally, when the desired amount of sliding has been reached, the indenter tip is retracted from the AFM probe, until the

contact separates (i.e. pull-off occurs, as described above). The sliding distance interval between high-resolution out-of-contact images (from which volume loss was calculated) was most commonly 100 or 200 nm, but in some tests was shortened initially to be more sensitive to the early stages of wear, and lengthened later in the tests to achieve longer total sliding distances.

3-4: Data processing: Analyzing and quantifying the images and video

3-4-1: Direct observation of tip shape and modification in the TEM images and video

In accordance with prior investigations in which *ex situ* imaging was used to study wearing asperities, the TEM images and video can be directly analyzed to yield information about how the tip shape had been deformed. Different deformation mechanisms observed include:

- Fracture – In some cases, material removal occurs suddenly and along a well-defined crystallographic plane that is not typically parallel to the flat surface. In some cases of fracture, the broken piece sticks to the tip or the counter-surface and remains clearly visible.
- Plastic deformation – In cases of high load, plastic deformation and nucleation of dislocations shows contrast changes in the single crystal material that indicate residual plastic strain.
- Homogeneous deformation – In some cases, the tip deformed plastically and even flowed homogeneously, resulting in gross changes in the tip shape and sometimes droplet-like shapes of transferred material on the counter-surface. In this

investigation, this deformation mechanism occurred most commonly in electron beam-sensitive materials such as silicon nitride.

3-4-2: Algorithms for extracting the outer profile of the AFM tips

While the observations and comparisons described in Sect. 3-4-1 are useful, quantitative analysis is crucial. Therefore, computational analysis routines were developed to extract the contour of the tip in a specific image (i.e. at a specific point in the adhesion or wear testing) and to more rigorously compare the shape evolution of the tip over the course of testing. Specifically, a MATLAB program (script name: *profileTracer_v2.m*) was developed[5] to take in a TEM image (in .tif format) and allow the user to manually select sequential points on the image that define the outer profile of the AFM tip. Using contrast changes apparent in the image, the user is able to trace the tip; the resultant set of *(x,y)* coordinates define a two-dimensional real-space contour, as shown in Fig. 3.4. This contour is saved and can be further analyzed, as discussed below.

An additional MATLAB program (script name: *edgeFindingProfileTracer_v2.m*) was developed[6] that used the edge finding algorithms that are built into MATLAB to define the contour automatically and nearly instantly. It was found that the automatic algorithms accurately defined tip contours in cases of high contrast, and worked especially well for SEM images, lower-magnification (<25 kX) TEM images, or

[5] This MATLAB script was developed in collaboration with Dr. David S. Grierson (then a post-doc in the Turner Research Group, Univ. of Wisconsin; currently CTO, systeMECH LLC.)
[6] This MATLAB script was developed in collaboration with Joel A. Lefever (PhD candidate, Department of Materials Science & Engineering, University of Pennsylvania)

materials that appeared dark due to thick geometries or high-atomic-number component materials. However, for typical high-resolution TEM images with electron transparent materials and thin or variable-thickness geometries, the automatic edge-finding routines were easily fooled by artificial contrast (e.g. thickness fringes) and TEM artifacts. In typical analysis of a set of data, the automatic routine is attempted first, but if the contours are inaccurate (as judged by eye), then the manual selection routine is used. Note that the same point-selection routine (manual or automatic) must be used for all elements in a single set of data so that meaningful comparisons can be made without the introduction of artifacts due to differences in tracing method.

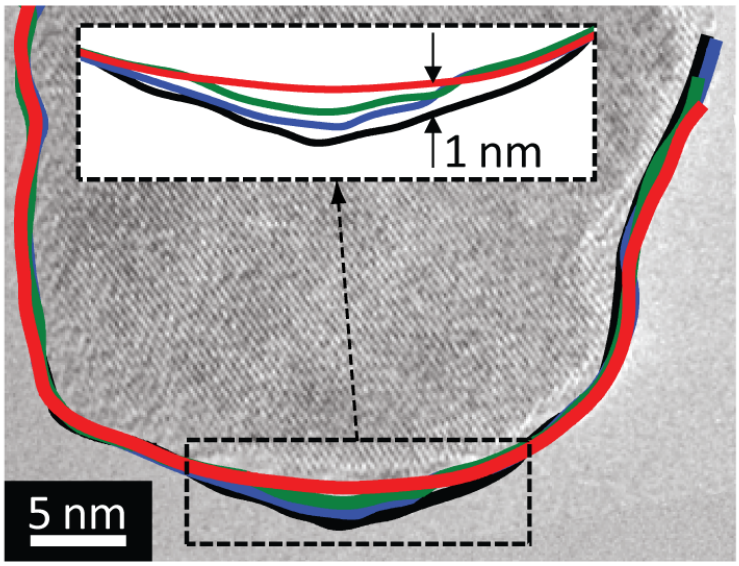

Figure 3.4: Algorithms were created to trace the contours of the probe at various points throughout a wear test.

3-4-3: Algorithms for fitting the overall tip shape, and computing its surface roughness

A MATLAB program (script name: *roughnessMeasurement_v2.m*) was created[7] for finding the mathematical function that best approximates the overall tip shape. As discussed in Chapter 2, standard contact mechanics models (Sect. 2-2-2) assume that the contacting bodies are spherical but with contact radii far below the sphere radius, thus, they approximate the bodies mathematically describe as paraboloids, i.e. their three-dimensional shape is defined by (*16*):

$$z_{tip}(r) = z_{paraboloid}(r) = \frac{r^2}{2R_{tip}}, \tag{3.1}$$

where r and z are the cylindrical polar spatial coordinates, and R_{tip} defines the radius of the overall parabolic shape. The quantity R_{tip} is then used as in input to the aforementioned models to calculate such quantities as contact area. In cases where the tip cannot be well-fit to a parabola, the algorithm allows the user to choose to fit with a more complex shape, such as a higher-order power-law shape. Continuum models (such as in Ref. (*17*)) have been developed to calculate contact parameters for geometries with such power-law shapes defined by Eq. 2 of Ref. (*17*), which, for 'S' parameter set to 1, reduces to:

$$z_{tip}(r) = z_{power-law}(r) = \frac{r^n}{nR_{tip}^{n-1}}. \tag{3.2}$$

This equation corresponds to a tip shape with a flatter end, which is a reasonable description of a tip that has been worn against a smooth surface.

[7] This MATLAB script was developed in collaboration with Dr. David S. Grierson (then a post-doc in the Turner Research Group, Univ. of Wisconsin; currently CTO, systeMECH LLC.)

Finally, a MATLAB program (script name: *roughnessMeasurement_v2.m*) was also developed[8] for characterizing the roughness of AFM tips imaged in the TEM. After the outermost contour of the high-magnification side view of the tip is traced, as discussed above, a parabola is fit to contour. This parabola captures the overall shape (ignoring surface roughness) of the asperity and allows the best-fit radius R_{tip} to be extracted; this quantity is needed for comparison with continuum mechanics models such as the DMT model (discussed in Chapter 2). The tip contour is compared to the best-fit parabola, and each traced point was characterized by the magnitude of its distance away from that best-fit parabola. Intuitively, this can be understood as subtracting the overall (parabolic) shape from the actual shape to yield a roughness profile similar to what would be measured on an equivalently rough planar surface. Once this equivalent profile was obtained, typical roughness characterizations could be performed on it, such as calculation of root-mean-square (RMS) roughness value R_q, average roughness, standard deviation of asperity heights, and other quantities (all defined, for example, in Ref. (*18*)).

3-4-4: Algorithm for extracting the snap-in distance and pull-off force from videos of tests

All adhesion and wear testing is recorded using real-time video, and the deflection distance Δ of the cantilever provides a measure of the total force F_{total} applied to the contact. Thus, a MATLAB program (script name: *videoAnalysis_v2.m*) was developed[9] for to allow the user to specify relevant frames, extract the cantilever deflection from

[8] This MATLAB script was developed in collaboration with Joel A. Lefever (PhD candidate, Department of Materials Science & Engineering, University of Pennsylvania)
[9] This MATLAB script was developed in collaboration with Joel A. Lefever (PhD candidate, Department of Materials Science & Engineering, University of Pennsylvania)

those frames, and thus compute contact forces. The code allows the user to do the following: (1) input a video file of an adhesion or wear test; (2) trace the tip profile (as discussed in Sect. 3-2-2) or input a previously saved trace; (3) find the relevant comparison frames (for instance, the frames immediately before and after a pull-off event); (4) move the profile trace around manually until it is correctly located on the tip in each of the relevant frames; (5) compute the distance of motion between frames – either the total distance, or the resolved distance along a particular axis (e.g. the cantilever deflection axis). Further, an optional component of the code was developed for cases where the tip position is hard to resolve due to indenter vibration or poor video contrast. In this, the user can specify a range of possible tip positions that are compatible with the current frame, and the algorithm will yield a propagated uncertainty in the calculation of total cantilever deflection.

3-4-5: Algorithms for integrating the interaction potential and computing relevant quantities

As discussed in Sect. 2-2-1, many continuum models (such as Refs. (*19*, *20*)) assume a tip shape or use of an analytical expression to define it, then integrate an interaction potential over this assumed shape. An improvement upon this method is presented here, where the integration is done over the *actual* traced tip profile. To create a three-dimensional shape from a two-dimensional contour the tip is assumed to have a circular profile at any height. Note that this does not assume global axisymmetry about a single axis of rotation (as is true for a right cone), but assume local axisymmetry, with the potential for different axes of rotation at different locations along the height (z-axis) of the tip. This assumes that the surface of the probe is free of localized contamination or

wear debris, and that the axis of the probe is pointing downward (the image was rotated prior to analysis to optimize this). TEM images taken at a variety of tilt angles inside the TEM demonstrate that the assumption of circular cross-section is reasonable – except where clearly localized material is visible or immediately after a large fracture event has occurred along a defined crystallographic plane. In the case of multiple protrusions on the end of the tip, this assumption of local axisymmetry is assumed to apply separately to each.

A MATLAB program (script name: *forceVsSeparation_integration_v2.m*) has been developed to perform this integration and calculate the effective total tip/surface interaction potential. The force of interaction $F_{interaction}$ between the tip and the sample is calculated as the integral of an interaction potential between vertically aligned differential elements of the two bodies. The specific interaction potential used was the Lennard-Jones 3-9 surface potential (see Chapter 2), such that $F_{interaction}$ is defined as:

$$F = \int_{Area} \sigma_{normal}\left(z_{sep}\right) dA = \int_0^{2\pi} \int_0^{\infty} \sigma_{normal}\left(z_{sep}(r,\theta)\right) r\, dr\, d\theta =$$

$$= \int_0^{\infty} \left\{ \frac{8W_{adh}}{3z_0} \left[\left(\frac{z_0}{z_{sep}(r)} \right)^3 - \left(\frac{z_0}{z_{sep}(r)} \right)^9 \right] \right\} 2\pi r\, dr \quad , \tag{3.3}$$

where σ_{normal} is the stress acting between two vertically aligned differential elements of area separated by z_{sep}, and z_0 is the equilibrium separation between flat surfaces. In this case, $z_{sep} = z_{tip} + d$, where d is the distance of closest approach between tip and sample. Note that the code is currently written to allow the user to choose between the Lennard-Jones 3-9 potential and a Dugdale square well potential; it could be readily expanded to

use any arbitrary potential. This code allows the user to calculate the force-vs-separation curve for any arbitrary tip shape. From that curve, the distance at which "snap-in" occurs and the force at which "pull-off" occurs can be readily calculated.

The previously described code allows the user to specify a work of adhesion W_{adh} and a value for the adhesive range z_0, and calculates the pull-off force and the snap-in distance for a given tip geometry. However, as discussed in Chapter 2, these values (particularly z_0) are not typically known *a priori* and are not easy to measure experimentally. By contrast, the pull-off force and snap-in distance for a given tip are easily measured using the present test methodology. Therefore, an additional MATLAB program (script name: *forceVsSeparation_varyZ0varyGamma_v5.m*) has been written to solve the reverse problem from that described in the previous paragraph; the user inputs the measured snap-in distance and pull-off force and the algorithm computes the values of work of adhesion and adhesive range that would produce these values.

The routines described in the previous paragraphs are used to calculate relevant parameters in Chapters 3 and 4.

3-4-6: Algorithms for aligning pre-/post-wear contours and calculating volume lost

The high-resolution out-of-contact still images of the TEM taken before and after a sliding wear test can be used to trace tip contours with high precision. A MATLAB program (script name: *optimizeProfileAlignment_v2.m*) was developed to align these traces and compute their volume change. Specifically, different contours of a single tip were taken at various points throughout a wear test, and these could be aligned based on

the shapes of the unworn shanks. Thus, a trace from a tip (example shown in Fig. 3.5(a)) is compared to a trace from the same tip that was taken earlier in the wear test. The profiles' upper (unworn) portions were then aligned spatially using an optimization algorithm that minimizes the "mismatch parameter," defined as the average lateral displacement of the unworn portions of the profiles (Fig. 3.5(b)). Once aligned, the profiles were integrated using a method of disks (Fig. 3.5(c)) to calculate a three-dimensional volume (Fig. 3.5(d)). The volume lost was then calculated by comparing the volumes of the asperity at various points in the wear test.

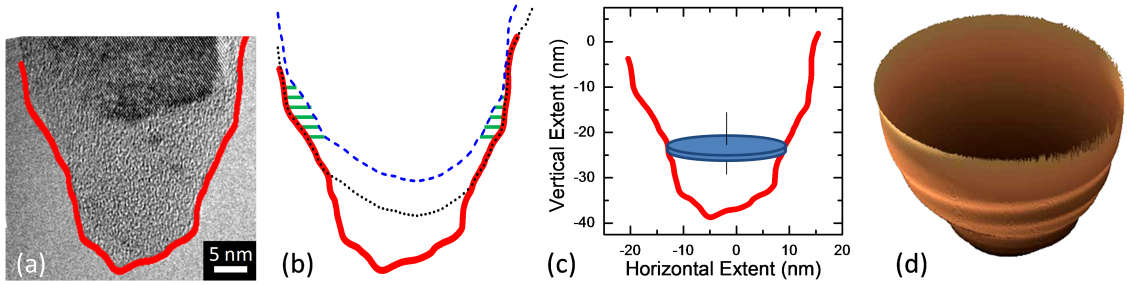

Figure 3.5: Lattice-resolved out-of-contact images of the tip were used to calculate the instantaneous volume lost at various points throughout the wear test. The high-resolution TEM images were traced (a) to extract the profile of the asperity at various intervals throughout the wear test. Profiles of the same asperity after different amounts of wear were aligned using an optimization routine (b). Here a reference profile (solid, red) is compared to a worn profile, which is shown both in good alignment (dotted, black) and in poor alignment (dashed, blue). Horizontal green lines schematically indicate the measured displacement between the two profiles, which is used to calculate the "mismatch parameter" used for optimization. Once aligned, the two-dimensional profiles were integrated using a method of disks (c) to create a three-dimensional shape (d), from which the volume and volume lost were measured. Figure reproduced with permission from Ref. (*15*).

There were three assumptions in the present method. First, the profiles are assumed to be perfectly aligned. While the optimization routine described is effective, the geometry of any particular tip will determine the sensitivity of the "mismatch

parameter" to deviations in alignment. In particular, tips that are rougher and have lower aspect ratio will be very sensitive to displacement (as shown in Fig. 3.5(b)) and will be easier to align, while the alignment will be more inaccurate for tips that are featureless and higher-aspect ratio. To quantify the effect of this factor, an uncertainty value was quantified by re-computing volume loss at deviations +/-5% away from the optimum value of the mismatch parameter. An additional assumption arose from the integration using the method of disks, which assumes local (not global) axi-symmetry (*i.e.*, the asperity has a circular cross-section at every height), as discussed in Sect. 3-2-4. As mentioned, tilting in the TEM about the axis of the asperity prior to testing was used to confirm that this approximation is reasonable. While this effect is more difficult to quantify, it is predicted to be a smaller source of error than the alignment uncertainty discussed above. Finally, a third assumption inherent in this analysis is that the volume change is due only to wear and not due to changes induced by the electron beam. The most common beam effects are deposition of carbonaceous films (*21*, *22*) and electron beam-induced damage or changes to the materials under study (*23*, *24*). To reduce the impact of these processes, beam exposure is minimized as much as possible (imaging quickly and with minimum possible brightness during active testing and deflecting the beam to a safe location far from the test sample at all other times). The effect of these processes was tested using mocks wear test (tests conducted using identical imaging and beam conditions, with no actual tip/surface contact taking place), and the "volume loss" in these was found to be within the noise level of the wear measurements.

3-5: References

(1) Huttl, G.; Klemm, V.; Popp, R.; Simon, F.; Muller, E. Tailored colloidal AFM probes and their TEM investigation. *Surf. Interface Anal.* **2002**, *33*, 50–53.

(2) Chung, K.; Lee, Y.; Kim, D. Characteristics of fracture during the approach process and wear mechanism of a silicon AFM tip. *Ultramicroscopy* **2005**, *102*, 161–171.

(3) Chung, K.; Kim, D. Fundamental investigation of micro wear rate using an atomic force microscope. *Tribol. Lett.* **2003**, *15*, 135–144.

(4) Chung, K.-H.; Kim, D.-E. Wear characteristics of diamond-coated atomic force microscope probe. *Ultramicroscopy* **2007**, *108*, 1–10.

(5) Liu, J.; Notbohm, J. K.; Carpick, R. W.; Turner, K. T. Method for characterizing nanoscale wear of atomic force microscope tips. *ACS Nano.* **2010**, *4*, 3763–3772.

(6) Liu, J.; Grierson, D.; Moldovan, N.; Notbohm, J.; Li, S.; Jaroenapibal, P.; O'Connor, S.; Sumant, A.; Neelakantan, N.; Carlisle, J. Preventing nanoscale wear of atomic force microscopy tips through the use of monolithic ultrananocrystalline diamond probes. *Small* **2010**, *6*, 1140–1149.

(7) Minor, A. M.; Morris, J. W.; Stach, E. A. Quantitative in situ nanoindentation in an electron microscope. *Appl. Phys. Lett.* **2001**, *79*, 1625–1627.

(8) Stach, E. A.; Freeman, T.; Minor, A. M.; Owen, D. K.; Cumings, J.; Wall, M. A.; Chraska, T.; Hull, R.; Morris, J. W.; Zettl, A. Development of a nanoindenter for in situ transmission electron microscopy. *Microsc Microanal* **2001**, *7*, 507–517.

(9) Jacobs, T. D. B.; Ryan, K. E.; Keating, P. L.; Grierson, D. S.; Lefever, J. A.; Turner, K. T.; Harrison, J. A.; Carpick, R. W. The Effect of Atomic-Scale Roughness on the Adhesion of Nanoscale Asperities: A Combined Simulation and Experimental Investigation. *Tribol. Lett.* **2013**, *50*, 81–93.

(10) Sader, J.; Chon, J.; Mulvaney, P. Calibration of rectangular atomic force microscope cantilevers. *Rev. Sci. Instrum.* **1999**, *70*, 3967–3969.

(11) Sader, J. E.; Sanelli, J. A.; Adamson, B. D.; Monty, J. P.; Wei, X.; Crawford, S. A.; Friend, J. R.; Marusic, I.; Mulvaney, P.; Bieske, E. J. Spring constant calibration of atomic force microscope cantilevers of arbitrary shape. *Rev. Sci. Instrum.* **2012**, *83*, 103705.

(12) Bares, J. A.; Sumant, A. V.; Grierson, D. S.; Carpick, R. W.; Sridharan, K. Small amplitude reciprocating wear performance of diamond-like carbon films: dependence of film composition and counterface material. *Tribol. Lett.* **2007**, *27*, 79–88.

(13) Fletcher, P. C.; Felts, J. R.; Dai, Z.; Jacobs, T. D.; Zeng, H.; Lee, W.; Sheehan, P. E.; Carlisle, J. A.; Carpick, R. W.; King, W. P. Wear-Resistant Diamond Nanoprobe Tips with Integrated Silicon Heater for Tip-Based Nanomanufacturing. *ACS Nano.* **2010**, *4*, 3338–3344.

(14) Cappella, B.; Dietler, G. Force-distance curves by atomic force microscopy. *Surf Sci Rep* **1999**, *34*, 1–104.

(15) Jacobs, T. D. B.; Carpick, R. W. Nanoscale wear as a stress-assisted chemical reaction. *Nature Nanotech.* **2013**, *8*, 108–112.

(16) Johnson, K. L. *Contact Mechanics*; 2011; pp. 1–467.

(17) Grierson, D. S.; Liu, J.; Carpick, R. W.; Turner, K. T. Adhesion of nanoscale asperities with power-law profiles. *J. Mech. Phys. Sol.* **2013**, *61*, 597–610.

(18) Mate, C. M. *Tribology on the Small Scale: A Bottom Up Approach to Friction, Lubrication, and Wear*; Oxford University Press: Oxford, UK, 2008.

(19) Maugis, D. Adhesion of spheres: the JKR-DMT transition using a Dugdale model. *J. Coll. Int. Sci.* **1992**, *150*, 243–269.

(20) Zheng, Z.; Yu, J. Using the Dugdale approximation to match a specific interaction in the adhesive contact of elastic objects. *J. Coll. Int. Sci.* **2007**, *310*, 27–34.

(21) Reimer, L.; Wächter, M. Contribution to the contamination problem in transmission electron microscopy. *Ultramicroscopy* **1978**, *3*, 169–174.
(22) Wei, X.; Liu, Y.; Chen, Q.; Peng, L. Controlling electron-beam-induced carbon deposition on carbon nanotubes by Joule heating. *Nanotechnology* **2008**, *19*, 355304.
(23) Zheng, K.; Wang, C.; Cheng, Y.-Q.; Yue, Y.; Han, X.; Zhang, Z.; Shan, Z.; Mao, S. X.; Ye, M.; Yin, Y.; Ma, E. Electron-beam-assisted superplastic shaping of nanoscale amorphous silica. *Nat Commun* **2010**, *1*, 24.
(24) Williams, D. B.; Carter, C. B. *The Transmission Electron Microscope*; Springer, 1996.

CHAPTER 4: Nanoscale adhesion: Part I - Quantifying adhesive interaction parameters

In Sect. 3-4-5, a novel method was described for combining measurements of the detailed geometry of a sharp tip with results from adhesion tests in order to measure fundamental adhesion parameters that previously were not experimentally accessible; specifically the work of adhesion W_{adh} and the range of adhesion z_0 between two surfaces. The present chapter begins by applying this method to artificial data – "probe tips" with standard shapes and arbitrarily chosen adhesion data. This allows for identification of the relevant trends that emerge, as well as validation of the proposed algorithms through comparison to previously published results. Later in the chapter, the method is applied to real data – nanoscale silicon atomic force microscopy probes in adhesive contact with a diamond substrate. The calculated work of adhesion compares favorably to other methods of measurement; more significantly, the range of adhesion is measured experimentally for the first time, and agrees with theoretical values.

4-1: Using an interaction potential to calculate expected adhesion values for model shapes

An adhesion potential provides a description of the stress acting between two opposing elements at any separation distance between those elements. This potential can be integrated over an arbitrary contact geometry to yield the net force acting between the two bodies at any separation distance between those bodies. Two related algorithms are described in Sect 3-4-5: one uses the tip shape and the adhesion parameters (work of

adhesion W_{adh} and range of adhesion z_0) as inputs, then calculates expected values for pull-off force $F_{adhesive}$ and snap-in distance z_{si} as outputs; the other uses the tip shape, pull-off force, and snap-in distance as inputs, then calculates the adhesion parameters (W_{adh}, z_0) as outputs. To minimize confusion, the former algorithm (W_{adh}, $z_0 \rightarrow F_{adhesive}$, z_{si}) is referred to periodically as the *forward calculation* (since it can be integrated directly) and the latter algorithm ($F_{adhesive}$, $z_{si} \rightarrow W_{adh}$, z_0) is referred to periodically as the *reverse calculation* (since it cannot be directly integrated, but rather relies on the integration of a large number of (W_{adh}, z_0) pairs, then uses a search routine to find the best one). In this section, results are presented from applying both algorithms to model "probes" of standard shapes are presented. The purpose of this section is not only to validate the functionality of the code, but also to point out relevant trends of behavior for different geometries; these trends will be referenced in the analysis of the real data.

4-1-1: Calculating tip-sample force-separation curves using probes with standardized shapes: the forward calculation

To review, the tip-sample interaction force (at any separation distance) can be calculated by applying a Lennard-Jones 3-9 surface potential to each differential area element, then integrating over the entire contact geometry. This approach and its assumptions are discussed in Sect. 2-2-3. As discussed, the underlying Lennard-Jones surface potential has two empirically-determined free parameters: the range of adhesion z_0, which scales the *length* over which the potential acts; and the work of adhesion W_{adh}, which is equal to the area of the attractive portion of the curve (as shown in Fig. 2.4).

To validate the approach and algorithms used in the present investigation, force-separation curves have been computed (using the forward calculation) for three different reference tips with shapes described by three simple analytical functions: a cylindrical flat punch; a paraboloid (i.e. a two-dimensional parabola that has been revolved about its central axis), and a right cone. These shapes were chosen as they represent extremes of tip shape, and they illustrate trends of behavior, as follows:

- Flat punch – This represents the bluntest possible tip and the closest approximation of two infinite flat surfaces coming into contact. The force-vs-separation curve for this tip represents the form of the underlying Lennard-Jones surface potential (differing only by a constant).
- Paraboloid – This shape was chosen as it is used in many contact mechanics models (see Sect. 2-2-2) as an approximation for a sphere (accurate when the contact radius is significantly smaller than the tip radius). It represents an intermediate sharpness between the flat punch and the cone. As discussed later, it represents a special case of adhesion.
- Right cone – This shape represents the extreme of the sharpest possible probe, converging to a single point at the apex. This unphysically sharp analytical shape is useful for demonstrating trends, and also a limitation of the present model.

The three shapes are shown in Fig. 4.1. Their specific geometries were chosen to achieve similar values of minimum interaction force (i.e. maximum value of attractive force, $F_{adhesive}$) for physically reasonable values of $W_{adh} = 0.30$ J/m^2 and $z_0 = 0.1$ nm (in

the range proposed by Ref. (*1*). This yielded a flat punch of end radius 0.4 nm; a paraboloid defined by Eq. 3.1 and an input radius R_{tip} of 0.8 nm; and a right cone with a circular base of diameter of 100 nm and a height of 20 nm (for an opening half-angle of 70°). Figure 4.1 shows the force-separation curves for each shape, calculated using the parameters given above (W_{adh} = 0.30 and 0.60 J/m^2, z_0 = 0.1 and 0.3 nm). These plots are included to show the effects of W_{adh} and z_0, and the differences in behavior for each shape.

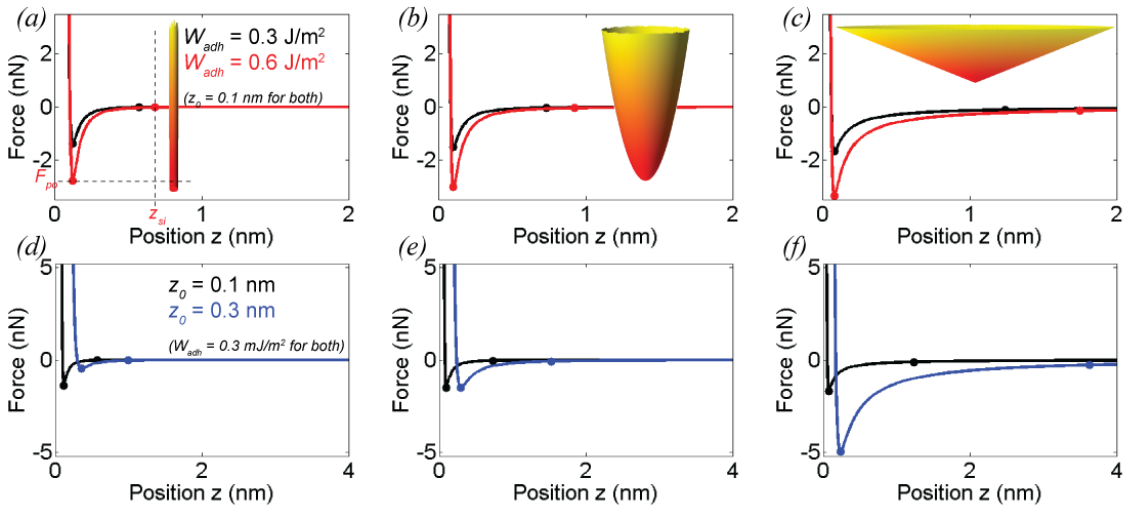

Figure 4.1: Force-separation curves were calculated for standardized shapes to establish trends of behavior and to allow for comparison with previously published results. Preliminary tests were performed of the adhesion model using three artificially shaped probes: a flat punch (shown in (a)), a paraboloid (b), and a right cone (c). Shapes are not shown on the same scale, each is 20 nm tall - see text for full geometric details. Here, the tip/sample interaction force is calculated over a range of tip positions, with the flat substrate at z = 0. These force-separation curves are shown (a-c) for two different values of the work of adhesion (W_{adh} = 0.3, 0.6 J/m^2) at a constant value of range of adhesion (z_0 = 0.1 nm). Similarly, in (d-f), force curves are compared for two different ranges of adhesion (z_0 = 0.1, 0.3 nm) and a constant work of adhesion (W_{adh} = 0.3, 0.6 J/m^2). The points on the curves corresponding to pull-off and snap-in are labeled in each plot with circular points; values of pull-off force (F_{po}) and snap-in distance (d_{si}) are explicitly indicated in (a). The effect of range of adhesion on pull-off force varies for different shapes. The spring constant of the cantilever is assumed to be 0.1 N/m in all cases.

For all probe shapes, a larger value of work of adhesion results in interaction forces that are uniformly larger; therefore both the pull-off force and the snap-in distance increase monotonically with W_{adh}. Note that the pull-off force scales linearly with W_{adh} in all cases; in contrast, while the snap-in distance increases with W_{adh}, it does not obey a simple functional dependence.

The dependence of pull-off and snap-in on the range of adhesion z_0 is more complex, and depends strongly on the geometry of the tip. For a flat punch (and for the underlying Lennard-Jones surface potential), the pull-off force decreases as z_0 is increased. All trends shown here can be compared with recent papers (*2*, *3*) discussing adhesion of power-law shapes of the form $z \propto r^n$ where z and r represent cylindrical polar coordinates, and n is the so-called power exponent. A flat punch tip like the one used here is equivalent to a power-law shape with a very large power exponent ($n \rightarrow \infty$). The trend of decreasing adhesive force with increasing z_0 directly agrees with the trend shown in Grierson *et al.* (*2*) for all shapes with power law exponent $n > 2$. By contrast, for the parabolic tip (a power-law shape where the power exponent $n = 2$), the pull-off force is unaffected by the choice of z_0. This is in agreement not only with trends from Refs. (*2*, *3*), but also with the Maugis-Dugdale model (*4*) (Sect. 2-2-3). The pull-off force agrees exactly with the prediction of the Bradley limit for rigid spheres and that of the DMT model (Sect. 2-2-2): namely, that pull-off force is equal to $2\pi R_{tip} W_{adh}$. Finally, for the conical shape, the pull-off force *increases* as z_0 is increased for a constant W_{adh}. This trend for a conical shape (a power-law shape where the power exponent $n = 1$) is in direct agreement with the so-called DMT-*n* limit described by Zheng and Yu (*3*).

In summary, for the probe shapes shown in Fig. 4.1 and others shapes tested (not shown), consistent trends of behavior hold:

- for shapes blunter than a paraboloid ($n > 2$), the pull-off force *decreases* as z_0 *increases*;
- for shapes sharper than a paraboloid ($n < 2$), the pull-off force *increases* with z_0;

and for a paraboloid ($n = 2$), the pull-off force *is unaffected* by changes in z_0. (Note that, for rigid tips, the JKR limit (with its modified pull-off force) is not reached.)

The dependence of pull-off force on adhesive range can be understood as a competition between two factors: as the range of adhesion is increased, a larger section of the probe contributes to the adhesive interaction, but the adhesive stress on a given element at a given separation is decreased (to maintain a constant work of adhesion in the underlying Lennard-Jones potential). The "winner" of this competition is determined by the geometry of the body. A parabola represents the shape where these competing effects exactly balance, and furthermore, this holds regardless of the chosen interaction potential (*5*) – in this case, the pull-off force depends only on the work of adhesion W_{adh}. For sharper shapes, the geometric effect dominates, and for blunter shapes the weakening of the adhesive stress dominates.

4-1-2: Restricting the minimum tip-sample separation distance to the value of the adhesive range

Another important result emerges from Fig. 4.1: without some modification, a simple integration of the Lennard-Jones surface potential leads to an unphysical result

when the finite rigidity and strength of the materials are considered. Specifically, for any shapes that are sharper than a parabola, the separation distance corresponding to the minimum force (F_{po}) will be smaller than the equilibrium flat-on-flat separation z_0. To be explicit, z_0 rigorously designates the equilibrium separation of *surfaces*, but is not the same as the equilibrium separation of the *bodies* once integrated over the tip/sample contact. This is illustrated more specifically in Fig. 4.2. Since the Lennard-Jones surface potential rapidly increases at separation distances below z_0, this can result in unphysically high local compressive stresses on the closest elements. Since the model assumes rigid tips, the elements that are closest have to support infinitely large stresses without deformation or fracture. This is unrealistic for two reasons: first, the interaction of the two surfaces is *not* solely mitigated by surface-surface interactions, but instead includes the mechanical stiffness of the bodies themselves, which will provide an additional restoring force that is not accounted for by the present model; second, wherever the local stress does get extremely high, the shape of the bodies will deform (elastically or plastically) away from their out-of-contact shapes, thus reducing the local stress.

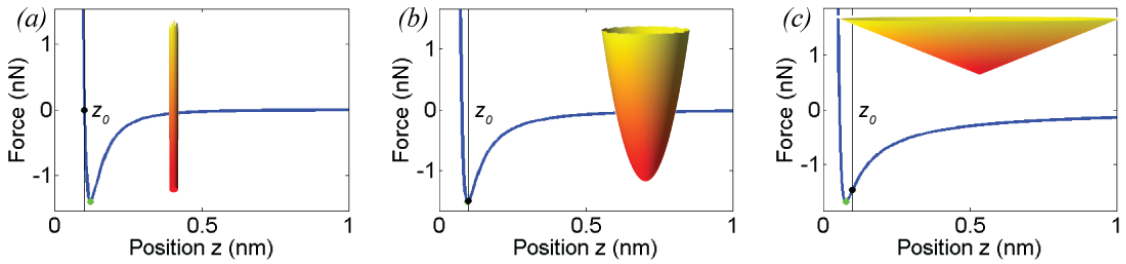

Figure 4.2: A minor modification to the model must be made to prevent extremely sharp tip apexes from developing unphysically high stresses. Force-separation curves are shown for the same three standard shapes shown in Fig. 4.1. Here, the value of z_0 is explicitly indicated with a black line and a black circle on the curve. For shapes such as the flat punch (a) and the paraboloid (b), the pull-off force (labeled with a green circle) occurs at separations larger or approximately equal to the range of adhesion z_0. However, the curve for the cone shape (c) shows that the minimum of the curve can occur at separations less than z_0. This leads to unphysically high local stresses at the tip apex. To prevent this, the minimum allowed separation is set to z_0. For many real tips, this change has little or no effect.

To eliminate the unphysically large Lennard-Jones stresses on the apex, an additional constraint was added to the present model: the tip-sample minimum separation distance cannot fall below the value of z_0 chosen for that simulation (i.e. $z_{sep} \geq z_0$). This constraint mimics the restoring force due to elasticity, by effectively assuming that the strain caused by repulsive contact between the bodies corresponds to an infinitely high elastic stress. In other words, hard-wall repulsion has been artificially introduced when the minimum separation of the bodies is z_0. For high-modulus materials and light loads (where the deformation due to strain is small), this assumption is expected to be reasonable. In particular, in the present use of the model on silicon and diamond where the *net* tip-sample interaction forces are all in the adhesive regime, this is expected to be a good approximation of reality. For comparison, one tip profile was tested using an

adhesion potential applied to an elastic tip as calculated using a finite element package[10]. For W_{adh} = 0.1 J/m^2, z_0 = 0.5 nm, the calculated pull-off force agreed with the present model within 2%.

4-1-3: Calculating adhesion parameters for the same standardized shapes: the reverse calculation

The calculations performed in the previous sections validated the underlying approach through comparison to previously published results, and also demonstrated trends of behavior with tip shape. There, values of pull-off force and snap-in distance were calculated for standard shapes and known adhesion parameters (W_{adh}, z_0). This section performs the reverse calculation: the specific calculated values of pull-off force and snap-in distance from the forward calculation are used as *inputs* and, along with probe shape, are used to extract adhesion parameters (W_{adh}, z_0). This is done purely for purposes of illustration and validation of the approach.

To clearly illustrate the method, a sample adhesion test is analyzed step-by-step as shown in Fig. 4.3. First, the shape of a real tip was traced using the procedure described in Sect. 3-4-2. The measured pull-off force for this tip was 84 nN and the measured snap-in distance was 6.9 nm. Pull-off forces corresponding to a wide range of (W_{adh}, z_0) pairs are calculated and plotted in Fig. 4.2(a). It is apparent that several different pairs of values can accurately describe the measured pull-off force. Therefore the solution using

[10] This test was performed by Dr. David S. Grierson, then a post-doc in the Turner Research Group, Univ. of Wisconsin; currently CTO, systeMECH LLC. The test was performed with Abaqus (Dassault Systèmes, Vélizy-Villacoublay, France), as described in Ref. (*2*).

pull-off force alone is not unique. However, a second independent measure is provided by the snap-in distance (Fig. 4.2(b)) that would be calculated for each corresponding pair of (W_{adh}, z_0). As shown in these figures, there is only one (W_{adh}, z_0) pair that accurately describes both pull-off force *and* snap-in distance. Note that Fig. 4.3 is intended to illustrate the method and only shows a coarse meshing of W_{adh} and z_0; the programs described in Sect. 3-4-5 use a far smaller spacing of tested values for W_{adh} and z_0 and a search algorithm is employed to find the best-fit values.

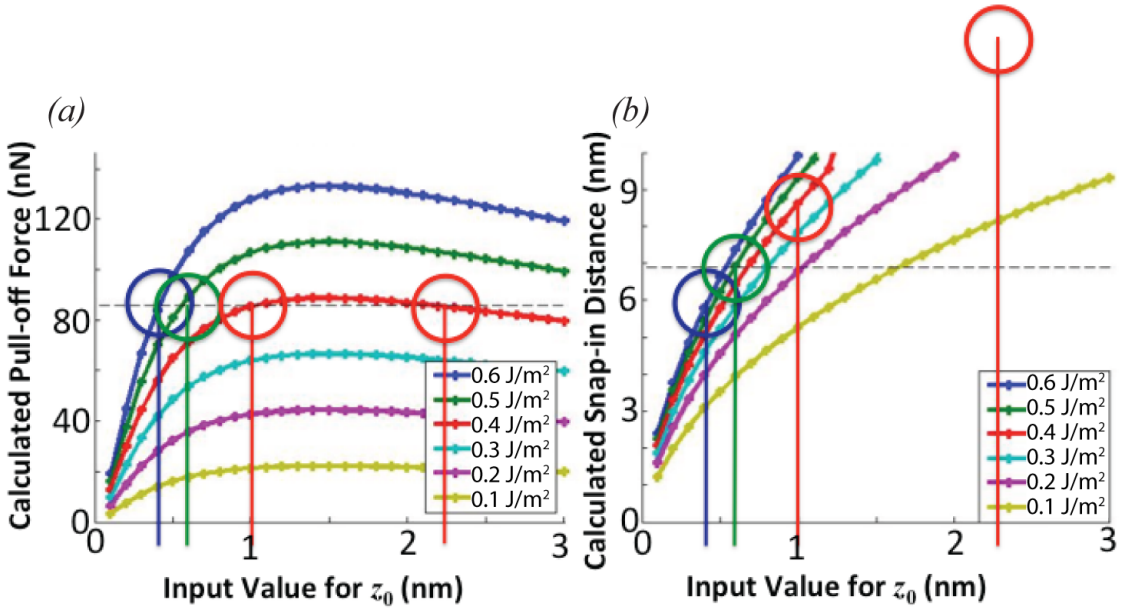

Figure 4.3: The approach is demonstrated for calculation of work of adhesion W_{adh} and range of adhesion z_0 based on quantities measured using *in situ* adhesion tests. Tests on a particular tip shape (not shown) yield example values of pull-off force and snap-in distance. The algorithms calculate possible pull-off forces for a wide range of (W_{adh}, z_0) pairs (colored data in (a)) – these are compared against the true pull-off force (black, dashed line). It is apparent that the solution is not unique – the four circles indicate four possible pairs of (W_{adh}, z_0) that accurately describe this pull-off force. The novel aspect of the present work is that the snap-in distance is used as an *independent* measure of adhesion. In (b), circles of corresponding color are calculated for the same four pairs of (W_{adh}, z_0) that were identified in (a). Three of the four *do not* match the snap-in distance, while the fourth *does*. Thus, the physically-reasonable values in this example are W_{adh} = 0.5 J/m^2 and z_0 = 0.6 nm.

To validate the reverse calculation, values from the previous section were tested. The goal was to see if the code could accurately extract the values of W_{adh} and z_0 that were chosen as inputs in the previous section (i.e. W_{adh} = 0.3 or 0.6 J/m^2 and z_0 = 0.1 or 0.3 nm. In all cases, the extracted pair of (W_{adh}, z_0) matched the originally chosen pair within 2%; in most cases, the agreement was within 1%. The same validation (W_{adh}, z_0 → $F_{adhesive}$, z_{si}, then $F_{adhesive}$, z_{si} → W_{adh}, z_0) was repeated for a trace of a real AFM tip, and a range of values of W_{adh} and z_0; in all cases, the input and extracted values agreed within 1%.

The primary conclusion from Sect. 4-1 is simply that the present approach works well for a wide range of shapes and inputs. The two algorithms calculate and back-calculate consistent values; and the trends in results agree with previously published reports investigating adhesion of probes with standard shapes defined by analytical functions. These trends demonstrate the dependence of pull-off force and snap-in distance on work of adhesion and range of adhesion for different classes of tip shape.

4-2: Measuring adhesive interaction parameters in real materials

Section 4-1 described the overall approach for the present analysis of nanoscale adhesion and demonstrated its success with artificial data. The same approach is applied in this section to real data taken from *in situ* adhesion tests. However, the previous analysis did not consider the fact that the indenter apparatus is subject to vibrations along the loading direction upon approach. This is important because these vibrations cause temporary reductions in the minimum separation distance below the average value

observed in the TEM. Therefore, Sect. 4-2-1 describes a method for accounting for these vibrations; then Sect. 4-2-2 describes the analysis.

4-2-1: Modification of the technique to account for vibration

As mentioned in Sect. 3-2-1, the spring-mounted indenter tool exhibits constant vibration at the natural resonance frequency of the force transducer, which for the present apparatus is 119.8 Hz. Therefore, the apparent position of the indenter tip in the video (which is captured at 30 frames per second) is the time-averaged position; the actual position of the spring-mounted indenter varies approximately sinusoidally around this average. Immediately prior to every set of experiments, several at-rest displacement measurements were taken to characterize the standard deviation of the vibration at that specific time and day. Typical vibration amplitudes varied from less than 0.75 nm of standard deviation up to more than 3 nm, depending on the time of day, which other equipment was active, and other external variables.

Since the spring constants of the cantilevers are low ($k \approx 0.1$ N/m), then this level of vibration has little effect on the measurement of applied load or of pull-off force – leading to variations of considerably less than 1 nN. However, as shown in Fig. 4.1, the tip-surface interaction force is exquisitely sensitive to variations in separation distance – down to the Ångström level. Further, the time scale needed for snap-in to occur is on the order of a single period of vibration of the AFM cantilever, which – for a typical resonance frequency of 10 kHz – is 0.1 ms. This is two orders of magnitude faster than the period of vibration of the nanoindenter tip. Therefore, the relevant distance for snap-

in is the smallest instantaneous distance between the AFM tip and the vibrating surface of the nanoindenter right before snap-in. This distance is smaller than the measured (time-averaged) distance $d_{snap\text{-}in,meas.}$ by the amplitude of vibration A_{vib} and, if the vibration is assumed to be perfectly sinusoidal, then the adjusted snap-in distance $d_{snap\text{-}in,true}$ is given by:

$$d_{snap-in,true} = d_{snap-in,meas.} - A_{vib} = d_{snap-in,meas.} - \sqrt{2}\sigma_{vib}, \tag{4.1}$$

where σ_{vib} is the standard deviation of vibration that is measured before each set of tests.

4-2-2: Measurement of adhesion parameters for a silicon tip on a diamond surface

Three different nanoscale tips were used in adhesion tests inside the TEM (Sect. 3-3-3). High-magnification images were taken before and after testing, as shown in Fig. 4.4. Real-time video was used to capture the dynamic snap-in and pull-off events, the values of which are recorded in Table 4.1.

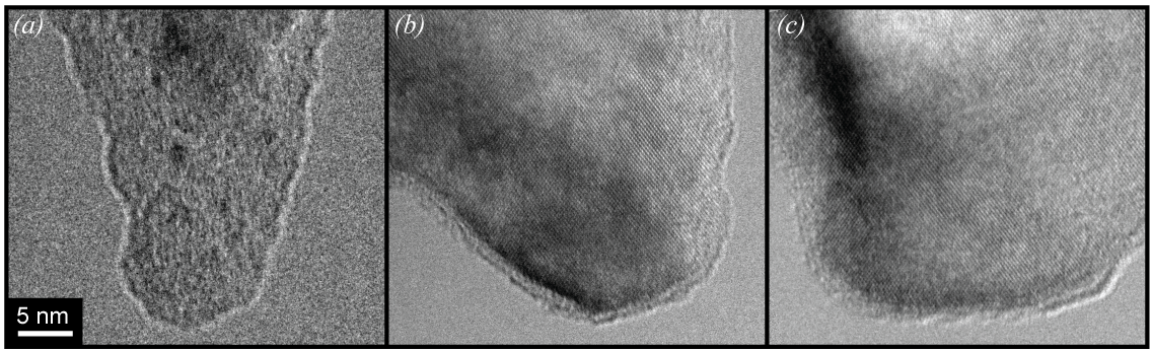

Figure 4.2: *In situ* adhesion tests were performed on three tips of varying sharpness and geometry. The three tips are shown at a common magnification.

Table 4.1: Measured and calculated values for the three probes shown in Fig. 4.4.

Tip image	Measured F_{po} [nN]	Measured d_{si} [nm]	St. dev. of vibration [nm]	Amplitude of vibration [nm]	Vibration-adjusted d_{si} [nm]	Calculated W_{adh} [J/m^2]	Calculated z_0 [nm]
Fig 4.4(a)	26.55	5.37	1.21	1.71	3.66	0.898	0.28
	41.80	5.16	1.21	1.71	3.45	0.693	0.23
Fig 4.4(b)	14.45	6.11	2.67	3.77	2.34	0.616	0.23
	15.74	7.01	2.67	3.77	3.24	0.667	0.31
	22.17	5.91	2.67	3.77	2.14	0.565	0.16
	57.32	5.90	1.34	1.90	4.00	0.433	0.20
Fig 4.4(c)	66.42	7.60	1.34	1.90	5.70	0.623	0.33
	69.66	6.90	1.34	1.90	5.00	0.795	0.22

The results obtained using the present method are shown in Fig. 4.5. There were thirteen distinct adhesion tests performed using three different tips. These represent the cases where high-resolution profiles could be combined with adhesion tests performed in the absence of sliding, and with sufficient resolution of the snap-in and pull-off events. For the first two probes (labeled Probe 1 and Probe 2), two adhesion tests were performed between each high-resolution image. For the Probe 3, high-resolution images were taken before and after each pull-off event. The averaged values for the calculated parameters are $W_{adh} = 0.66 \pm 0.14$ J/m^2 and $z_0 = 0.25 \pm 0.06$ nm.

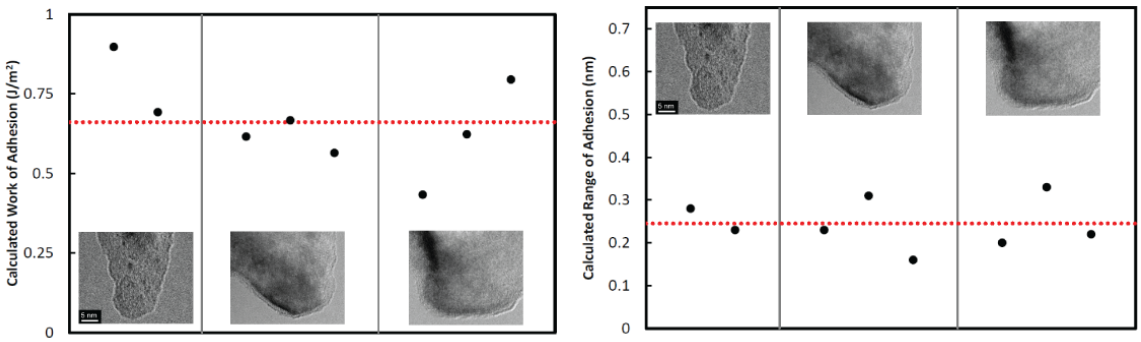

Figure 4.5: Using the novel algorithm values of work of adhesion and range of adhesion are extracted simultaneously from *in situ* adhesion tests. The calculated data for each of the three probes is shown: work of adhesion (a) and range of adhesion (b). There is scatter in the data corresponding to a standard deviation of 20%, but the average values are physically reasonable as compared to other techniques for estimation or measurement.

4-3: Assessing the reliability of the measured parameters

First, it must be determined whether these results are even physically possible. An upper bound on the work of adhesion is the cleavage energy of a perfect crystal. This value ranges over 1.5 – 1.9 J/m^2 for silicon (*6*) and over 11.1 – 19.9 J/m^2 for diamond (*7*) (values can vary depending on crystallographic plane and method of measurement/calculation). Since the range of adhesion z_0 is also the flat-surface equilibrium separation, then an upper bound can be identified because no clear gap was observed between the bodies while in contact. For instance, if z_0 = 2 nm, then the separation between the two bodies would be easily resolvable in the TEM. Because of the vibration of the instrument and the lower magnification of the real-time videos, a gap of 0.5 nm or even larger *could* go unnoticed, but an equilibrium separation larger than

1 nm can be expressly ruled out. Such a large gap would be visible. Both of the measured values fall within the absolute limits of what is physically reasonable.

4-3-1: Comparing the range of adhesion with previously proposed values

To assess how correctness of the measured value of z_0, there are two different bodies of literature that can be consulted: values used in continuum contact mechanics investigations; and values calculated from atomistic simulations – converting the empirical parameters from a well-established interatomic potential into those for the resulting surface potential. The present result (z_0 = 0.25 nm) compares favorably against most estimates used in continuum mechanics investigations. Various values were proposed in at least twelve previously published reports ranging from purely theoretical calculations to fits to experimental data (as shown in Table 4.2). Ten of the twelve propose that z_0 is either equal to the interatomic spacing of the materials (0.154 nm in diamond and 0.234 nm in silicon) or some similar absolute value, such as 0.2 nm or 0.3 nm. The other two reports (Refs. (*8*) and (*2*)) estimate the adhesive range h (the width of the Dugdale potential – slightly different in physical meaning from z_0, but typically assumed to be of equal magnitude (see, for example, Ref. (*8*)) as 1 nm and 4-5 nm, respectively. Value of z_0 of these magnitudes can be ruled out in the present study as such a gap would be readily visible. It should be noted that there could be other adhesive interactions not captured by the Lennard-Jones potential which could act at this distance (such as capillarity or electrostatic attraction), but these are not likely to be

active in the present investigation since the contact is in high vacuum and the bodies are doped to impart high conductivity.

Table 4.2: Values of z_0 that have been proposed in previously published investigations.

Proposed z_0 (nm)	Estimated or fit to data	Materials (if applicable)	Ref.
0.15 - 0.23 [a]	Estimated		*(5)*
0.15 - 0.23 [a]	Estimated		*(4)*
0.15 - 0.23 [a]	Estimated		*(9)*
0.15 - 0.23 [a]	Estimated		*(10)*
0.15 - 0.23 [a]	Estimated		*(11)*
0.3	Estimated		*(12)*
1	Estimated		*(8)*
0.15	Used to fit data	tungsten carbide / diamond	*(1)*
0.2	Used to fit data	platinum / mica	*(13)*
0.2	Used to fit data	tungsten carbide / diamond	*(14)*
0.3	Used to fit data	glass / platinum	*(15)*
0.3	Used to fit data	silicon / TiO_2	*(16)*
4 - 5	Used to fit data	DLC / DLC	*(2)*

[a] These investigations suggest z_0 equal to interatomic spacing; for silicon on diamond: 0.15 - 0.23 nm

A second avenue of comparison involves starting with empirically-derived constants from well-established molecular dynamics potentials, some of which use a Lennard-Jones interatomic potential to describe the longer-range interactions between atoms or molecules. These values (designated C and D, in Eq. 2.8) can be used to calculate W_{adh} and z_0 in the surface potential by integration (as explicitly described in Ref. (*17*)). The length-scale for the C-C Lennard-Jones interatomic potential used in the AIREBO molecular dynamics potential (*18*) is 0.340 nm. Using the method of Ref. (*17*), this corresponds to $z_{0,C\text{-}C,LJ} = 0.243$ nm for a carbon-carbon interface. The corresponding

parameter for silicon do not seem to be as firmly agreed upon with values ranging from 0.220 nm (*19*) to 0.380 nm (*20*). These correspond to a range of $z_{0,Si\text{-}Si,LJ}$ = [0.157–0.272] nm. The present values agree well with these ranges.

4-3-2: Comparing the work of adhesion with previously proposed values

To assess how correctness of the measured value of W_{adh}, there are once again two different bodies of literature that can be consulted: first, values used in continuum contact mechanics investigations; and second, by comparing against the very well established literature on solids with van der Waals bonding between them.

While few investigations have directly measured the work of adhesion between a silicon tip and a diamond surface, there have been many prior reports of work of adhesion of related contact pairs: a silicon tip on DLC or UNCD; a diamond tip on silicon; or any of those materials in a self-mated configuration. Relevant measured results are shown for experimental investigations in Table 4.3 and for simulated investigations in Table 4.4. Measured values range widely from 0.01 J/m^2 (a hydrogen-terminated, self-mated UNCD pair) to 0.83 J/m^2 (a self-mated silicon contact pair). While the present result (W_{adh} = 0.66 J/m^2) lies in that range, it is significantly larger than most reported values from similar materials. This is expected as most (but not all) of the AFM studies were performed in air, where contamination and water desorption can passivate the surface, and also because none of the studies took account of the surface roughness on the tip or the sample, which can cause up to an order of magnitude drop in adhesion (as discussed in Chapter 5).

Table 4.3: Values of W_{adh} that have been measured in previously published *experimental* investigations of relevant contact pairs.

Tip/Substrate Materials	Measured W_{adh} (J/m^2)	Comment	Ref.
silicon / ta-C	0.10 - 0.35	AFM, in air; well-characterized tip radius	*(21)*
silicon / DLC	0.08	AFM, in air; well-characterized tip radius	*(2)*
DLC / DLC	0.05		
diamond / silicon (111)	0.20 - 0.45 [a]	Interfacial force microscope	*(22)*
diamond / UNCD	0.06	AFM, in air	*(23)*
diamond / UNCD-H [b]	0.01	AFM, in air	
amorphous C / diamond (111)-H	0.10	AFM, UHV [c], R_{tip} = 45 nm	*(24)*
amorphous C / diamond (111)-H	0.03	AFM, UHV, R_{tip} = 150 nm	
amorphous C / diamond (111)-H	0.19	AFM, UHV, R_{tip} = 45 nm	
amorphous C / diamond (111)-H	0.05	AFM, UHV, R_{tip} = 150 nm	
tungsten carbide / silicon	0.12	AFM, in air	*(25)*
tungsten carbide / diamond (111)	0.06	AFM, in air	
tungsten carbide / diamond (111)-H	0.04	AFM, in air	
tungsten carbide / UNCD	0.06	AFM, in air	
tungsten carbide / UNCD-H	0.03	AFM, in air	
silicon / silicon	0.83	AFM, in air	

[a] Radius not well characterized; quoted as "<10 nm". Also value decreased with time elapsed.

[b] An appended "-H" indicates that the surface was intentionally hydrogen-terminated

[c] "UHV" designates an environment of ultra-high vacuum

Table 4.4: Values of W_{adh} that have been measured in previously published *simulation* investigations of relevant contact pairs.

Tip/Substrate Materials	Measured W_{adh} (J/m^2)	Comment	Ref.
diamond (111) flat [a] / diamond (111)	0.20 - 0.30	Depends on H coverage	*(24)*
high-sp3 carbon flat / diamond (111)	0.15 - 0.23		
low-sp3 carbon flat / diamond (111)	0.15 - 0.25		
MDN [b] flat / diamond (111)	0.03 - 0.15	Depends on roughness	
diamond (001) flat / diamond (001)	0.15 - 0.25	Depends on H coverage	
low-sp3 carbon flat / diamond (001)	~0.10 [c]		
UNCD tip [d] / diamond (111)	~0.60	Simulated AFM-like tests	*(26)*
UNCD tip / diamond (111)-H	~0.35		
UNCD tip / UNCD	~0.40		
UNCD tip / UNCD-H	~0.20		
UNCD tip / DLC-H	~0.10		
UNCD-H tip / diamond (111)	~0.24		
UNCD-H tip / diamond (111)-H	~0.28		
UNCD-H tip / UNCD	~0.26		
UNCD-H tip / UNCD-H	~0.18		
UNCD-H tip / DLC-H	~0.10		
DLC-H tip / diamond (111)	~0.12		
DLC-H tip / diamond (111)-H	~0.12		
DLC-H tip / UNCD	~0.12		
DLC-H tip / UNCD-H	~0.10		
DLC-H tip / DLC-H	~0.08		

[a] Unlike AFM, contact involved two flat surfaces. W_{adh} calculated by integrating the force during separation

[b] MDN stands for "model diamond nanocomposite"

[c] The symbol "~" designates that these values were read off of plots and are accurate within ±0.05

[d] Similar to AFM, contact involved a 2.5-nm tip on a flat surface. W_{adh} calculated using DMT model (Eq. 2.5)

To assess the measured value of W_{adh} with more precision, it is useful to compare against the very well-established literature (see, for example, Ref. (*27*)) on solids with van der Waals bonding between them. The van der Waals theory and the more rigorous Lifshitz theory assume atomic interaction mechanisms (dispersion, Debye, and Keasom interactions, specifically) and are derived based on the physics of those. In describing

van der Waals bonding, the Hamaker constant $A_{1:2}$ conveniently describes the strength of interaction between materials (designated 1 and 2) interacting across a vacuum and is a function of the density and polarizability of the interacting materials.

In his classic text on interaction forces, Israelachvili (*27*) provides the needed values and conversions to compare the present results to this literature. The values of $A_{C:C}$ and $A_{Si:Si}$ have been theoretically calculated and measured to be approximately 30×10^{-20} and 20×10^{-20} J, respectively. Using a combining rule $A_{1:2} = \sqrt{A_{1:1}A_{2:2}}$, the value for silicon and diamond interacting across a vacuum is $A_{C:Si} = 24.5\times10^{-20}$ J. Finally, the work of adhesion between two planar surfaces experiencing van der Waals attraction is given by:

$$W_{adh} = \frac{A_{1:2}}{12\pi D_0^2} \ , \tag{4.2}$$

where D_0 represents the separation distance at contact. It is tempting to insert the measured value for z_0 into this equation for D_0. However, it is not clear that this is the correct approach. Figure 4.5 demonstrates the fundamentally different meanings of D_0 using a van der Waals approach and z_0 using a Lennard-Jones approach. In the van der Waals approach, an artificial hard-wall cut-off must be imposed in order to prevent the interaction going to infinity, the adhesive stress gets monotonically larger until D_0 is reached. Unfortunately, the exact value of this cut-off is somewhat arbitrary; it may or may not have a relationship to a physical spatial distance in the contact. Israelachvili discusses choosing a value of D_0 with the sole purpose of calculating physically reasonable values for W_{adh} (assuming cleavage of a material with known bond energy and areal density of bonds on the surface). In other words, the value of D_0 and the shape of

the potential are fundamentally unrelated in the van der Waals picture. By contrast, in the Lennard-Jones potential, z_0 represents a parameter of the potential. In the general treatment of planes, no artificial cut-off distance is needed[11] because the repulsive part of the potential balances the attractive potential and keeps it from increasing without bound. Thus, there is no reason that D_0 and z_0 should have the same value.

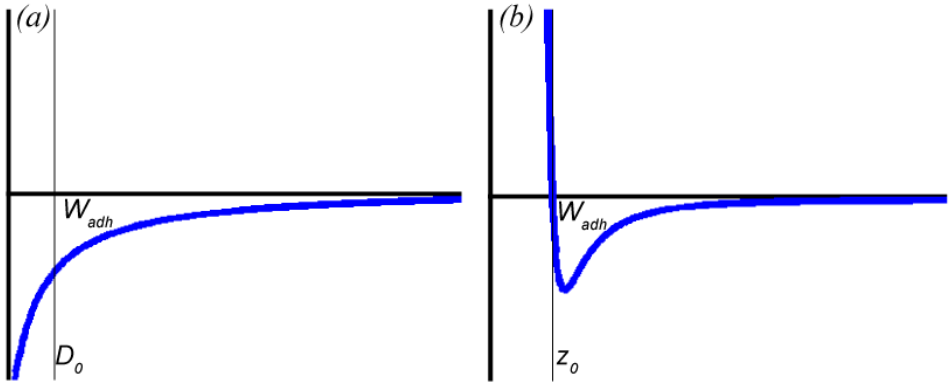

Figure 4.6: The van der Waals adhesion potential is compared with the Lennard-Jones potential to show the different meanings of D_0 and z_0. The van der Waals potential (a) is purely adhesive, therefore an arbitrary cut-off value must be chosen for D_0 such as the bounded region (labeled W_{adh}) agrees with measured values (*27*). In contrast, the Lennard-Jones potential has a repulsive part incorporated and so requires no such artificial cut-off for the interaction of two planar surfaces.

Given that z_0 cannot simply be inserted into Eq. 4.2, then what value should be used? According to Israelachvili, while "it is not at all obvious what value to use, […] for calculating surface energies we must use a 'cut off' distance D_0 that is substantially less than the interatomic or inter-molecular center-to-center distance" (page 277, 3rd Ed. of Ref. (*27*)). He goes on to suggest the use of the interatomic distance divided by 2.5 as

[11] Section 4-1-2 discusses the addition of a constraint of hard-wall repulsion at z_0 for certain shapes. This is required due to the simplifying assumptions of the integration method used in the present investigation. In the treatment of the adhesion of flat surfaces, no such hard-wall cut-off is required since the repulsive part of the potential balances the attractive part.

an empirical rule that applies to a wide variety of compounds. Given the interatomic distances discussed above, the values are calculated as $D_{0Si:Si}$ = 0.094 nm and $D_{0C:C}$ = 0.062 nm. If an average value is used in Eq. 4.2, along with the appropriate value of $A_{Si:C}$ (see above), the $W_{adh,vdW}$ is equal to 1.08 J/m^2. This is larger than the measured value, but it also likely represents an over-estimate for this material pair because the method for calculation of surface energies in Ref. (*27*) assumes perfect commensurate surfaces of a single crystal, rather than two different surfaces coming into contact.

4-3-3: Origins of the large amounts of scatter in the data

There was significant scatter in the data, with W_{adh} and z_0 each having approximately 20% uncertainty in the measured values. This is likely arising either due to real fluctuations in changes in the tip and/or sample surfaces with time, or due to approximations and limitations of the analysis routine – both of which are difficult to quantify. The first source could be due to slight fluctuations in contact location (due to drift in the system), which lead to differences in local topography or structure (passivation, relaxation, etc.) of the surfaces in contact. Additionally, there could be bond formation/breaking across the interface, which would lead to deviations in the pull-off force and could lead to local atomic topographical rearrangements (that may or may not be visible given the resolution of the TEM). The uncertainty could also arise due to the significant assumptions in the model. For instance, the assumption of local axinsymmetry (i.e. a circular cross-section at every height) is almost certainly not strictly correct and may be more or less accurate for different probe tips. Also, the high-

resolution images cannot resolve atomic structure. The tracing routine is a best guess of location of the tip apex and assumes that the surface is smooth in between traced points. Finally, vibration in the tool was characterized and explicitly included in the analysis, but this assumes that the vibration is constant with time and does not change significantly with tool use (e.g. motion of the piezoelectric stage) nor with external factors (e.g. foot traffic outside the room). To study and address these factors in more detail, a larger number of measurements is desired, ideally in a variety of conditions (different probes, different times of day, even different *in situ* indenters, if possible).

4-3-4: Impact of the present technique for adhesion characterization

Despite the large uncertainty in the measured values, they represent the characterization of the length-scale and the strength of adhesion between two technologically relevant materials. Knowledge of these parameters is required for predicting what the forces at work in nanoscale contacts and for designing strategies and geometries to maximize or minimize these forces in nanoscale devices or applications. While the present analysis assumes a Lennard-Jones type interaction – likely a gross simplification of the real adhesive interactions – Barthel (*28*) and others showed that calculated results are relatively insensitive to the exact form of the potential (Sect. 2-2-4). The length-scale and the strength of the adhesion are quite significant, but if these values are kept constant, the exact shape of underlying curve (square, triangle, Lennard-Jones, etc.) has a second-order effect. This implies that the values measured here may provide a

very accurate description of adhesion between these two materials, despite the simplifications made in the analysis.

4-4: Conclusions regarding the measurement of adhesion parameters

As discussed in Sect. 2-2-3, a limitation of adhesion integration methods is the lack of reliable data for work of adhesion W_{adh}, and particularly for the adhesive range z_0 for a given pair of surfaces. The advancement of the present method, containing direct visualization of the tip shape and its behavior during the adhesion test, is that the pull-off force and snap-in are used to provide two independent equations – each of which depends on both variables, W_{adh} and z_0. Therefore, both variables can be extracted through simultaneous fitting of the experimental data. The measured values do not exceed bounds of what is physically reasonable, and they agree approximately with most previously published estimates and with most values calculated based on related techniques. The values measured here, and the technique demonstrated, provide a basis for more accurate and predictive models of adhesion in real nanoscale devices and applications.

4-5: References

(1) Grierson, D.; Flater, E.; Carpick, R. Accounting for the JKR-DMT transition in adhesion and friction measurements with atomic force microscopy. *J. Adhes. Sci. Technol.* **2005**, *19*, 291–311.

(2) Grierson, D. S.; Liu, J.; Carpick, R. W.; Turner, K. T. Adhesion of nanoscale asperities with power-law profiles. *J. Mech. Phys. Sol.* **2013**, *61*, 597–610.

(3) Zheng, Z.; Yu, J. Using the Dugdale approximation to match a specific interaction in the adhesive contact of elastic objects. *J. Coll. Int. Sci.* **2007**, *310*, 27–34.

(4) Maugis, D. Adhesion of spheres: the JKR-DMT transition using a Dugdale model. *J. Coll. Int. Sci.* **1992**, *150*, 243–269.

(5) Greenwood, J. Adhesion of elastic spheres. *Proc. Roy. Soc. A* **1997**, *453*, 1277–1297.

(6) Adachi, S. *GaAs and Related Materials: Bulk semiconducting and superlattice properties*; World Scientific Publishing Company, 1994.

(7) Davidson, J. L. *Diamond Materials VI*; Davidson, J. L.; Brown, W. D.; Gicquel, A.; Spitsyn, B. V.; Angus, J. C., Eds. The Electrochemical Society: Pennington, NJ, 2000.

(8) Yao, H.; Ciavarella, M.; Gao, H. Adhesion maps of spheres corrected for strength limit. *J. Coll. Int. Sci.* **2007**, *315*, 786–790.

(9) Tabor, D. Surface forces and surface interactions. *J. Coll. Int. Sci.* **1977**, *58*, 2–13.

(10) Muller, V. M.; Yushchenko, V. S.; Derjaguin, B. V. On the influence of molecular forces on the deformation of an elastic sphere and its sticking to a rigid plane. *J. Coll. Int. Sci.* **1980**, *77*, 91–101.

(11) Derjaguin, BV; Muller, V.; Toporov, Y. P. Effect of contact deformations on the adhesion of particles. *J. Coll. Int. Sci.* **1975**, *53*, 314–326.

(12) Persson, B. Nanoadhesion. *Wear* **2003**, *254*, 832–834.

(13) Carpick, R. W.; Agrait, N.; Ogletree, D. F.; Salmeron, M. Measurement of interfacial shear (friction) with an ultrahigh vacuum atomic force microscope. *J. Vac. Sci. Tech. B* **1996**, *14*, 1289–1295.

(14) Enachescu, M.; van den Oetelaar, R.; Carpick, R. W.; Ogletree, D. F.; Flipse, C.; Salmeron, M. Atomic force microscopy study of an ideally hard contact: The diamond(111) tungsten carbide interface. *Phys. Rev. Lett.* **1998**, *81*, 1877–1880.

(15) Rabinovich, Y. Adhesion between nanoscale rough surfaces II. Measurement and comparison with theory. *J. Coll. Int. Sci.* **2000**, *232*, 17–24.

(16) Katainen, J.; Paajanen, M.; Ahtola, E.; Pore, V.; Lahtinen, J. Adhesion as an interplay between particle size and surface roughness. *J. Coll. Int. Sci.* **2006**, *304*, 524–529.

(17) Yu, N.; Polycarpou, A. A. Adhesive contact based on the Lennard–Jones potential: a correction to the value of the equilibrium distance as used in the potential. *J. Coll. Int. Sci.* **2004**, *278*, 428–435.

(18) Stuart, S.; Tutein, A.; Harrison, J. A. A reactive potential for hydrocarbons with intermolecular interactions. *J. Chem. Phys.* **2000**, *112*, 6472–6486.

(19) Zimmerman, P. M.; Head-Gordon, M.; Bell, A. T. Selection and Validation of Charge and Lennard-Jones Parameters for QM/MM Simulations of Hydrocarbon Interactions with Zeolites. *J. Chem. Theory Comput.* **2011**, *7*, 1695–1703.

(20) Lee, S. H.; Rossky, P. J. A comparison of the structure and dynamics of liquid water at hydrophobic and hydrophilic surfaces—a molecular dynamics simulation study. *J. Chem. Phys.* **1994**, *100*, 3334.

(21) Liu, J.; Notbohm, J. K.; Carpick, R. W.; Turner, K. T. Method for characterizing nanoscale wear of atomic force microscope tips. *ACS Nano.* **2010**, *4*, 3763–3772.

(22) Moore, N. W.; Houston, J. E. The Pull-Off Force and the Work of Adhesion: New Challenges at the Nanoscale. *J. Adhes. Sci. Technol.* **2010**, *24*, 2531–2544.

(23) Sumant, A.; Grierson, D.; Gerbi, J.; Carlisle, J.; Auciello, O.; Carpick, R. Surface chemistry and bonding configuration of ultrananocrystalline diamond surfaces and their effects on nanotribological properties. *Phys. Rev. B* **2007**, *76*.

(24) Piotrowski, P. L.; Cannara, R. J.; Gao, G.; Urban, J. J.; Carpick, R. W.; Harrison, J. A. Atomistic Factors Governing Adhesion between Diamond, Amorphous Carbon and Model Diamond Nanocomposite Surfaces. *J. Adhes. Sci. Technol.* **2010**, *24*, 2471–2498.
(25) Sumant, A. V.; Grierson, D. S.; Gerbi, J. E.; Birrell, J.; Lanke, U. D.; Auciello, O.; Carlisle, J. A.; Carpick, R. W. Toward the Ultimate Tribological Interface: Surface Chemistry and Nanotribology of Ultrananocrystalline Diamond. *Adv. Mater.* **2005**, *17*, 1039–1045.
(26) Harrison, J. A.; Keating, P. L.; Ryan, K. E. Unpublished data.
(27) Israelachvili, J. N. *Intermolecular and Surface Forces*; Academic Press, 2011.
(28) Barthel, E. On the description of the adhesive contact of spheres with arbitrary interaction potentials. *J. Coll. Int. Sci.* **1998**, *200*, 7–18.

CHAPTER 5: Nanoscale adhesion, Part II: The effect of atomic-scale roughness[12]

As discussed before, while it is well established that adhesion energies and forces, including forces of separation, depend strongly on the geometry of the contacting bodies, there is little understanding and almost no direct measurements of such phenomena at the nanometer scale. Even nanoengineered surfaces like molded or sculpted AFM tips can have random nano- and atomic-scale features, and these are difficult to model and even more difficult to measure. The previous chapter presented analysis applicable to cases where the tip's geometry is known with sub-nanometer-scale detail. A more generalizable question regards the effect of *tip roughness* on adhesion; i.e., characterizing the impact of measured roughness parameters, rather than characterizing individual tips. *In situ* microscopy provides an opportunity to address this question in ways that were previously impossible. This chapter presents adhesion tests performed inside the TEM, which enable concurrent characterization of the sub-nanometer tip roughness and the force required to pull the tip off of the surface. The *in situ* imaging capability is leveraged by comparing against atomistic simulations; this enables the identification of trends of adhesion over a wide range of roughness values.

[12] Much of this chapter appears in print: Adapted Turner with permission from Jacobs, T. D. B.; Ryan, K. E.; Keating, P. L.; Grierson, D. S.; Lefever, J. A.;, K. T.; Harrison, J. A.; Carpick, R. W. The Effect of Atomic-Scale Roughness on the Adhesion of Nanoscale Asperities: A Combined Simulation and Experimental Investigation. *Tribol. Lett.* **2013**, 50, 81–93. Copyright 2013 Springer.

5-1: Analytical results: A simple numerical model of roughness

As discussed in Sect. 2-1-1, there are no established models that predict the adhesive force between a rough, curved tip and a flat surface. While the method presented in Chapter 4 can be used for this purpose, it requires prior knowledge of the detailed contour of the tip. It is impractical to characterize the shape of each tip of interest, and further, Chapter 4 does not demonstrate trends of behavior such as those found in the significant body of literature regarding the effect on adhesion of roughness of planar surfaces (see Sect. 2-3). Therefore, before any *in situ* adhesion tests are presented, this section presents the expected trends of adhesion on tip roughness by using the adhesion integration method (described in Sect. 3-4-5) on model, axisymmetric tips of varying roughness.

Model tips were defined by superposing a paraboloid (for the overall tip shape) and a sine wave (representing the roughness) as follows:

$$z_{tip}(r) = z_{paraboloid}(r) + z_{roughness}(r) = \frac{r^2}{2R_{tip}} - A\cos\left(\frac{2\pi r}{\lambda}\right), \tag{5.1}$$

where r and z are cylindrical polar spatial coordinates, R_{tip} defines the radius of the overall parabolic shape, and A, λ are the amplitude and wavelength of the sine wave, respectively. The resulting tip (inset in Fig. 5.1) is treated as rigid and is paired with a rigid flat surface. The pull-off force was calculated (see Sect. 3-4-5) for varying inputs of A and λ. Values of $W_{adh,max}$ = 0.15 J/m^2, z_0 = 0.154 nm, and R_{tip} = 10 nm were chosen as physically reasonable values as input parameters for the Lennard-Jones surface potential (Eq. 2.9); the exact values are unimportant as the qualitative trends would be similar for other common experimental values. The roughness of the tip is changed by varying the

amplitude and the wavelength of $z_{roughness}$ over the range 0 - R_{tip}/10 (i.e., 0 - 1 nm for R_{tip} = 10 nm), and the RMS roughness of the tip is calculated from the profile of $z_{roughness}$. Once $F_{adhesive}$ is calculated for each value of RMS roughness, Eq. 2.5 is used to calculate the effective work of adhesion, $W_{adh,eff}$; since the tips are rigid, then $\mu_T \rightarrow 0$, so the DMT-limit (or, more accurately, the Bradley limit) applies. This quantity represents the work of adhesion that would be calculated if the roughness of the tip was ignored, i.e., if only the overall paraboloidal tip shape was considered. In fact, that is how the vast majority of experimental studies calculate the work of adhesion since, as stated earlier, the atomic-scale details of the tip are usually not measureable

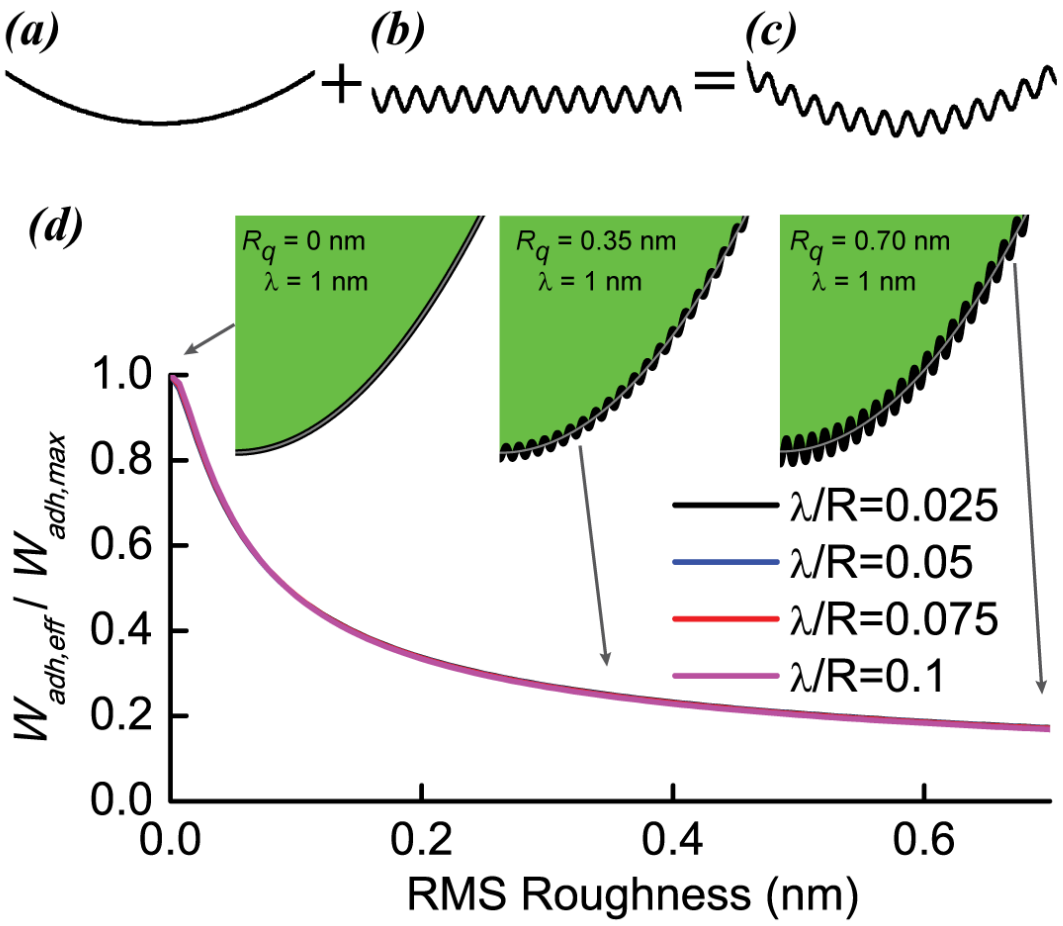

Figure 5.1: By applying a Lennard-Jones surface potential to a model tip composed of a sinusoid superimposed on a paraboloid, the essential trends of adhesion as a function of roughness are demonstrated. A smooth paraboloidal tip (a) has a sinusoidal roughness (b) superimposed on it to create a roughened tip (c). Using a similar approach to that described in Sect. 4-1-1, simulated pull-off force tests as a function of roughness yield values for $F_{adhesive}$. Then the DMT model (Eq. 2.5) is used to calculate an effective work of adhesion, $W_{adh,eff}$. This $W_{adh,eff}$ value has been divided by the input value $W_{adh,max}$ to determine the deviation due to RMS roughness R_q, as shown in (d) for various values of roughness wavelength. Results for all four values of λ overlap, with a maximum deviation of just 2% at any value of roughness. Insets in (d) indicate the roughness as compared to the overall shape (thin grey lines show the best-fit parabolic profiles) for three values of roughness. Note that for the tips and data shown in (d), R_{tip} = 10 nm and z_0 = 0.154 nm. Figure reproduced with permission from Ref. (*1*).

The results of this simplified rigid model are shown in Fig. 5.1(d). The effective work of adhesion is normalized by $W_{adh,max}$ (i.e., the input value for work of adhesion in

the interaction potential). This is shown as a function of the RMS roughness R_q, which, for any sine wave, is defined as $R_q = \frac{\sqrt{2}}{2} A$. While the model and its assumptions are quite simplistic, there are three key implications that provide insights for what to expect for real adhesion tests of hard materials:

1. The effective work of adhesion decreases significantly and rapidly with increasing roughness. Even with an RMS roughness of just 0.1 nm, the effective work of adhesion is reduced to almost 50% of its maximum value.
2. The results agree qualitatively with findings of the more sophisticated models discussed in Sect. 2-1-2. Larger roughness (i.e., larger R_q) increases the average separation between the two surfaces and thus decreases the adhesive stress acting between them. Because the results have been normalized to the maximum (smooth-tip) work of adhesion, these trends are expected to be material independent.
3. The results show almost no dependence on the wavelength of the roughness, when the wavelength is kept significantly smaller than the tip radius. Over the range shown in Fig. 1(d) ($0.025 \leq \lambda/R \leq 0.1$), there is only a 2% change in normalized work of adhesion due to changes in wavelength.

The quantitative reduction of $W_{adh,eff}$ with increasing roughness is sensitive to the chosen value of the equilibrium separation, z_0; however, the sharply decreasing trend of $W_{adh,eff}$ as a function of roughness will occur for any reasonable value chosen.

5-2: Measuring adhesion with direct, concurrent measurements of tip topography

5-2-1: Experimental in situ *TEM measurements*

Adhesion tests were performed inside the TEM to enable concurrent measurements of the sub-nanometer tip roughness and the force required to pull the tip off of the surface. Using the methods described in Sect. 3-2, adhesion tests were performed for multiple DLC and UNCD tips making contact with a single-crystal diamond substrate using the TEM-based PicoIndentor. An example video of a typical adhesion test can be found in the Supplemental Information of associated with Ref. (*1*). At least 9 adhesion tests were performed on each probe; histograms are provided in Fig. 5.2(*i-vi*). The average of the measured values was reported as $F_{adhesive}$, with the standard deviation of the measurements reported as the uncertainty in that value. There is significant scatter in the data, consistent with results from prior investigations (such as Ref. (*2*)). This scatter is thought to be attributable to vibration or drift in the instrument. Vibration and ambient mechanical noise could result in slightly premature pull-offs; drift could result in small changes in contact location – with resulting changes in local topography and roughness. Even small changes in registry/distregistry of atomic corrugation between opposing surfaces have been shown to have a significant effect on pull-off force (*3*). The roughness of the tip was characterized before testing, as described in Sect. 3-3-1, as is shown for each tip in Fig. 5.3. High-resolution images taken after the adhesion testing confirmed that the tip shape and roughness did not change during testing.

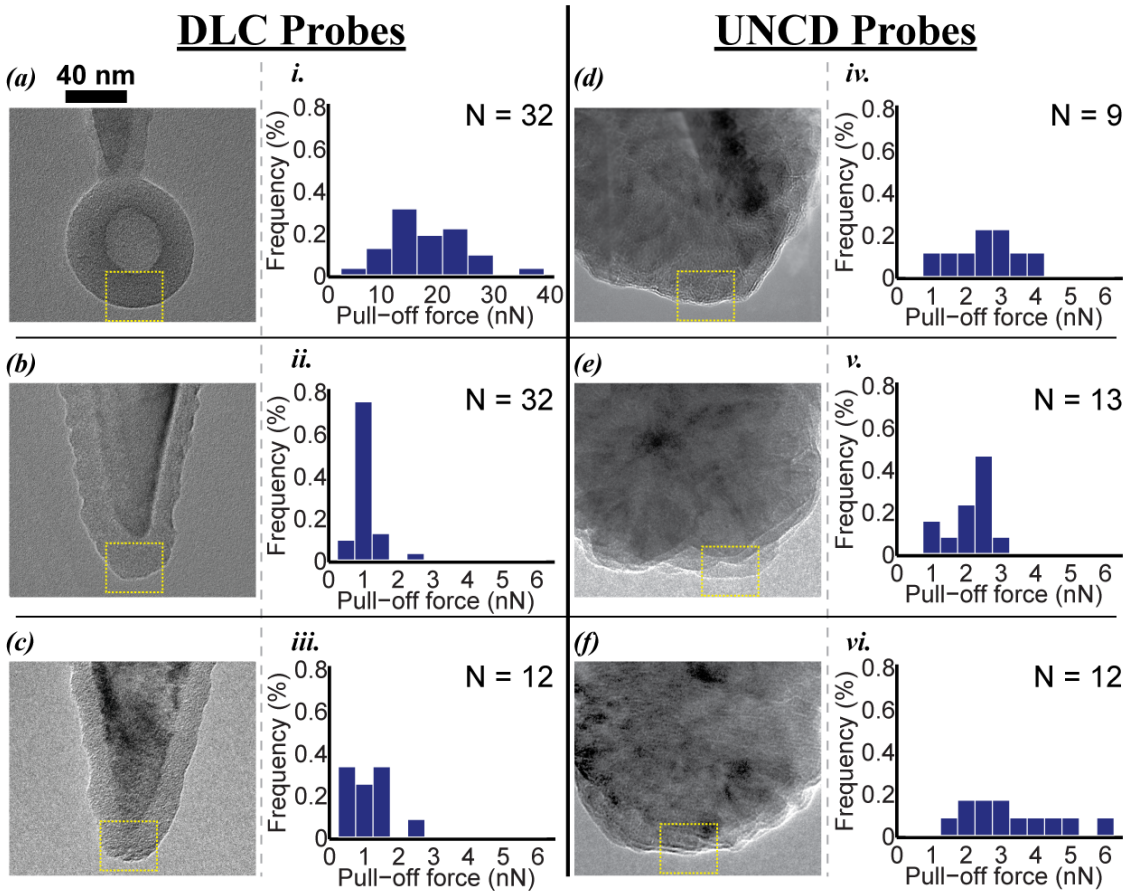

Figure 5.2: In situ adhesion tests were used to measure adhesive forces on asperities of diamond-like carbon and ultrananocrystalline diamond against a single crystal diamond substrate. Three DLC-coated silicon asperities (a-c) and three UNCD-coated silicon asperities (d-f) were used in this study. For the probe shown in (a), an irregularity in the coating process produced an almost perfect hollow sphere on the end of the probe. Each probe was used for at least 9 pull-off tests; histograms of the measured adhesion force $F_{adhesive}$ are shown in (*i-vi*). The dashed boxes indicate the regions of the tips that were imaged at higher resolution; the corresponding images are shown in Fig. 5.3. Figure reproduced with permission from Ref. (*1*).

Combining the measured adhesion force $F_{adhesive}$ and the best-fit parabolic radius R_{tip}, the effective work of adhesion $W_{adh,eff}$ was calculated using Eq. 2.5, the standard technique for AFM-based measurements of work of adhesion. All measured and calculated values are shown in Table 5.1 along with the tip radii and roughness values.

For the DLC tips, there is an 80% reduction in measured work of adhesion between the smoother tip (R_q roughly 0.2 nm) and the rougher tips (R_q roughly 0.5 nm). Likewise, the UNCD tips show a 50% reduction over the interval of 0.5 – 1.6 nm of RMS roughness. These results clearly demonstrate a steep downward trend of effective work of adhesion with increasing roughness on the sub-nanometer to nanometer length scale. More generally, these results demonstrate that the standard experimental technique for measuring work of adhesion produces results that depend very sensitively on tip roughness, a parameter that is not measured in a typical test. This investigation further shows that the work of adhesion, a parameter that is typically treated as a constant for a given tip/sample material pair (*4*), is highly geometry-dependent.

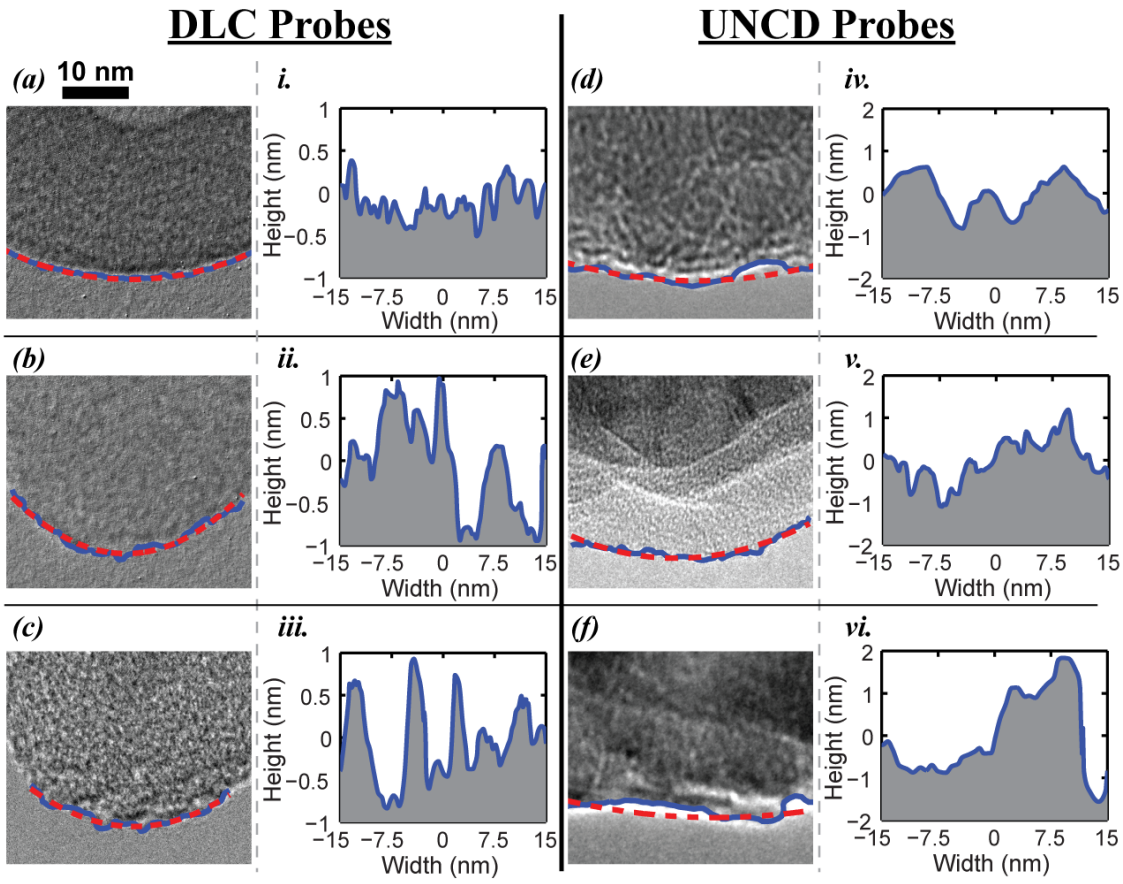

Figure 5.3: The roughness of each tested tip has been characterized with sub-nanometer resolution. The outer profiles of two-dimensional side views are traced (blue) and fit to a parabola (red). The subtraction of the two curves yields the equivalent roughness that would be measured on a flat surface; these profiles are shown in (*i-vi*). For ease of direct visual comparison, the axes of (*i-vi*) have been standardized among the various tips of a single material; in some cases, the profile that was measured and analyzed extends beyond the representative region shown. Figure reproduced with permission from Ref. (*1*).

Table 5.1: All data from the experimental and simulated adhesion tests. For each tip/sample combination, the tip radius is extracted using a parabolic fit to the measured profile and the pull-off force is measured directly. From these values, the effective work of adhesion is calculated using Eq. 2.5. The RMS roughness is extracted as described in Sect. 3-3-1.

Tip material	Sample	Method	Tip radius (nm)	Adhesion Force (nN)	RMS Roughness (nm)	Eff. Work of Adhesion (J/m^2)
DLC Probes						
DLC (Fig. 2a)	Diamond(111)-H	MD	2.33	2.02 ± 0.10	0.033	0.138 ± 0.007
DLC (Fig. 2b)	Diamond(111)-H	MD	2.67	1.08 ± 0.24	0.098	0.064 ± 0.014
DLC (Fig 5a)	Diamond punch	TEM	45.72	17.1 ± 6.9	0.182	0.060 ± 0.024
DLC (Fig 5b)	Diamond punch	TEM	21.55	1.0 ± 0.4	0.456	0.007 ± 0.003
DLC (Fig 5c)	Diamond punch	TEM	17.40	1.1 ± 0.4	0.548	0.010 ± 0.004
UNCD Probes						
UNCD (Fig. 2c)	Diamond(111)-H	MD	2.74	4.56 ± 0.33	0.031	0.265 ± 0.019
UNCD (Fig. 2d)	Diamond(111)-H	MD	2.56	2.02 ± 0.08	0.121	0.125 ± 0.005
UNCD (Fig 5d)	Diamond punch	TEM	37.83	2.1 ± 0.6	0.514	0.009 ± 0.003
UNCD (Fig 5e)	Diamond punch	TEM	70.23	2.6 ± 0.9	0.644	0.006 ± 0.002
UNCD (Fig 5f)	Diamond punch	TEM	115.51	3.2 ± 1.4	1.576	0.004 ± 0.002

It should be noted that RMS roughness is ideally measured over a constant sampling area. Unfortunately due to deviations in tip size (between different coated TEM probes, and especially between simulated tips in the subsequent section), different sampling widths were unavoidable in this study. While this will add some additional degree of uncertainty to the results, the increasing roughness of the tips demonstrated by changes in the RMS roughness reported in Tables 5.1 can clearly be verified by visual inspection of the profiles shown in Figs. 5.3(i-iv) and 5.6(i-vi).

5-2-2: Complementary simulated adhesion tests performed by collaborators

Since the roughness of the coated tips cannot be controlled nor systematically varied, complementary simulated adhesion tests were performed by collaborators at the US Naval Academy. Test conditions (materials, geometry, environment) were as closely-matched as possible to those of the experiments. The specific details of the creation of the

simulation tips can be found elsewhere (*5*). In short, axisymmetric paraboloidal tips were cut from bulk DLC or UNCD according to the equation:

$$z(r) = \frac{r^2}{2R_{tip}}, \tag{5.2}$$

where R_{tip} (the radius of curvature) was set at 2.5 nm and the height of the tip along the *z*-axis was set at 3.5 nm. The radius of curvature of the tips was selected to be as large as was computationally feasible. After equilibration in hydrogen to passivate dangling bonds, the tips (shown in Fig. 5.4(a,c)) were brought into contact with the hydrogen-terminated (111) face of diamond (shown in Fig. 5.4(a)). Additional tips were made and tested with intentionally roughened surfaces, as shown in Fig 5.4(b,d). These were created by taking the equilibrated tips described above, randomly removing 25% of the carbon atoms from the outer 3-5 Å of the tip, and re-equilibrating in hydrogen. All adhesion simulations were performed using the adaptive intermolecular reactive empirical bond-order potential (AIREBO) (*6*). While this potential is based on the 2nd generation REBO (*7*), it additionally captures intermolecular interactions by allowing for longer-range (so called "non-bonded") interactions using a Lennard-Jones term (Eq. 2.8) and also by including a term to account for torsional energies of bond rotation. It was developed for hydrocarbons and is well-suited for capturing interactions between surfaces of carbon-hydrogen systems. The potential was coded into the Large-scale Atomic/Molecular Massively Parallel Simulator (LAMMPS) (*8*).

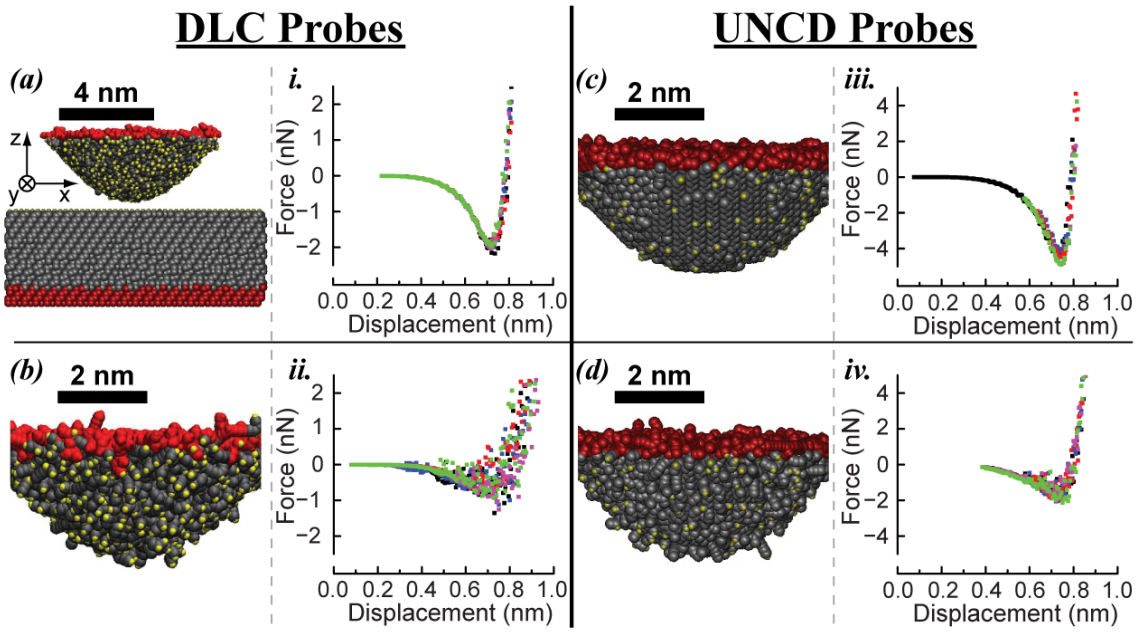

Figure 5.4: Simulated adhesion tests were performed by collaborators using molecular dynamics, conditions were matched as closely as possible to the TEM adhesion tests. Simulation tips made from DLC and UNCD (a, c, respectively) are shown with carbon atoms colored grey and hydrogen atoms colored yellow; red atoms represent those that are held rigid during testing. Replicas of these tips were roughened intentionally (b, d). Adhesion tests were performed against a hydrogen-terminated diamond substrate (included in (a)) to calculate the interaction force as a function of *z*-displacement, as shown in (*i-iv*). Data points from five tests performed with slightly different impact locations are shown overlapped (each with a different color, online) to indicate the degree of scatter in repeated tests. For both materials, the rougher tips demonstrate reduced pull-off forces and larger variability in force curves. Figure reproduced with permission from Ref. (*1*).

The pull-off force was identified as the minimum value of force as a function of displacement, as shown in Fig. 5.4(*i-iv*). To account for crystalline alignment effects, multiple contact points were chosen by shifting the tip by one half or one full length of the unit cell of diamond in each lateral direction in a manner similar to (*3*). The tip radius and roughness of the equilibrated tips was measured as described in Sect. 3-3-1, as shown in Fig. 5.5.

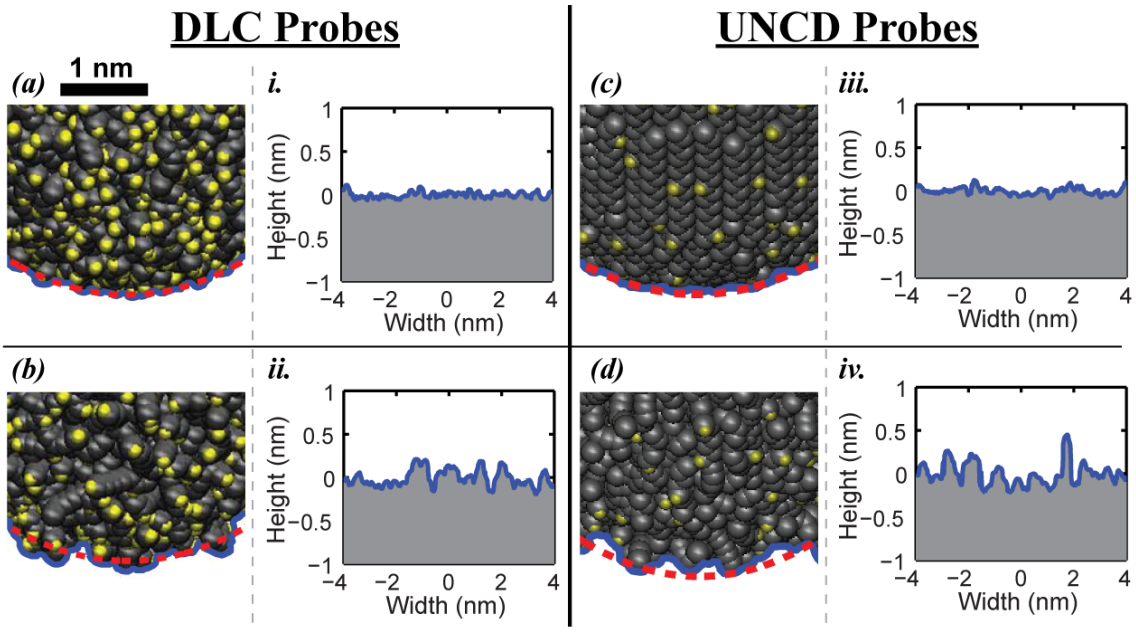

Figure 5.5: The roughness of the simulated tips was characterized using the same approach as was used on the experimental tips. Using The roughness of the MD probes is characterized using side-view renderings of all probes (a-d) using VMD software (*9*) and the van der Waals radius of each atom. The outer profiles are traced (blue) and fit to a parabola (red). While the entire profile of the tip was traced and analyzed (approximately 8 nm in arc length), these images of the tip traces have been expanded to show detail. The subtraction of the two curves (measured and fit) yields the equivalent roughness (shown in *i-iv*) that would be measured on a flat surface. The original parabolic tips of DLC (a) and UNCD (c) are significantly smoother than the intentionally roughened versions of the same tips (b, d, respectively). Figure reproduced with permission from Ref. (*1*).

Finally, the effective work of adhesion was calculated using Eq. 2.5. All measured and calculated parameters for the simulated tips are shown in Table 5.1. Only data for the approach portion of the curve was analyzed, but in all cases, the approach and retract portions were symmetrical and post-test examination showed no chemical bond formation. The trends seen in the experimental data were reproduced in the simulated data, with precipitous drops in effective work of adhesion with increasing roughness.

Results from both the experimental and simulated data sets are plotted together in Fig. 5.6. It is clear that the simulated data form a consistent trend with the experimental data. This is particularly clear for the DLC tips where the roughest simulated tip approaches the roughness value of the smoothest experimental tip. Taken together, the two data sets show that for both DLC and UNCD, there is more than an order of magnitude drop in effective work of adhesion as roughness increased from 0.03 nm (atomically smooth) to approximately 0.5 nm. The magnitude of this decrease in $W_{adh,eff}$ due to Ångström-level and nanoscale roughness highlights the degree to which measured values of work of adhesion depend on roughness, even when the roughness is at the atomic scale.

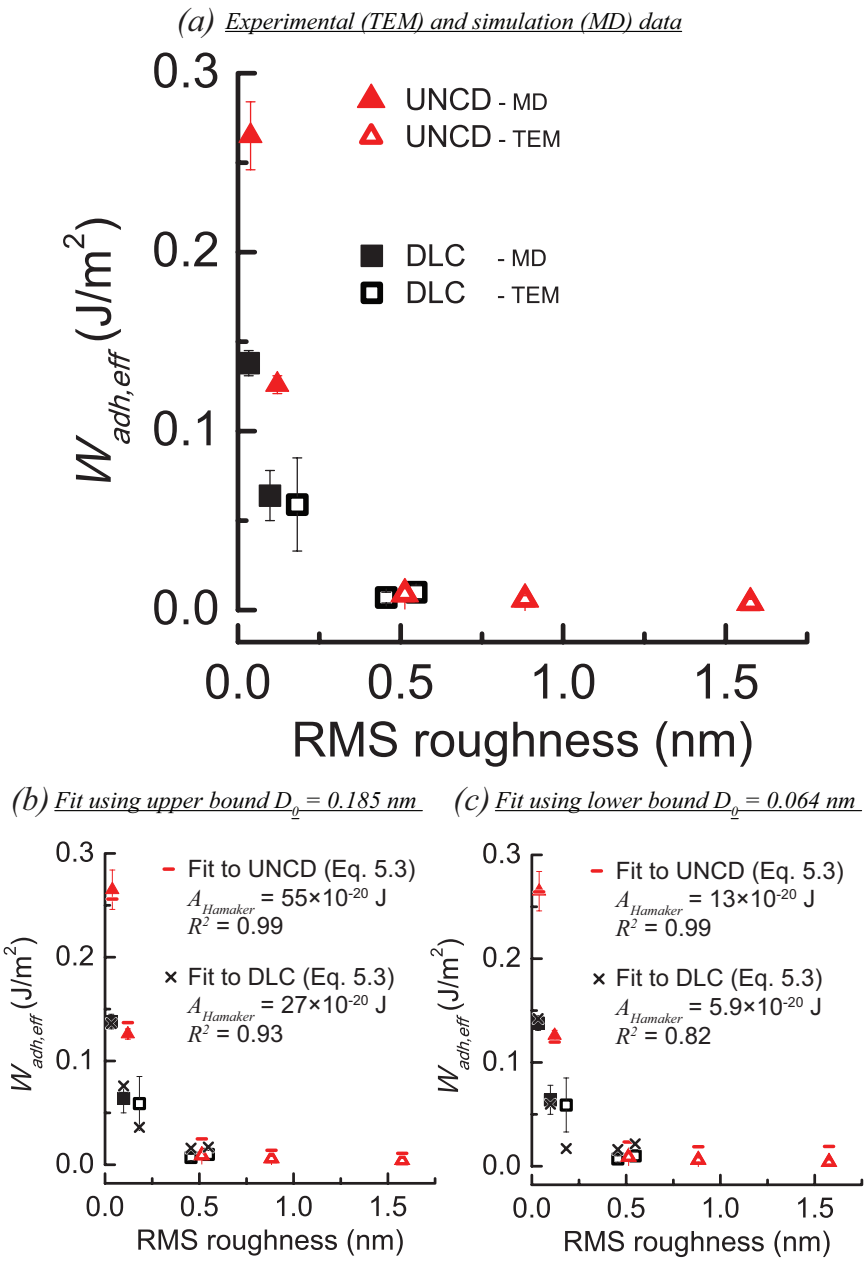

Figure 5.6: The experimental and simulated tests show a consistent trend of adhesion with roughness; this trend is well-fit using a previously proposed roughness model. The work of adhesion decreases by more than an order of magnitude as roughness increases from the sub-Ångström level (atomic corrugation only) to the nanometer scale. Results from MD simulations (filled data points) and from experimental testing (hollow data points) are shown (a) for sharp tips made of UNCD (red) and of DLC (black). The modified Rumpf model (Eq. 5.3) was fit separately to each material (indicated by '-'s and 'x's of corresponding color) using either the upper bound (b) or lower bound of D_0. Best-fit values of Hamaker constant for each material from fitting the model are given in the legend. Figure reproduced with permission from Ref. (*1*).

5-2-3: Fitting experimental and simulation results with a simple literature model

To put these results in context, they were compared to predictions from all models discussed in Sect. 2-1-1, even though these contacts explicitly violate assumptions made by many of these models (for example, the assumption that asperity radii $R_{asperity}$ are identical (*10-14*)). Note that the self-affine fractal model (*15*) was not tested because the two-dimensional measured profiles provided insufficient data to accurately calculate the power spectra of the surfaces. The most readily applicable models are those in which a sphere (radius R_{tip}) in contact with a rough surface is approximated as the same sphere in contact with a single small asperity (of radius $R_{model\text{-}roughness}$) situated on a perfectly smooth surface (as described in Sect. 2-3 and pictured in Fig. 2.1(c)) The adhesion force calculated using the simplest of these models (the modified Rumpf model, Eq. 2.10) can be combined with Eq. 2.5 to calculate the dependence of measured work of adhesion $W_{adh,eff}$ on roughness R_q as follows:

$$W_{adh,eff} = \frac{F_{adhesive}}{2\pi R_{tip}} = \frac{A_{Hamaker}}{12\pi D_0^2}\left[\left(1+\frac{R_{tip}}{1.48R_q}\right)^{-1}+\left(1+\frac{1.48R_q}{D_0}\right)^{-2}\right]. \quad (5.3)$$

(The DMT model (Eq. 2.5) is used rather than the JKR model (Eq. 2.6), based on calculated Maugis parameters (Sect. 2-2-2) in the range of 0.012 to 0.108 for the present tests.)

The present data has been fit using Eq. 5.3 with input parameters calculated as follows: the measured pull-off force $F_{adhesive}$; the asperity radii R_{tip} extracted from parabolic fits; and the RMS roughness R_q values extracted from the flattened profiles (as described in Sect. 3-3-1). Unfortunately, choosing a value for D_0 is not straightforward

(as discussed in Sect. 4-3-2). For fitting the present data, two limiting cases were chosen: the lower bound of D_0 = 0.062 nm corresponds to 40% of the interatomic spacing (*4*); the upper bound of D_0 = 0.185 nm corresponds to a physically reasonable value for separation of the surfaces in contact, calculated using the method described in Ref. (*16*) and using the value of the *interatomic* equilibrium spacing taken from the AIREBO potential used in the simulations. The data for the DLC and UNCD tips were fit separately, each with the Hamaker constant as the only free parameter. The fits to the data using the upper bound of D_0 were quite good, with adjusted R^2 values of 0.99 (UNCD) and 0.93 (DLC). The fits using the lower bound of D_0 were *also* good, with adjusted R^2 values of 0.99 (UNCD) and 0.82 (DLC). Values for the Hamaker constant were extracted from all fits: for D_0 = 0.185 nm, $A_{DLC:Diamond} = 27\times10^{-20}$ J and $A_{UNCD:Diamond} = 55\times10^{-20}$ J; for D_0 = 0.062 nm, $A_{DLC:Diamond} = 5.9\times10^{-20}$ J and $A_{UNCD:Diamond} = 13\times10^{-20}$ J. Since the appropriate choice of D_0 is uncertain, these can be considered upper and lower bounds for each material. (When this data was previously published (*1*), the only the value of 0.185 nm was used. In the present thesis, both values are used to demonstrate the ambiguity in this value and its effect on measured parameters.) While specific reference values for these material pairs do not exist, the order of magnitude of these values compares favorably against the reference value of $A_{Hamaker} = 30\times10^{-20}$ J calculated for diamond surfaces in a vacuum (*4*). The much-lower value of Hamaker constant for DLC as compared to UNCD is partially explained by the lower density of the former (2.0 g/cm^3, measured using x-ray reflectivity) as compared to the latter (3.5 g/cm^3 (*17*)), however, van der Waals interactions are also affected by the electronic properties of the materials in contact.

One factor that was not considered in the above analysis was the roughness of the (nominally flat) counter-surface. However, in all cases the counter-surfaces had a lower RMS roughness than the contacting asperities, as discussed in Sect. 3-2-3 for the experimental tips. In the simulated contacts, the only topographical variations in the hydrogen-terminated (111) face of diamond are due to the atomic corrugation. Thus these surfaces can be considered to be ideally smooth. Therefore, in all cases, the roughness of the substrate is predicted to have only a secondary effect on adhesion.

Regardless of the details of the chosen fitting parameters, Fig. 5.6 clearly demonstrates several characteristics of the data and the model fit, which can be compared to those of the simplified rigid model presented in Sect. 5-1:

1. There is a significant and rapid decrease in effective work of adhesion with increasing roughness. The TEM and MD results show that for an RMS roughness of just 0.15 nm, the effective work of adhesion is already reduced by approximately 50% from its smooth-tip value. This trend compares very favorably to the rigid model shown in Fig. 5.1(d), where the same ~50% decrease was observed for an RMS roughness of 0.1 nm.
2. The observed dependence not only agrees qualitatively with predictions of published models (Sect. 2-3), but also can be fit quantitatively using the modified Rumpf model.
3. Finally, it may seem surprising that the modified Rumpf model fits well, especially given that it depends only on RMS roughness and does not take into account the spatial extent of the roughness. However, this finding is in agreement with the trend of the simplified rigid model (Fig. 5.1), which showed almost no

dependence of $W_{adh,eff}$ on the wavelength λ. The absence of dependence on wavelength is, in part, due to the fact that the elastic deformation is very small in these contacts due to the high modulus and relatively low values of adhesion.

5-3: Suggestion of a roughness-independent adhesion parameter

The atomically smooth MD tips (RMS roughness of roughly 0.03 nm for both smooth DLC and UNCD tips) with nearly perfect parabolic profiles approach the limit of smoothness that can be physically realized. Therefore, the work of adhesion determined from Eq. 2.5 for the contact between these tips and the C(111)-H substrate was considered to correspond to a maximum work of adhesion that is realistically attainable, $W_{adh,max}$, for the given material pairs (0.138 J/m^2 for DLC on C(111)-H, and 0.265 J/m^2 for UNCD on C(111)-H). If true, then while all values of effective work of adhesion, $W_{adh,eff}$, will be roughness dependent, this maximum value, $W_{adh,max}$, should not be. Because the modified Rumpf model fits the data well, Eq. 5.3 can be used to suggest an equation for extracting the smooth-tip work of adhesion, $W_{adh,max}$, from measurements of the effective work of adhesion, $W_{adh,eff}$, if the tip radius and roughness are known. As mentioned, $W_{adh,max}$ is taken as the value that would be measured with a tip containing atomic corrugation (R_q = 0.03 nm). In other words, from Eq. 5.3, $W_{adh,max} = W_{adh,eff}$ (R_q = 0.03 nm) and $W_{adh,measured} = W_{adh,eff}$ ($R_q = R_{q,measured}$). These two quantities can be divided, resulting in the following equation:

$$W_{adh,max} = \left[\frac{F_{pull-off}}{2\pi R_{tip}}\right] \frac{\left(1+\frac{R_{tip}}{1.48(0.03nm)}\right)^{-1} + \left(1+\frac{1.48(0.03nm)}{D_0}\right)^{-2}}{\left(1+\frac{R_{tip}}{1.48R_{q,measured}}\right)^{-1} + \left(1+\frac{1.48R_{q,measured}}{D_0}\right)^{-2}} . \quad (5.4)$$

In principle, this is a general equation which allows for the calculation of the work of adhesion that would be measured using an atomically-smooth tip (i.e., $W_{adh,max}$). This value should be a fundamental property of the tip and sample materials and should be independent of probe roughness. For instance, in the present study $W_{adh,max}$ was measured as 0.138 J/m^2 and 0.265 J/m^2 (DLC and UNCD, respectively) using the atomically smooth simulated tip; in principle, these values could have been calculated from measurements taken with tips that have finite roughness.

To test this method of calculation, all the data from rough tips (i.e., all data from Tables 5.1, *excluding* the atomically smooth simulated tips) can be processed together. Following the traditional method of measurement of work of adhesion (which accounts for tip radius, but not roughness), all measurements are averaged yielding $W_{adh,eff}$ = 0.035±0.031 J/m^2 for DLC and 0.036±0.060 J/m^2 for UNCD. These values are significantly different from the smooth-tip values reported in the previous paragraph and have standard deviations that are larger or roughly equal to the measured value. By contrast, when Eq. 5.4 is used to calculate a $W_{adh,max}$ from each measurement (with D_0 = 0.185 nm), the resulting values can be averaged to yield $W_{adh,max}$ = 0.121±0.071 J/m^2 for DLC and 0.140±0.078 J/m^2 for UNCD. These values agree within 50% with the smooth-tip values, and the standard deviation has been reduced to approximately half of the measured value. The remaining uncertainty and error may be attributed to a relatively

small sample size, but the principle is demonstrated. Further work is required to verify the reliability of this approach and the limits of its applicability.

The good agreement between the experimental and simulation data with a simple analytical model holds promise for addressing the challenge of extracting meaningful work of adhesion values from AFM measurements. In general, it is impractical, if not impossible, to characterize the details of the sub-nanometer-scale roughness of a tip every time a pull-off test is performed. However, the present results indicate that a reasonable estimate can be made of the effect on work of adhesion with knowledge only of the radius and RMS roughness of the tip material. If a set of tips are fabricated using the same method, TEM characterization of the roughness of a small set could be used to obtain a representative value of RMS roughness R_q, which can then be used with Eq. 5.4 to extract improved estimates of the smooth-tip work of adhesion, with meaningful uncertainty bounds.

5-4: Conclusions

Both the simple numerical model and the measured adhesion results demonstrate the extreme effect that atomic-scale roughness of nanoscale tips has on the measured value of work of adhesion. This work represents the first time that sub-nanometer-scale roughness of asperities has been measured and related to measured changes in adhesion. Adhesion forces are extremely sensitive to atomic-scale roughness in this range. If the atomic-scale roughness is not measured and explicitly accounted for (something that is difficult with nanoscale tips), then the true work of adhesion can be greatly

underestimated, and a wide range of values can be obtained for the same material pair. However, the simple modified Rumpf model is shown to fit the measured data remarkably well, and is thus used to suggest a roughness-independent measurement of adhesion.

Significant scientific questions remain open for future study. Most critically, the present analysis distills the surface topography to a single parameter and does not account for the multi-scale nature of surface roughness. Further experimental investigation is required to relate the present results to well-established models of nominally flat self-affine surfaces. An additional practical challenge lies in the difficulty of measuring tip roughness on typical AFM probes. Thus, even though this parameter has been shown to be critically important for interpreting AFM results, it remains unattainable to most AFM users since a TEM is required to obtain the needed information (and even with TEM, only a two-dimensional tip profile is obtained; the full three-dimensional topography remains unknown). This challenge could be addressed in the short term by the generation of statistics on the surface roughness of typical AFM probes processed using standard fabrication techniques, such that a typical range of R_q values can be quoted, allowing the calculation of a range of $W_{adh,max}$ values within which one can be confident the correct value lies. In the longer term, techniques would ideally be developed for assessing tip roughness – for instance, either using standardized surfaces and reconstruction algorithms (akin to current techniques for measuring tip radii) or else using pull-off tests from extremely robust and well-characterized surfaces (such as clean, atomically flat surfaces in ultra-high vacuum).

5-5: References

(1) Jacobs, T. D. B.; Ryan, K. E.; Keating, P. L.; Grierson, D. S.; Lefever, J. A.; Turner, K. T.; Harrison, J. A.; Carpick, R. W. The Effect of Atomic-Scale Roughness on the Adhesion of Nanoscale Asperities: A Combined Simulation and Experimental Investigation. *Tribol. Lett.* **2013**, *50*, 81–93.

(2) Liu, D. L.; Martin, J.; Burnham, N. A. Which fractal parameter contributes most to adhesion? *J. Adhes. Sci. Technol.* **2010**, *24*, 2383–2396.

(3) Piotrowski, P. L.; Cannara, R. J.; Gao, G.; Urban, J. J.; Carpick, R. W.; Harrison, J. A. Atomistic Factors Governing Adhesion between Diamond, Amorphous Carbon and Model Diamond Nanocomposite Surfaces. *J. Adhes. Sci. Technol.* **2010**, *24*, 2471–2498.

(4) Israelachvili, J. N. *Intermolecular and Surface Forces*; Academic Press, 2011.

(5) Jacobs, T. D. B.; Gotsmann, B.; Lantz, M. A.; Carpick, R. W. On the application of transition state theory to atomic-scale wear. In; 2010; Vol. 39, pp. 257–271.

(6) Stuart, S.; Tutein, A.; Harrison, J. A. A reactive potential for hydrocarbons with intermolecular interactions. *J. Chem. Phys.* **2000**, *112*, 6472–6486.

(7) Brenner, D. W.; Shenderova, O. A.; Harrison, J. A.; Stuart, S. J.; Ni, B.; Sinnott, S. B. A second-generation reactive empirical bond order (REBO) potential energy expression for hydrocarbons. *J. Phys.: Condens. Matter* **2002**, *14*, 783–802.

(8) *LAMMPS Molecular Dynamics Simulator*.

(9) Humphrey, W.; Dalke, A.; Schulten, K. VMD: visual molecular dynamics. *Journal of molecular graphics* **1996**, *14*, 33–38.

(10) Fuller, K.; Tabor, D. Effect of surface-roughness on adhesion of elastic solids. *Proc. Roy. Soc. A* **1975**, *345*, 327–342.

(11) Maugis, D. On the contact and adhesion of rough surfaces. *J. Adhes. Sci. Technol.* **1996**, *10*, 161–175.

(12) Rumpf, H. *Particle Technology*; Chapman and Hall: London, UK, 1990.

(13) Rabinovich, Y. Adhesion between nanoscale rough surfaces I. Role of asperity geometry. *J. Coll. Int. Sci.* **2000**, *232*, 10–16.

(14) Katainen, J.; Paajanen, M.; Ahtola, E.; Pore, V.; Lahtinen, J. Adhesion as an interplay between particle size and surface roughness. *J. Coll. Int. Sci.* **2006**, *304*, 524–529.

(15) Peressadko, A.; Hosoda, N.; Persson, B. Influence of Surface Roughness on Adhesion between Elastic Bodies. *Phys. Rev. Lett.* **2005**, *95*, 124301.

(16) Yu, N.; Polycarpou, A. A. Adhesive contact based on the Lennard–Jones potential: a correction to the value of the equilibrium distance as used in the potential. *J. Coll. Int. Sci.* **2004**, *278*, 428–435.

(17) Adiga, V.; Sumant, A.; Suresh, S.; Gudeman, C.; Auciello, O.; Carlisle, J.; Carpick, R. Mechanical stiffness and dissipation in ultrananocrystalline diamond microresonators. *Phys. Rev. B* **2009**, *79*, 245403.

CHAPTER 6: Nanoscale Wear, Part I: The Application of Reaction Rate Theory to Nanoscale Wear[13]

This chapter discusses the application of reaction rate theory to nanoscale wear. As discussed below, previous authors have analyzed wear data assuming an exponential dependence on stress; however, this approach has not been rigorously justified and analysis approaches have varied from author to author. To remedy this, in the present chapter, a specific thermally activated mechanism of wear is proposed, along with a description of the system in its initial, activated, and final states and the required assumptions. Then specific methods are discussed to extract the relevant activation parameters, along with the challenges of interpretation of those parameters. Finally, future investigation approaches are suggested for further exploring the fundamentals of nanoscale wear – some of which are employed in the subsequent chapter. The present chapter begins with a review of reaction rate theory and its assumptions, along with a case study of its application to dislocation glide. This serves to demonstrate themes that will be referred to later in the chapter.

6-1: Review of reaction rate theory

Reaction rate theory (also called *absolute rate theory* or *transition state theory*) originated as a framework for describing the kinetics of thermally activated chemical

[13] Much of this chapter appears in print: Adapted with permission from Jacobs, T. D. B.; Gotsmann, B.; Lantz, M. A.; Carpick, R.W. On the application of transition state theory to atomic-scale wear *Tribol. Lett.* **2010,** 39, 257-271. Copyright 2010 Springer.

reactions. The topics are very well covered elsewhere, for example by J. W. Christian (*1*) and by P. Hanggi *et al.* (*2*); therefore only the essential points are covered here. The classic formulation of reaction rate theory describes a set of reactants that undergo a process which moves them from one stable equilibrium point (the initial state) to another (the final state). The degree of progress is measured as the *reaction coordinate*. Stable equilibrium demands that the two terminal points lie at local energy minima and therefore at least one local maximum must exist at an intermediate position along the reaction coordinate. In the simplest picture, shown in Fig. 6.1, there is one maximum and the state of the system at this point is called the *activated complex*. The energy difference between the initial and activated states is known as the *activation energy*, (ΔG_{act}). For a large number of identical systems, Eyring used statistical mechanics to describe the overall rate of forward reaction k for a thermally activated process (*1*):

$$k = f_{att} \exp\left(-\frac{\Delta G_{act}}{k_B T} \right), \tag{6.1}$$

where f_{att} is an effective attempt frequency, ΔG_{act} is the Gibbs free energy of activation, k_B the Boltzmann constant and T the absolute temperature.

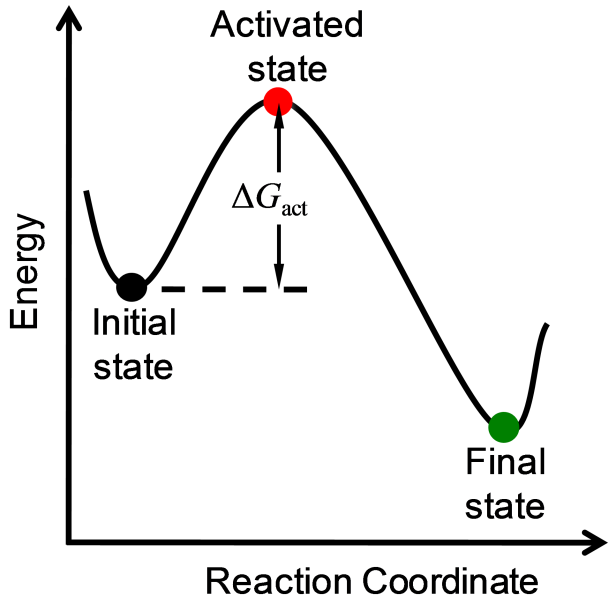

Figure 6.1: Reaction rate theory describes the kinetics of thermally activated processes. This schematic diagram shows the energy as a function of reaction coordinate for a system as it undergoes a thermally activated process. Figure reproduced with permission from Ref. (*3*).

As J. W. Christian (*1*) explains in his thorough text on the subject, there are five assumptions inherent in Eyring's analysis:

1) there is a continuous change along the reaction coordinate linking the stable initial and final states and the intermediate, unstable activated state;

2) the reaction will proceed along the lowest-energy path, thus the activated state will lie at a saddle point in energy;

3) once the system has reached the activated state, there is a high probability that it will proceed to the final state;

4) the initial state and activated state are at thermal equilibrium, such that Boltzmann statistics can be applied; and

5) the activated state possesses all degrees of freedom *except* vibrational motion along the reaction coordinate (which causes decomposition to the initial or final states).

The last assumption indicates that even the activated state is a point of stable equilibrium with respect to all other variables – it is only in the reaction coordinate that there is an energy maximum.

While this rigorous theoretical basis applies well to chemical reactions, its extension to reactions in solids (such as the movement of defects) is more complex as a crystal of N atoms contains $3N$ degrees of freedom and therefore the potential energy landscape is a $3N$-dimensional hypervolume. Vineyard was able to formulate the general, many-body problem and solve it rigorously in the context of reaction rate theory by approximating all vibrations as harmonic (*4*). His treatment described chemical diffusion by atomic hops, building on the work of other authors (*5*) to explain the temperature dependence of diffusion coefficients. In the absence of an external force, there is no work done on or by the system; therefore Vineyard used the Helmholtz free energy of activation $\Delta F_{act} = \Delta U_{act} - T\Delta S_{act}$, where ΔU_{act} and ΔS_{act} are the differences in potential energy and entropy, respectively, between the initial and activated states (the *activation energy* and *activation entropy*). By describing the potential energy landscapes around the initial and activated states as those of simple harmonic oscillators, the following Arrhenius-type rate equation can be derived (*4*):

$$k = f_{att} \exp\left(-\frac{\Delta F_{act}}{k_B T}\right) = \left\{\frac{\prod_{j=1}^{3N} f_j}{\prod_{j=1}^{3N} f_j'}\right\}\left(-\frac{\Delta U_{act}}{k_B T}\right) \qquad (6.2)$$

,

where f is an effective vibration frequency, and f_j and f_j' are the normal frequencies of oscillation about the initial state and the activated state, respectively, in the j^{th} degree of freedom. In accordance with assumption (5) of the Eyring treatment, the system has the full $3N$ degrees of freedom at its initial state, but only $3N$-1 at the activated state since, in that state, any vibration along the reaction coordinate causes decomposition to one of the terminal states. In many cases, the effective frequency factor is assumed to be in the range of 10^{12}-10^{13} Hz based on either of two assumptions: the vibrational modes of the initial and activated state can be assumed very similar such that the pre-factor shown in curly braces in Eq. 6.2 simplifies to the vibration frequency at the well bottom (Eq. 3.5 of Ref. (*2*)); alternatively, with appropriate substitution for the partition functions of the activated and initial states and under the assumption of negligible reactive volume, it can be shown that the other pre-factor takes the form $f_{att} = k_B T/h_P$ (where h_P is Planck's constant), which is equal to $f_{att} = 6.2\times10^{12}$ Hz at room temperature (Eq. 3.19 of Ref. (*2*)).

6-1-1: Case study on reaction rate theory: Plastic flow by dislocation glide

In the 1950s and '60s, substantial research was dedicated to plastic flow in crystalline metals in which deformation occurs by the motion of line defects (*dislocations*), which facilitates the relative motion of adjacent planes of atoms. Experimentally, many studies (such as Refs. (*6*, *7*)) demonstrated a logarithmic dependence of both strain rate (the time rate of change of the strain of the crystal) and dislocation velocity on the applied shear stress and on the inverse temperature. This behavior was explained using the formalism of transition state theory.

Articles by Gibbs (*8*), Hirth and Nix (*9*) and others describe a detailed model whereby the macroscopic behavior was characterized as the aggregate of a very large number dislocations, each of which has its motion pinned at various points by obstacles (such as crystal defects). In the initial state, the local dislocation segments are in mechanical equilibrium due to the opposing forces of the external applied stress and the local resistance to motion, which is increased by the obstacle, as shown in Fig. 6-2(a). The mechanical energy provided by the applied stress is insufficient to overcome the energy barriers represented by the pinning points. Therefore, the system must rely on thermal fluctuations to allow the dislocation segments to reach the unstable activated state (Fig. 6.2(b)), where the forces *just* balance and any perturbation causes decomposition either back into the initial state or forward into the final state. In the final state (Fig. 6.2(c)), the dislocation has reached a new stable equilibrium state due to some other obstacle. All activation parameters describe the transition between the initial and activated states.

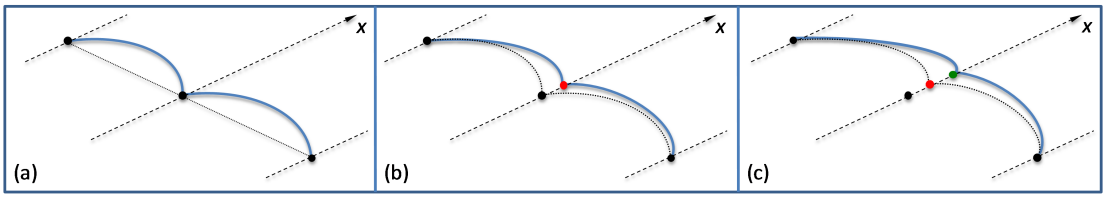

Figure 6.2: Reaction rate theory was successfully applied to plasticity and the movement of dislocations under stress; this earlier case study provides insights into the present application to nanoscale wear. In this schematic model, a plane shown in perspective view contains a dislocation segment (thicker, blue line) that is undergoing thermally activated advancement. In the initial state (a), the dislocation is in stable equilibrium. The black dots represent stable equilibrium points along the reaction coordinate (which is a spatial axis designated, for the central pinning point, by *x*); the dots *do not* represent the obstacles themselves. In (b), the central region of the dislocation has accessed the activated state (designated by a red dot along the reaction coordinate). In (c), this section of the dislocation has advanced to a new stable equilibrium point (shown in green), where its motion is impeded by some other obstacle. Figure reproduced with permission from Ref. (*3*).

For a very large number of these pinned dislocations, Boltzmann statistics apply and the process can be modeled with an analysis similar to that of Vineyard's. In this picture, work is done during the transition and therefore the Gibbs free energy of activation ($\Delta G_{act} = \Delta H_{act} - T\Delta S_{act}$) is used, where the activation enthalpy is $\Delta H_{act} = \Delta U_{act} - \Delta W_{act}$ and ΔW_{act} is the work done during the transition from initial to activated state (*10*, *11*). In this formulation, the overall strain rate $\dot{\varepsilon}$ can be described with an Arrhenius form (*12*):

$$\dot{\varepsilon} = \dot{\varepsilon}_0 \exp\left(-\frac{\Delta G_{act}}{k_B T}\right), \tag{6.3}$$

where $\dot{\varepsilon}_0$ is an appropriate pre-exponential factor. Therefore, using thermodynamics and rearranging Eq. 6.3, the rigorous definitions of activation volume ΔV_{act} and activation enthalpy can be determined as follows (*8*, *12*):

$$\Delta V_{act} = -\left(\frac{\partial \Delta G}{\partial \sigma^*} \right)_T = -k_B T \left(\frac{\partial \ln\left(\dot{\varepsilon}/\dot{\varepsilon}_0\right)}{\partial \sigma^*} \right)_T , \tag{6.4}$$

$$\Delta H_{act} = -\left(\frac{\partial\left(\Delta G/T\right)}{\partial\left(1/T\right)} \right)_{\sigma^*} = k_B T^2 \left(\frac{\partial \ln\left(\dot{\varepsilon}/\dot{\varepsilon}_0\right)}{\partial T} \right)_{\sigma^*} , \tag{6.5}$$

where σ^* is the resolved shear stress acting on the dislocation. It is important to note that activation volume does not by definition describe an actual physical volume, but, as will be discussed later, it is sometimes associated with one.

In principle, these quantities should be directly measurable by experiment. In practice, it remains difficult to interpret experimentally measured values of activation volume and enthalpy, as is clearly elucidated by Hirth and Nix (*9*). The first problem comprises the accurate determination of the stress. The exact state of stress acting at the local area where the reaction is taking place is often complex and difficult to accurately specify. Additionally, the measured, macroscopic rate involves the action of many microscopic processes, which may not all experience the same state of stress. Second, the stress acting locally may change over the course of a test, even if the macroscopic applied stress is constant. Third, the pre-exponential factor ($\dot{\varepsilon}_0$ in Eq. 6.3) cannot be measured independently, so it must be assumed constant with respect to stress and temperature. Finally, at low stress levels, the reverse dislocation jump rate is no longer

negligible and the rate equation needs to be modified to include a reverse term. As will be shown, each of these difficulties has an analog in the analysis of atomic-scale wear.

Despite all of these difficulties, measured values are useful as a signature for a given process and have been fruitfully compared across different experiments with significant success. In many cases, they can even be related to physical quantities. For example, the work done ΔW_{act} is often further defined as $\sigma^* \Delta V_{act} = \sigma^* b \Delta A_{act}$ where b is the Burgers vector of the dislocation and ΔA_{act} is the area swept out by the dislocation as it moves from the initial to the activated state (*10*, *11*). This relation allows the dislocation behavior to be associated with the distribution of obstacles, enabling understanding and predictions for the behavior of materials undergoing plastic flow.

However, dislocation-mediated plastic flow also provides examples where reaction rate theory *cannot* be applied. For instance, dislocation motion is opposed not only by the short range forces described above, but also by long range forces such as elastic interactions with other dislocations (*13*). The energy barriers from the latter forces can be too large to be overcome by thermal activation. Therefore, the thermally activated description will only apply up to some critical temperature where the flow stress reaches the *athermal limit*. As temperature increases further, the flow stress will continue to decrease, but now due to the variation of shear modulus G with temperature. Thermal softening is an entirely different effect and any attempts to model flow stress in this regime using a thermally activated model would yield meaningless values of activation parameters. There are countless examples of other processes, some of which might even be highly temperature-dependent, where the macroscopic behavior is *not* described by an aggregate of a large number of local processes, where the energy barrier is too small

(relative to $k_B T$) for Boltzmann statistics to apply, or where for some other reason the formalism of transition state theory cannot be applied.

Reviewing the well-established literature on thermally activated plastic flow provides useful insights, which will be applied in the following sections to the developing theory of thermally activated atomic-scale wear. In particular, this example demonstrates the usefulness of a clear description of the microscopic mechanism underlying the larger behavior, including a picture of the transitioning system in its initial and activated states. The example also demonstrates the challenges of analyzing the model and interpreting experimentally measured parameters.

6-2: Formalizing the application of reaction rate theory to wear

As discussed in Sect. 2-2, several recent notable investigations have applied reaction rate theory to the analysis of atomic-scale wear. In particular, recent work by Park *et al*. (*14*), Sheehan (*15*), Gotsmann and Lantz (*16*), and Bhaskaran *et al*. (*17*) experimentally measured wear of nanoscale contacts and analyzed results using an Arrhenius analysis. The analysis of all four papers is built on the assumption that the fundamental rate of atom loss (atoms removed per second) due to wear can be described as:

$$\begin{aligned} k_{atom-loss} &= k_0 \exp\left(-\frac{\Delta G_{act}}{k_B T}\right) \\ &= k_0' \exp\left(-\frac{\Delta U_{act}}{k_B T}\right)\exp\left(\frac{\sigma \Delta V_{act}}{k_B T}\right), \end{aligned} \tag{6.6}$$

where k_0 is some pre-factor analogous to $\dot{\varepsilon}_0$ in plastic flow, and σ represents the stress component that lowers the activation barrier – though the various authors disagree about which stress component this should be. (Note that in Eq. 6.6 and subsequent equations, the term containing the entropy of activation has been subsumed into the pre-factor k_0'.) The following section probes the analysis and assumptions of this approach in light of the discussion in Sect. 6-1.

While the many difficulties of accurately extracting and interpreting values of experimentally measured parameters will be discussed below, it is interesting to compare values as they are reported in the various studies, as shown in Table 6.1. First of all, the order of magnitude of all measured parameters is consistent with a highly localized activation reaction involving a small number of atoms and the rupture of a small number of bonds. Second, the reported activation energies for wear of the covalently bonded solids (silicon and silicon-containing DLC probes) are quite similar in the range of 1 eV, while energies of the ionically bonded solids (sodium chloride and calcite) are lower. It should be noted that due to the form of the shear stress, the model used in the Gotsmann and Lantz study only allows effective activation parameters to be extracted since, mathematically, the *effective* activation barrier $\Delta U_{act} - \tau_0 \Delta V_{act}$ and the *effective* activation energy $\xi \Delta V_{\text{act}}$ cannot be further broken down. Through separate studies of the pressure-dependence of velocity, the authors were able to measure $\xi = 0.5$ for a silicon probe on polyaryletherketone (*18*), therefore an effective activation volume of 55 Å^3 corresponds to an activation volume of 110 Å^3. For reference, typical values of activation parameters for some other common thermally activated processes are included

in Table 6.1. As mentioned, the measured values for a thermally activated picture of wear are consistent with the order of magnitude of these other highly localized processes.

Table 6.1: Experimentally-determined values of activation energy and volume for earlier atomic-scale wear studies, and also for other processes that are known to be thermally activated. Activation volumes for the latter processes are typically given in units of the Burgers vector that is typically 2.5-6 Å, and therefore b^3~10-200 Å^3. The ranges of numbers given are for very different materials and typically scale with the degree of covalent bonding between neighboring atoms. Table reproduced with permission from Ref. (*3*).

System	Activation energy	Activation volume	Ref.
atomic-scale wear of calcite sample	0.80±0.20 eV	37±3 Å	*(14)*
atomic-scale wear of NaCl sample	0.34±0.17 eV	86±6 Å	*(15)*
atomic-scale wear of Si tips	0.98±0.04 eV	55±35 Å (110±70Å [a])	*(16)*
atomic-scale wear of Si-containing DLC tips	0.34±0.17 eV	86±6 Å	*(17)*
(Typical values for other thermally activated processes)			
dislocation nucleation (forest) in bulk		100 - 1000 b^3	
dislocation nucleation at surfaces	0.1 - 0.6 eV	1 - 10 b^3	*(20)*
atomic vacancy creation (Schottky defect)	0.1 - 7 eV		*(21)*
atomic vacancy hopping	0.05 - 0.5 eV	0.02 - 0.2 b^3	*(22)*

[a] Assume ξ ~ 0.5 (Cannara, R.; Gotsmann, B.; Lantz, M. A. Unpublished results)

6-2-1: Expanding on the model of atomic-scale wear as a thermally activated process

While a transition state analysis does appear to fit the data quite accurately for the different types of wear studies mentioned, it is still important to ask the question of whether a thermally activated model can be meaningfully applied. The primary test for whether a process obeys Boltzmann statistics, and thus can be considered thermally activated, is a study of the variation in the rate of the process with temperature. Such studies have been conclusively carried out for plastic flow, as discussed in Sect. 6-1.

This temperature dependence has not yet been demonstrated for atomic-scale wear, though there has been some experimental work showing Arrhenius behavior of *macroscale* wear (*23*). While the one atomic-scale study where temperature was varied (*15*) was consistent with a thermally activated process, only two similar temperatures could be accessed experimentally. There has not yet been a systematic study examining atomic-scale wear over a wide range of temperatures. The thermally activated formalism provides one potentially powerful way to analyze the data. However, without experimental demonstration of the temperature dependence, it must be applied with caution.

Further, if atomic-scale wear is a thermally activated process, one must describe the specific atomic-scale mechanism by which it progresses, including a picture of the system in its initial, activated, and final states. The aforementioned studies implicitly propose that the underlying local process is one of atom-by-atom attrition, analogous to dissolution or desorption of atoms from a surface. This is appealing since dissolution and desorption are commonly modeled as thermally activated processes and it is intuitively reasonable to model atomic-scale wear as a stress-assisted version of the same mechanism. It is useful to take this one step further by creating a schematic picture similar to that shown in Fig. 6.2. An example of such a model is shown and described in Fig. 6.3.

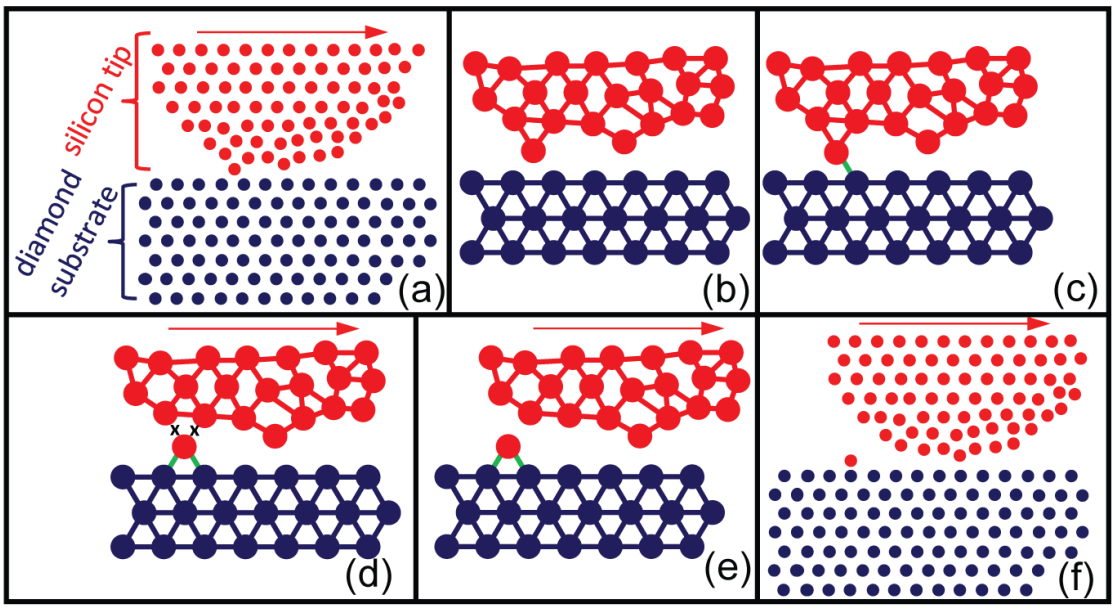

Figure 6.3: A potential reaction pathway for nanoscale wear has been proposed in which the rate-limiting reaction is the initial formation of a chemical bond across the interface. A proposed reaction is shown schematically, where a silicon tip slides slowly (with respect to lattice vibrations) over a diamond substrate (a), with atomic-scale detail in (b). The entire system is in quasi-static equilibrium. In (c), a single tip atom has undergone thermally-activated bond formation with an atom from the substrate. Thus, in the language of reaction rate theory, (b) represents the *initial state* for this reaction, (c) represents the lower energy *final state*; the intermediate, maximum energy *activated state* is not shown. In some cases, the newly formed bond will break (not shown), but in other cases, additional reactions will result in more bond-formation to the substrate and the breaking of bonds to the tip (d). In this case, an atom is transferred to the surface (e) and the tip has undergone wear by one atom. The tip continues sliding as before (f) and can start the process over again.

In Fig. 6.3(a), a sharp silicon tip is shown sliding across a flat diamond substrate. In principle, the tip could slide like this for long periods without any reactions across the interface and without any wear. Fig. 6.3(b) shows an atomic-scale view of the tip/sample interface; this represents the *system* in which the thermally activated process (described by reaction rate theory and Arrhenius kinetics) occurs. It is assumed that the tip is sliding slowly enough to consider the system to be in quasi-static equilibrium.

Given typical sliding speeds (roughly 1 nm – 1 μm per second), and given typical atomic vibration frequencies (roughly 10^{12} – 10^{14} /s), the tip moves less than 10^{-18} m/vibration and thus there are 10^{6} vibrations before the tip has moved by 1 pm. Therefore, the assumption of quasi-static equilibrium is reasonable. This is a critical assumption because reaction rate theory relies on Boltzmann statistics, which describes equilibrium systems – further, the initial, activated and final states must be in equilibrium with one another. Thus, Fig. 6.3(b) represents the system in its *initial state* (before any bonds are formed across the interface) and Fig. 6.3(c), where one bond has formed across the interface, represents the same system in its *final state* with respect to a thermally activated bond formation process. The *activated state* is some intermediate state (not shown) between (b) and (c), where the system's free energy is maximized. The state shown in Fig. 6.3(c) is assumed to be lower energy than the one shown in Fig. 6.3(b) since the new bonds make one of the tip atoms more highly coordinated. Thus, the activation barrier of the reverse reaction is higher than that of the forward reaction (as is the case in Fig. 6.1), and the reverse rate of reaction will be much slower than the forward rate.

The point shown in Fig. 6.3(c) might be quite stable were the tip not sliding; however, the motion of the tip (induced by cantilever forces that are far stronger than single atom bonds) will *require* bonds rearrangement. If the newly-formed bond (green) were to break, then the tip would slide on unaffected and no wear would occur. However, it is also possible that additional bonds will form to the substrate and in some cases, the bonds that previously held this atom to the tip will break instead (as is the case shown in Fig. 6.3(d), then the atom is left behind on the surface and the tip has

experienced wear. Thus the bond-breaking step represents a competition between two possible sub-processes; one of which causes wear, one of which does not. It is possible that one of these sub-processes is more likely than the other. For instance, since the surface atom was low-coordinated on the sharp tip and would often find a deep energy minimum on the surface, it is possible that the tip atoms are typically the ones that break. Alternatively, since the surface atom will usually have multiple bonds to the tip and only form one bond to the surface (at least initially), then it might be more likely that the newly-formed tip/sample bonds will break. It is even possible that the process of bond breaking is *also* thermally activated, complicating the kinetics further.

This wear process is analogous to wear that has been observed in molecular dynamics simulations of diamond-like carbon sliding over diamond (*24*). It is further postulated here that the first process, bond formation, will be the rate limiting step and will have the greatest dependence on stress. This is supported by literature regarding molecular dynamics potentials, which define an energy barrier between the "non-bonded" and "bonded" states of two adjacent atoms (*25*). However, the specific atomic-scale processes that lead to wear are unknown, and thus this remains an important open question.

6-2-2: The extraction of activation parameters for wear

While the measurement of activation parameters is conceptually simple, the actual process of extracting reliable values is quite difficult. The difficulties enumerated by

Hirth and Nix with regard to dislocation motion (discussed in Sect. 6.1) have even more significant analogues in the studies of atomic-scale wear.

The first significant challenge is the correct identification of the stress state. In atomic-scale wear studies, the applied load is controlled as an input variable; the applied stress cannot be varied directly. Therefore, one must determine the location and values of the stress components that have the primary effect and then find a model for calculating this stress from known variables. Park *et al*. (*14*)and Sheehan (*15*) both assumed that interfacial contact stresses are the most relevant and rely on Hertzian contact mechanics to calculate values (though Sheehan includes an added adhesion force in the manner of the DMT model). Alternatively, the Gotsmann and Bhaskaran studies (*16*, *17*) propose that the interfacial shear stress has the most significant effect, yet these still must rely on models to calculate this stress from experimentally controllable parameters.

Adding to this first challenge of quantifying the stress state is the problem of the uniformity of stress throughout the contact interface. In the analysis of thermally activated processes, the system is treated as if it were comprised of a very large number of identical microscopic systems attempting the same transition. For a sliding tip, there are a large number of atoms that comprise the tip-sample contact and for realistic sliding times, there will be a very large number of "attempts". However, not all atoms experience the same energy landscape nor the identical stress state. With regard to energy landscape, consider the case of a single crystal tip with stepped edges (Fig. 2.1(d)) sliding on a surface: atoms with a lower coordination number such as those at a step edge experience a very different energy landscape than atoms on the bottom surface of the tip with a higher coordination. This implies that wear of such a hypothetical single crystal

tip would occur by loss of atoms from the step edges which recede. A similar topic is specifically discussed in the work of Maw *et al*. (*26*), where measurable wear is confined exclusively to the step edge. In this case, an analysis of the wear rate would probe the activation parameters of the dissolution of atoms *at the step edges*. Alternatively, in experiments where the wearing surface is expected to be amorphous (e.g. a native silicon oxide), there is likely to be a distribution of coordination environments of surface atoms. Wear then would occur by the removal of atoms in the lowest coordination states and the wear process would result in a continuous change in the coordination state of any given surface atom until it is removed by wear. As such, an analysis of the wear rate would probe the activation parameters of the process of removing the most weakly bound atoms.

The distribution of stress in the contact zone is also an important consideration. The simplest assumption is that the constant stress equals the average value across the contact. A more accurate treatment would be to apply contact mechanics models to estimate the stress distribution within the contact. For example, for a Hertzian contact, the maximum value of the compressive stress is 1.5 times the average value. Similar deviations from the results of contact mechanics models can be expected for the radial and shear stress components. It is important to note that, due to the nonlinearity of the relation between stress and wear rate (Eq. 6.6), this modest variation in stress could result in a much larger variation in wear rate. For the case of tip wear, one could argue (as in Gotsmann and Lantz (*16*)) that the progression of tip-shape as it is continuously worn will level out differences in stress. This, of course, only applies to the variation in a classical continuum-theory contact model. Such a treatment is not sufficient to describe variations at the atomic level, which are clearly relevant for atomic scale wear. For

example, using molecular dynamics simulations, of the contact between an amorphous spherical tip and an atomically flat single crystal surface, Luan and Robbins (*27*) have shown that the peak pressure acting on an individual atom in the tip can be up to 5-6 times the average value, depending on atomistic surface detail. Whatever assumptions are made about the state of stress under the tip, these variations in stress should be accounted for in any analysis based on transition state theory.

The second difficulty discussed in Sect. 6.1 is the changing local stress over the course of a test – even for a constant applied load. In Hirth and Nix (*9*), this referred to the fact that plastic flow altered the structure of the material and thus changed the local stress acting on the dislocation. In atomic-scale wear, even as the applied load is held constant, the modification that occurs due to wear of either the tip or surface means that the contact geometry is constantly changing, and thus the surface stresses are constantly changing. Of the three models described above, only Gotsmann and Lantz (*16*) attempt to address this issue with *in-situ* pull-off tests to get a measure of tip radius in real time as the wear test is progressing.

The third difficulty discussed in Hirth and Nix is the assumptions about quantities that are not directly accessible. In plastic flow, this involves assuming that the pre-factor ($\dot{\varepsilon}_0$ in Eq. 6.3) is constant with respect to stress and temperature. The present studies on wear make similar assumptions about the pre-factor k_0 and, in addition, make even stronger assumptions about the form of the rate equation. In plastic flow studies, the activation volume is measured by plotting the logarithm of the rate of the process against the applied stress. As shown in Eq. 6.4, the slope of the plotted curve is a direct

measurement of the activation volume. In contrast, the atomic-scale wear models assume a specific form of the work term ($\Delta W_{\text{act}} = \sigma \Delta V_{\text{act}}$) and further assume that the activation volume is a constant with respect to stress (which it need not be, as discussed in Refs. (*28*) and (*1*, *19*)). Once these assumptions are made, the authors extract an activation volume by choosing the parameter that allows the best fit to the experimental data. If the assumptions are valid, then curve fitting should be an acceptable way to ascertain these values. However, these assumptions are not required if the activation volume is measured in the traditional, direct fashion.

The final difficulty involved in extracting activation parameters arises from the attempt to calculate activation energies (and thus enthalpies) with limited or no temperature variation performed in the experiment. The activation enthalpy ΔH_{act} can be directly extracted by measuring the rate of wear at a variety of temperatures, as shown in Eq. 6.5. Sheehan's study (*2*, *15*) varied temperature and reported an activation energy ΔU_{act} of 0.34 eV with a reported error of 50% due to the limited temperature variation. In Park *et al.* (*1*, *14*), Gotsmann and Lantz (*3*, *16*), and Bhaskaran *et al.* (*1*, *17*), an attempt is made to calculate the activation energy ΔU_{act} by assuming values for all other parameters in the wear rate equation and then solving for ΔU_{act}. However, values calculated in this fashion can depend strongly on the choice of parameters. The pre-factor k_0 is often assumed to be a lattice vibration frequency and is estimated as 10^{13}/s in Park *et al*. (*4*, *14*) and 10^{12}/s in Gotsmann and Lantz (*5*, *16*). In Gotsmann and Lantz, there are additional constants: the reference velocity v_0 is taken as the sliding velocity of 1.5 mm/s (*4*, *18*), the dimensionless pressure-dependence ξ was subsequently measured as 0.5 (*2*, *18*), and τ_0 does not need to be directly estimated as it is wrapped into the

effective activation energy. Finally, and most significantly, a choice must be made for the form of ΔW_{act} – in particular, which stress does work on the system during the thermally activated event (Park *et al.* (*2*, *14*), Sheehan (*6*, *7*, *15*), and the papers by Bhaskaran *et al.* (*8*, *17*) and Gotsmann and Lantz (*9*, *16*) do not agree on the relevant stress component, as discussed in the previous sub-section). Once this relevant stress is chosen, its value must be calculated as a function of controllable or measurable variables (applied load, material parameters, tip radius, etc.). This calculation depends on the model chosen to describe the contact (Hertz, one that includes adhesion, or a non-continuum simulation). Due to its presence in the exponential, errors in the calculation of the work term will be even more impactful than errors in the pre-factor. A direct measurement of the activation enthalpy according to Eq. 6.5 avoids the need for these assumptions.

Despite all of the aforementioned difficulties, four studies managed to extract activation parameters. And, as discussed earlier, it is impressive that the activation parameters all fall within reasonable bounds for atomic bond-breaking events.

6-2-3: The interpretation of activation parameters

The interpretation of these experimentally measured values of activation parameters also differs among the various authors. In Park *et al.* (*3*, *14*), the authors assert that the activation volume is nearly equal to the volume of an ion in the calcite lattice and that the activation energy is comparable to the energy required for vacancy formation on a step edge. Such broad comparisons can be useful to ensure that measured

values are of the right order of magnitude; however, in Sheehan's article (*10*, *11*, *15*), the activation volume is explicitly described as the volume removed per pass of the scanning probe. This interpretation is not consistent with transition state theory; in the context of the prototypical model shown in Fig. 6.3, the total worn volume describes the difference between state (a) and state (e), while the activation volume describes only the transition from state (b) to state (c). This demonstrates the utility of clearly describing the proposed thermally activated process, including the specification of the system in its initial, activated, and final state. The Gotsmann study (*12*, *16*) does not attribute the activation volume to any real space quantity, but compares the order of magnitude of activation parameters to quantities associated with bond breaking.

From a transition state theory perspective, the primary utility of activation parameters is as a signature of the underlying atomic-scale mechanism that underlies the macroscopic phenomenon. They allow for comparison among different sets of experiments and against theoretical values for the proposed underlying thermally activated reaction. Once a concrete picture of the atomic-mechanism of wear is proposed (along the lines of Fig. 6.6), then atomistic simulations of the process can be created to calculate expected values of the activation energy and activation volume. These expected values can be compared directly against measured values to provide further support for a thermally activated picture.

6-3: Suggested future investigations to interrogate the fundamentals of wear on the atomic scale using a model based on reaction rate theory

To address some of the remaining questions explored in Sect. 6.2, the present section outlines future studies that would allow an even deeper investigation of the fundamental origins of atomic-scale wear. Specifically, further experimental investigation is suggested into the effect of temperature on wear, stress and velocity on atomic-scale wear. Also, a brief treatment of atomistic simulations of wear is presented along with past and future contributions to a better understanding of the science of atomic scale wear.

6-3-1: Experimentally demonstrating wear mechanisms and wear kinetics in high resolution

The discussion in Sect. 6-2-1 laid out a potential wear mechanism that was thermally activated and could obey stress-mediated Arrhenius kinetics. However, there are many other wear mechanisms that may be competing or even concurrent with atom-by-atom transfer. High resolution *in situ* studies could be used to determine the mechanism(s) of wear that are occurring in a given set of conditions. The same high-resolution studies could be used to measure relevant forces and volume losses with high enough precision to test the proposed kinetics of a wear model based on reaction rate theory. These in situ studies are the topic of Chapter 7 of the present dissertation.

6-3-2: Experimentally demonstrating the effect of temperature on atomic-scale wear

As discussed, thermal activation is just one of many possible frameworks for describing wear at the atomic scale. One way to clearly demonstrate that the kinetics are governed by such a framework would be to demonstrate an exponential dependence of the rate of atom transfer on inverse temperature (as predicted by the Arrhenius rate equation, Eq. 6.6. Ideally a wear study of this kind would vary temperature over several orders of magnitude as has been done with plastic flow as described in Sect. 1.

Unfortunately, a detailed temperature study is challenging for a variety of reasons. Aside from the experimental difficulty of heating or cooling the tip-sample contact, the analysis will be complicated by the temperature dependence of other parameters, especially friction. The temperature dependence of friction can be substantial in some cases (*8*, *12*, *29*, *30*) and even non-monotonic (*9*, *31*, *32*) and thus might alter the shear stresses acting at the interface. Additionally, a large enough increase in temperature will cause softening of the mechanical properties of the tip/sample materials, thus altering the geometry and stresses of the contact. Therefore, such a temperature study would ideally measure friction and wear concurrently, or be performed on a system where the temperature dependence of friction and mechanical properties is not strong, or has been determined previously such as for a silicon tip sliding over Si, SiO_2, SiC, or NaCl (*10*, *11*, *29-33*).

Furthermore, there is no guarantee that the activation volume itself is constant with temperature (as discussed in (*13*, *28*)), so it would be useful to have a comprehensive analysis that performs a study similar to Park *et al.* (*14*) or Gotsmann and Lantz (*15*, *16*) *at each temperature*. Finally, the pre-factor (*f* in Eq. 6.1 or k_0 in Eq. 6.6,

designated the *attempt frequency* above) may vary with temperature. Depending on dissipative processes active when the system moves along the lowest energy path (Fig. 6.1), f can increase or decrease with increasing temperature (*2*, *16*).

It would be difficult for all of the above effects to be addressed in a single study of atomic scale wear. Rather, these points are suggested as guidelines for the design of new experiments, and for the analysis of the body of wear data as it develops, especially with regard to temperature.

6-3-3: Determining which is the primary "activating stress" for atomic-scale wear

The free energy of activation, ΔG_{act}, is reduced when an applied stress does work during the thermally activated transition. However, each of the above models assumes that a different stress does work during the transition: the Park *et al*. study uses the Hertzian radial stress in its calculation; Sheehan uses the Hertzian shear stress at the interface; and Gotsmann and Lantz use the interfacial shear stress induced by sliding friction. It is crucial to determine which of these stresses is primarily involved in wear for accurate data analysis. As discussed in Sect. 6-2, it remains unclear which stress component is the most relevant for reducing the activation barrier for wear. Intuitively, it seems that the compressive stress would be most relevant for bond formation, while tensile or shear stresses would be most relevant for bond breaking.

In principle, it should be possible to distinguish which stress does work (and thus which is the *activating stress*) through further study of the dependence of wear on the applied load $F_{applied}$. However, in many models of contact (such as Hertz (*17*, *34*) and

DMT (*18*, *35*)) the maximum values of compressive, shear, and tensile stress have the same dependence on applied load. For instance, in Park *et al.* and in Sheehan, Hertzian stresses, which are present in static contact and depend only on mechanical properties of the materials and the shape of the tip, have a dependence of $F_{applied}^{1/3}$ (*23*, *36*). Even the interfacial shear stress $\tau_{friction}$ is often approximated (as in Gotsmann and Lantz) with a linear dependence on pressure – equivalent to Eq. 2.16 for a single value of velocity. Thus it would be predicted to have a similar functional dependence on load as the other stress components. The only case that should be readily distinguishable is if interfacial shear stress is the dominant value and a material pair is studied where the pressure dependence in Eq. 2.16 $\xi = 0$. In this case, there should be no distinguishable dependence of wear rate on applied load. More generally, simulation techniques such as atomistic, molecular dynamics, or other modeling may prove useful in simulating proposed reactions and determining the impact of different stress components, as discussed below.

6-3-4: Disentangling the effect of velocity on atomic-scale wear

The underlying equation of a thermally activated picture of atomic-scale wear (Eq. 6.6) is independent of velocity. Therefore, if the shear stress does not enter into the free energy of activation (as assumed by Park *et al.*, Sheehan, and Kopta and Salmeron) or the shear stress does not depend on velocity (as in the description from Ref. (*15*, *37*)) then the rate of wear is independent of tip velocity. The only predicted effect of sliding speed in these models is to change the amount of time in contact for a given sliding distance. Thus the rate of successful atom transfers per second will be unchanged, but

the amount of wear observed for a given sliding distance will scale linearly with contact time and so inversely with sliding velocity.

If the primary dependence of rate of atom loss is assumed to be on interfacial shear stress (as in Gotsmann and Lantz), then the picture is somewhat more complicated interfacial shear stress is assumed to depend on sliding velocity. This frictional shear stress has itself been described as a thermally activated process in models of single-asperity interfacial friction whereby the tip slides in quasi-static equilibrium along the corrugated energy surface representing the sample (*25*, *38*). The latter is captured in the Briscoe and Evans equation expressing the shear stress applied to an interface due to sliding friction (Eq. 2.16). As mentioned, although this equation was originally derived for organic thin films (*14*, *39*), it has been shown to be applicable to a variety of tip-sample systems and to stick-slip motion as derived from the Prandtl-Tomlinson model (*15*, *40-43*). Alternatively, for smaller scanning speeds, a different limit of velocity-dependent friction has been proposed of the form (*16*, *17*, *44*):

$$\tau_{friction} \propto const + \ln\left(\frac{v}{v_0}\right)^{2/3} \quad (6.9)$$

Each of the above scenarios will predict different dependences of wear rate on sliding velocity. Therefore a combined, systematic study of the velocity dependence of friction and wear could shed light on this question. Concurrent measurements of the frictional force, combined with knowledge of tip shape, would permit the direct calculation of the shear strength, circumventing the need for an assumed form of τ and allowing an evaluation of previous assumptions.

It should be noted, however, that varying the time or velocity scale in experiments to uncover the underlying kinetics ideally requires variation over several orders of magnitude. Especially with exponential equations, false trends can be easily detected with insufficient variation. However, experimentally this may be difficult to accomplish with many AFM systems. For the case of atomic-scale wear, the wear rates can be so low that high scanning speeds and long duration experiments are required to accurately measure the wear rate. For example, in the work of Gotsmann and Lantz (*16*, *26*), a sliding velocity of 1.5 mm/s in combination with sliding times of up to one week were required to quantify low-load wear. Acquiring the same amount of data at a significantly lower sliding velocity is unfeasible.

6-3-5: Using atomistic simulations to elucidate atomic-scale wear

A key complement to the above-mentioned experimental work will be computer simulations based on molecular dynamics (MD) and ab initio techniques. Already, there is a developing body of literature where these techniques are used to characterize the contact area and stresses (normal and frictional) of a nanoscale contact (for example, Refs. (*16*, *27*, *45*, *46*). Some of these models have even been extended to model certain aspects of wear. For instance, in a study on the adhesive loads associated with atomically-sharp diamond tips, Jarvis *et al*. (*27*, *47*)slide the tip along the surface and find that the contacting atom is removed from the tip after just 1.6 Å of sliding. Further, Harrison and Brenner (*9*, *48*) use MD models to slide two diamond surfaces past one another and find that wear initiates by the removal of hydrogen from the H-terminated

surfaces and continues by radical recombination, transient surface adhesion and debris formation. Other studies use MD to model the sliding of atomically flat surfaces in intimate contact and demonstrate plastic deformation and mechanical mixing of the surface material (*16*, *49*, *50*).

There has not yet been an atomistic simulation of wear in the context of transition state theory. A full treatment of the details of such a simulation is beyond the scope of this paper. Yet it can be imagined to follow the style of earlier work modeling the stress-dependent hydrolysis of silica in water (*22*, *28*). In this work, Zhu *et al*. use molecular orbital theory and the nudged elastic band (NEB) technique to find the minimum energy path along the potential energy surface, giving a direct measurement of the predicted activation energy for the proposed reaction. Not only are the authors able to predict the dependence of activation barrier on stress, but they go even further to show that different reaction pathways can be thermodynamically favorable at different stresses and that, when the stress is high enough, a given pathway may no longer require thermal activation to overcome the barrier.

Overall, simulation techniques make possible: the elimination of certain assumptions, such as the applicability of continuum mechanics; the study of wear under conditions that are difficult or impossible to access experimentally; and the creation of testable predictions that can be directly compared with experimental results. It is likely that atomistic simulations will be critical to solving many of the questions raised in this article.

6-4: Conclusions

This chapter has reviewed recent atomic-scale wear studies in light of formal transition state theory. There are several primary conclusions. First, substantial experimental evidence demonstrates that atom-by-atom wear occurs at single-asperity contacts for a variety of materials, highlighting the need to understand this process more deeply. Second, many of the previous analyses of these experiments used equations taken from reaction rate theory, but did not fully address the physics behind such a model. Specifically, any such analysis should specify the following: the atomic-scale transition which is proposed to be thermally activated; the configuration of the system in its initial, activated, and final states; and the assumptions made about the tip-sample system such that the requirements of transition state theory are satisfied and Boltzmann statistics can be applied. Third, the method of measurement and the physical interpretation of activation parameters were shown to vary widely from author to author. In particular, while various studies measured activation volumes directly, the values obtained depended on which stress component was chosen as the activating stress and how this component was calculated. Additionally, various authors offer differing interpretations of the physical meaning of measured values – some of which are demonstrably incorrect. Finally, further experimental work is required to confirm and interrogate models based on transition state theory.

The concepts discussed in this chapter provide new insights into the analysis of nanoscale wear, and provide a roadmap for characterizing a wide array of materials in a robust, fundamental way that might even have predictive potential. However, significant

questions remain. For instance, for specific materials and conditions, is wear caused (or rate-limited by) a tribochemical reaction (as opposed to fracture, plastic deformation, or some other mechanical effect)? If the wear is confirmed as tribochemical, can it be confirmed that Arrhenius kinetics can be applied? (Are the extensive set of assumptions (discussed succinctly in Sect. 6-1) satisfied for the nanoscale wear reaction?) If Arrhenius kinetics can be applied, what is the stress state acting on the contacting atoms and which stress in particular will serve as the "activating stress" σ in Eq. 6.6? In reality, the forces acting on individual atoms will vary significantly across the contact; should this stress represent some average? In the next chapter, experimental results using an *in situ* TEM methodology will be presented which will address some of these questions.

6-5: References

(1) Christian, J. W. *The Theory of Transformations in Metals and Alloys*; Pergamon, 1975.
(2) Hanggi, P.; Talkner, P.; Borkovec, M. Reaction-rate theory: fifty years after Kramers. *Rev. Mod. Phys.* **1990**, *62*, 251–341.
(3) Jacobs, T. D. B.; Gotsmann, B.; Lantz, M. A.; Carpick, R. W. On the application of transition state theory to atomic-scale wear. In; 2010; Vol. 39, pp. 257–271.
(4) Vineyard, G. H. Frequency factors and isotope effects in solid state rate processes. *J. Chem. Phys. Sol.* **1957**, *3*, 121–127.
(5) Wert, C.; Zener, C. Interstitial Atomic Diffusion Coefficients. *Physical Review* **1949**, *76*, 1169–1175.
(6) Rohde, R. W.; Pitt, C. H. Dislocation velocities in nickel single crystals. *J. Appl. Phys.* **1967**, *38*, 876–879.
(7) Kauzmann, W. Flow of solid metals from the standpoint of the chemical-rate theory. *Trans. AIME* **1941**, *143*, 57–83.
(8) Gibbs, G. B. Thermodynamics of Thermally-Activated Dislocation Glide. *Phys. Status Solidi* **1965**, *10*, 507–&.
(9) Hirth, J. P.; Nix, W. An Analysis of Thermodynamics of Dislocation Glide. *Phys. Status Solidi* **1969**, *35*, 177–&.
(10) Kocks, U. F.; Argon, A. S.; Ashby, M. F. Thermodynamics and Kinetics of Slip. *Progress in Materials Science* **1975**, *19*, 1–281.
(11) Gibbs, G. B. On Interpretation of Experimental Activation Parameters for Dislocation Glide. *Philosophical Magazine* **1969**, *20*, 867–&.
(12) Taylor, G. Thermally-activated deformation of BCC metals and alloys. *Progress in Materials Science(UK)* **1992**, *36*, 29–61.
(13) Hull, D.; Bacon, D. J. *Introduction to Dislocations*; Pergamon Press Oxford, 1984; Vol. 257.
(14) Park, N. S.; Kim, M. W.; Langford, S.; Dickinson, J. Atomic layer wear of single-crystal calcite in aqueous solution using scanning force microscopy. *J. Appl. Phys.* **1996**, *80*, 2680–2686.
(15) Sheehan, P. The wear kinetics of NaCl under dry nitrogen and at low humidities. *Chem. Phys. Lett.* **2005**, *410*, 151–155.
(16) Gotsmann, B.; Lantz, M. A. Atomistic wear in a single asperity sliding contact. *Phys. Rev. Lett.* **2008**, *101*, 125501.
(17) Bhaskaran, H.; Gotsmann, B.; Sebastian, A.; Drechsler, U.; Lantz, M. A.; Despont, M.; Jaroenapibal, P.; Carpick, R. W.; Chen, Y.; Sridharan, K. Ultralow nanoscale wear through atom-by-atom attrition in silicon-containing diamond-like carbon. *Nature Nanotech.* **2010**, *5*, 181–185.
(18) Gotsmann, B.; Lantz, M. A. Personal communication **2010**.
(19) Li, J. The mechanics and physics of defect nucleation. *MRS Bull.* **2007**, *32*, 151–159.
(20) Zhu, T.; Li, J.; Samanta, A.; Leach, A.; Gall, K. Temperature and Strain-Rate Dependence of Surface Dislocation Nucleation. *Phys. Rev. Lett.* **2008**, *100*, 025502.
(21) Crawford, J. H., Jr; Slifkin, L. M. *Point Defects in Solids. Volume 1. General and Ionic Crystals.*; Plenum Press, 1972.
(22) Zhu, T.; Li, J.; Lin, X.; Yip, S. Stress-dependent molecular pathways of silica–water reaction. *J. Mech. Phys. Sol.* **2005**, *53*, 1597–1623.
(23) Hong, U.; Jung, S.; Cho, K.; Cho, M.; Kim, S.; Jang, H. Wear mechanism of multiphase friction materials with different phenolic resin matrices. *Wear* **2009**, *266*, 739–744.
(24) Gao, G.; Mikulski, P.; Harrison, J. A. Molecular-scale tribology of amorphous carbon coatings: effects of film thickness, adhesion, and long-range interactions. *J. Am. Chem. Soc.* **2002**, *124*, 7202–7209.

(25) Brenner, D. W.; Shenderova, O. A.; Harrison, J. A.; Stuart, S. J.; Ni, B.; Sinnott, S. B. A second-generation reactive empirical bond order (REBO) potential energy expression for hydrocarbons. *J. Phys.: Condens. Matter* **2002**, *14*, 783–802.
(26) Maw, W.; Stevens, F.; Langford, S.; Dickinson, J. Single asperity tribochemical wear of silicon nitride studied by atomic force microscopy. *J. Appl. Phys.* **2002**, *92*, 5103.
(27) Luan, B.; Robbins, M. Contact of single asperities with varying adhesion: Comparing continuum mechanics to atomistic simulations. *Phys. Rev. E* **2006**, *74*, 026111.
(28) Krausz, A. S.; Eyring, H.; Eyring, H.; Eyring, H. *Deformation Kinetics*; Wiley New York, 1975; Vol. 197.
(29) Zhao, X.; Hamilton, M.; Sawyer, W.; Perry, S. Thermally activated friction. *Tribol. Lett.* **2007**, *27*, 113–117.
(30) Zhao, X.; Phillpot, S.; Sawyer, W.; Sinnott, S.; Perry, S. Transition from thermal to athermal friction under cryogenic conditions. *Phys. Rev. Lett.* **2009**, *102*, 186102.
(31) Schirmeisen, A.; Jansen, L.; Hölscher, H.; Fuchs, H. Temperature dependence of point contact friction on silicon. *Appl. Phys. Lett.* **2006**, *88*, 123108.
(32) Jansen, L.; Schirmeisen, A.; Hedrick, J.; Lantz, M. A.; Knoll, A.; Cannara, R.; Gotsmann, B. Nanoscale frictional dissipation into shear-stressed polymer relaxations. *Phys. Rev. Lett.* **2009**, *102*, 236101.
(33) Barel, I.; Urbakh, M.; Jansen, L.; Schirmeisen, A. Multibond dynamics of nanoscale friction: the role of temperature. *Phys. Rev. Lett.* **2010**, *104*, 066104.
(34) Hertz, H. On the contact of elastic solids. *J. reine angew. Math* **1881**, *92*, 110.
(35) Derjaguin, BV; Muller, V.; Toporov, Y. P. Effect of contact deformations on the adhesion of particles. *J. Coll. Int. Sci.* **1975**, *53*, 314–326.
(36) Johnson, K. L. *Contact Mechanics*; 2011; pp. 1–467.
(37) Zworner, O.; Hölscher, H.; Schwarz, U. D.; Wiesendanger, R. The velocity dependence of frictional forces in point-contact friction. *Applied Physics a-Materials Science & Processing* **1998**, *66*, S263–S267.
(38) Carpick, R.; Salmeron, M. Scratching the surface: Fundamental investigations of tribology with atomic force microscopy. *Chem. Rev.* **1997**, *97*, 1163–1194.
(39) Briscoe, B.; Evans, D. The shear properties of Langmuir-Blodgett layers. *Proc. Roy. Soc. A* **1982**, *380*, 389–407.
(40) Riedo, E.; Gnecco, E.; Bennewitz, R.; Meyer, E.; Brune, H. Interaction potential and hopping dynamics governing sliding friction. *Phys. Rev. Lett.* **2003**, *91*, 84502.
(41) Bouhacina, T.; Aime, J. P.; Gauthier, S.; Michel, D.; Heroguez, V. Tribological behavior of a polymer grafted on silanized silica probed with a nanotip. *Phys. Rev. B* **1997**, *56*, 7694.
(42) Gnecco, E.; Bennewitz, R.; Gyalog, T.; Loppacher, C.; Bammerlin, M.; Meyer, E.; Güntherodt, H. Velocity dependence of atomic friction. *Phys. Rev. Lett.* **2000**, *84*, 1172–1175.
(43) Chen, J.; Ratera, I.; Park, J. Y.; Salmeron, M. Velocity dependence of friction and hydrogen bonding effects. *Phys. Rev. Lett.* **2006**, *96*, 236102.
(44) Sang, Y.; Dubé, M.; Grant, M. Thermal effects on atomic friction. *Phys. Rev. Lett.* **2001**, *87*, 174301.
(45) Mo, Y.; Szlufarska, I. Roughness picture of friction in dry nanoscale contacts. *Phys. Rev. B* **2010**, *81*.
(46) Gao, G.; Cannara, R.; Carpick, R.; Harrison, J. A. Atomic-scale friction on diamond: a comparison of different sliding directions on (001) and (111) surfaces using MD and AFM. *Langmuir* **2007**, *23*, 5394–5405.
(47) Jarvis, M.; Pérez, R.; Payne, M. Can atomic force microscopy achieve atomic resolution in contact mode? *Phys. Rev. Lett.* **2001**, *86*, 1287–1290.
(48) Harrison, J. A.; Brenner, D. Simulated tribochemistry: an atomic-scale view of the wear of diamond. *J. Am. Chem. Soc.* **1994**, *116*, 10399–10402.
(49) Kim, H. J.; Karthikeyan, S.; Rigney, D. A simulation study of the mixing, atomic flow and velocity profiles of crystalline materials during sliding. *Wear* **2009**, *267*, 1130–1136.

(50) Rigney, D. A.; Fu, X. Y.; Hammerberg, J. E.; Holian, B. L.; Falk, M. L. Examples of structural evolution during sliding and shear of ductile materials. *Scripta Materialia* **2003**, *49*, 977–983.

CHAPTER 7: Nanoscale wear, Part II: Experimentally demonstrating wear of silicon as a stress-assisted chemical reaction[14]

The present chapter describes *in situ* wear tests performed in the TEM. In this investigation, nanoscale silicon tips of varying geometries were worn by sliding them against a flat diamond substrate. The loading configuration was chosen so that only the adhesive force was acting; no additional external load was applied. As described in Chapter 3, sliding tests were interrupted at specific intervals to assess the instantaneous tip geometry, worn volume, and adhesion force. TEM images and videos were used to ascertain that silicon was removed gradually, in accordance with the atom-by-atom wear mechanism discussed in Sect. 2-4-3, first applied to the wear of tips by Gotsmann and Lantz (*1*). Then, quantitative analysis of loads and volume lost was used to demonstrate that the wear kinetics obeyed the predictions of a wear model based on reaction rate theory.

7-1: Observing and distinguishing wear mechanisms in silicon and its oxide

As discussed in Chapter 6, a physically-based wear model requires specific identification of the process by which material is being removed. In this study, the removal mechanism was identified by using the high-resolution out-of-contact images

[14] Much of this chapter appears in print: Adapted with permission from Jacobs, T. D. B.; Carpick, R. W. *Nature Nanotech.* **2013,** 8, 108-112. Copyright 2013 Nature Publishing Group.

taken at various points throughout the wear test. Figure 7.1 shows the four probes in their initial states, final states and also mid-way through sliding. The probe manufacturing process induces a variable, and occasionally very thick oxide layer that is clearly visible in Fig. 7.1(d). In contrast, some probes (such as is shown in Fig. 7.1(g,j)) had previously undergone a fracture event or other uncontrolled contact prior to testing, so only a thin native oxide is present on the surface of the probe. Therefore, the four process have different, but non-zero, amounts of oxide on their apexes. An example video of a typical wear test performed on these probes can be found in the Supplemental Information of associated with Ref. (*2*).

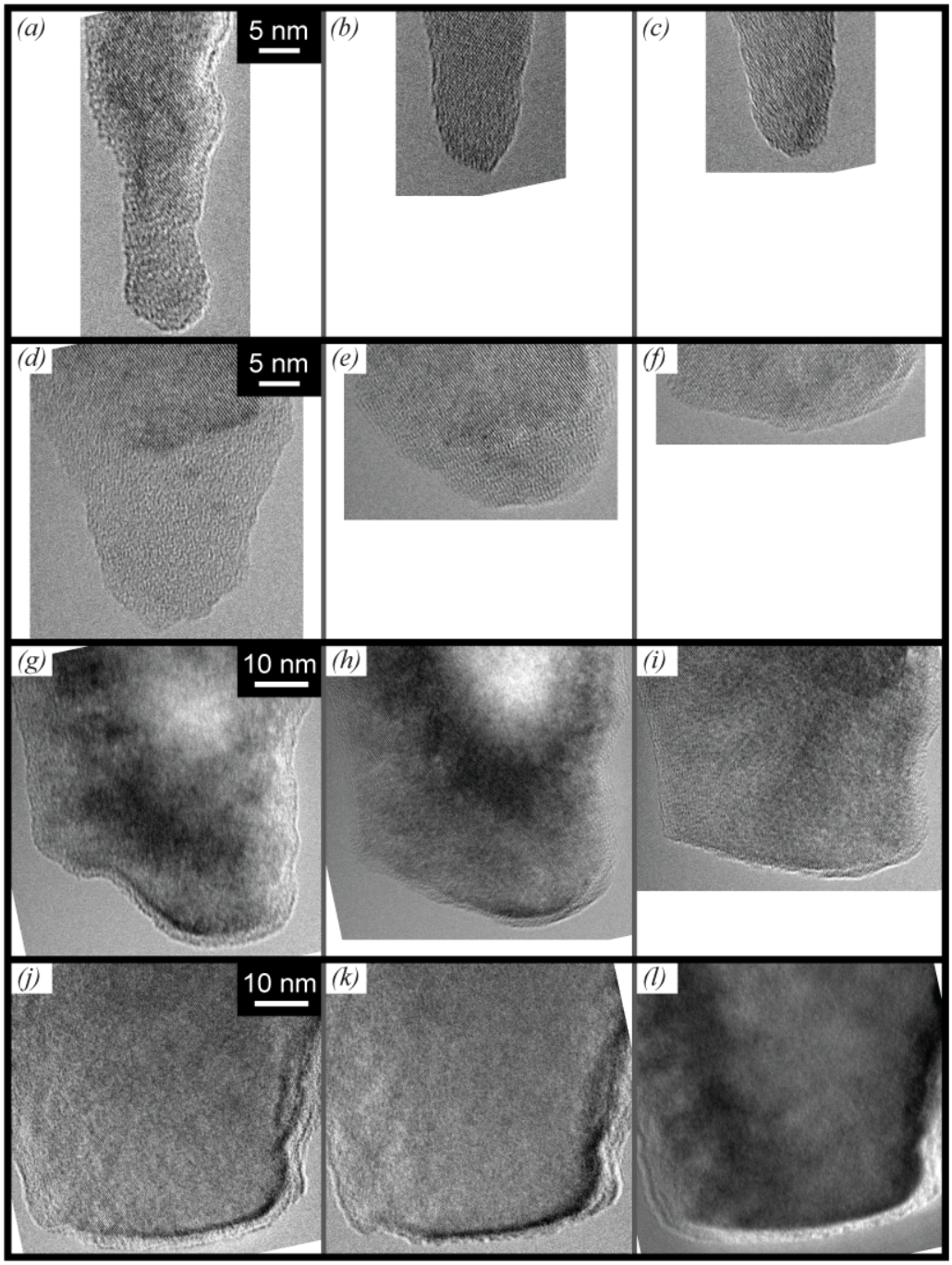

Figure 7.1: *In situ* sliding wear tests were performed on four silicon tips of varying geometries. TEM images of four silicon asperities are shown immediately prior to wear testing (left), at the approximate mid-point of testing (center), and after the conclusion of the test (right). Total sliding distances of each probe are: (a) 700 nm; (d) 3200 nm; (g) 4900 nm; (j) 200 nm. Images for each probe are *approximately* vertically aligned so surface recession can be estimated. Quantitative alignment to calculate volume loss is done on traced contours (Sect. 3-4-6).

To supplement the direct visual inspection of tip images, the outer profiles of the tips were traced at every separation point throughout the wear test, as shown in Fig. 7.2. These profiles are aligned and overlaid (as discussed in Chapter 3) to examine and quantify the changes in geometry with sliding. In the present testing, sliding was used to wear through the outermost oxide, and then to continue wearing into the single crystal silicon. Clear differences were observed in the wear behavior of these two materials. The single crystal silicon wore gradually. There was no evidence of fracture, as evident from the solid traces of Fig. 7.2. In all cases involving wear of pure silicon, the change from one profile to the next is gradual and relatively uniform, without evidence of fracture. The distance of profile recession varied for different scan lengths, but in many cases was 1 nm or less. Even allowing for the possibility of fracture events that were undetected, the total distance of recession puts an upper bound on the size of fractured pieces of typically 1 nm and often less.

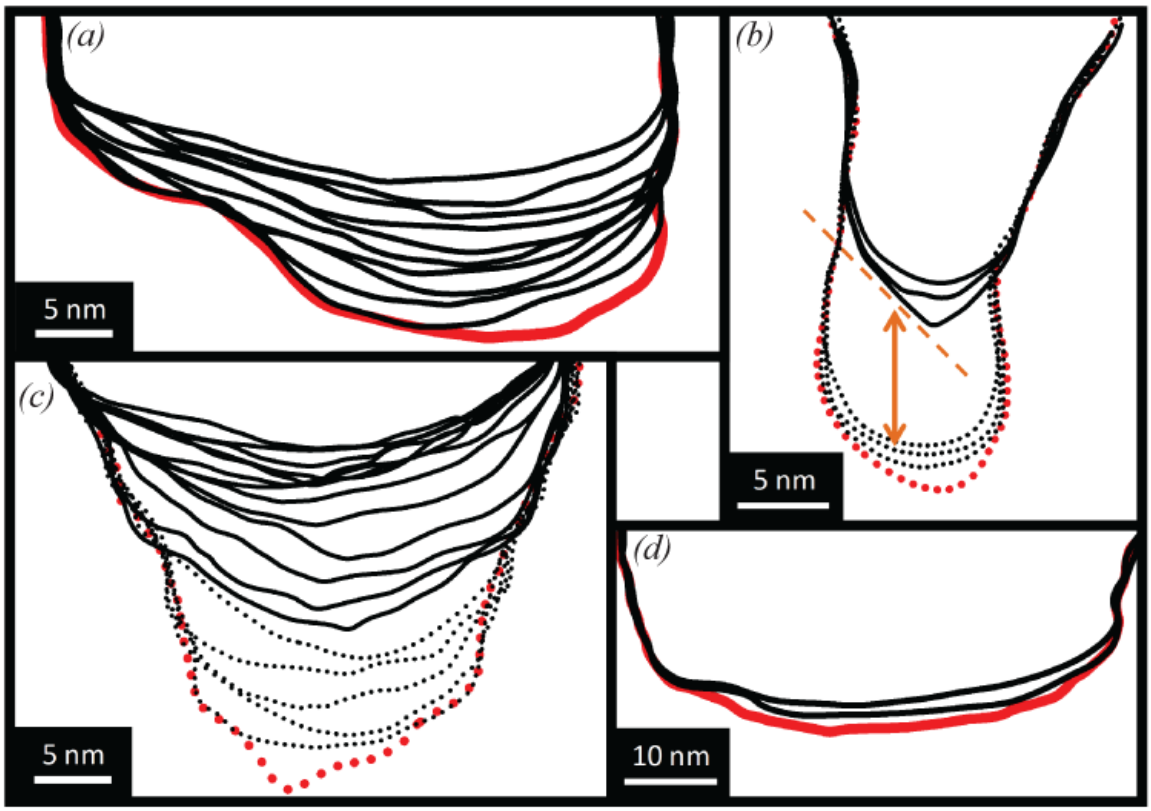

Figure 7.2: Overlaid traces show that silicon wear is gradual. Initial profiles (red) and subsequent (black) profiles have been overlain to show the evolution of the tip over the course of testing. Solid lines indicate that the wearing material is crystalline silicon (as determined through TEM imaging); dotted lines indicate wear of the initially-present oxide. For tips shown in (a) and (c) the oxide was removed in the TEM during tip alignment, before images and videos were saved. Sliding intervals for the silicon correspond to the spacing of points on the *x*-axis in Fig. 7.4 (silicon) and 7.6 (silicon oxide). In only one case (during wear of oxide) is there clear evidence of fracture (in (b), orange arrow), demonstrated by sudden removal of a larger amount of material with evidence of a preferred crystallographic plane different from the sliding plane. Figure reproduced with permission from Ref. (*2*).

Further, the perfect silicon crystalline lattice arrangement was often observed to extend to within a nanometer of the surface, even in highly worn regions, as shown in the lattice-resolved images of several different worn tips shown in Fig. 7.3. (Note that the structure of the outermost atomic layers is not accessible in the TEM; due to the curvature and small size of the tip, there is very little material being imaged and there is

insufficient contrast to distinguish between amorphous material (i.e. due to surface reconstruction or wear-induced disordering) and imaging artifacts (such as focusing fringes and edge effects). The thickness of this unknown region can vary depending on focus and beam conditions.) Overall, these results demonstrate that, under the selected conditions, significant wear of silicon occurs gradually and progressively without requiring fracture or plastic deformation; this material removal is directly consistent with the atomic attrition wear model (Chapter 6).

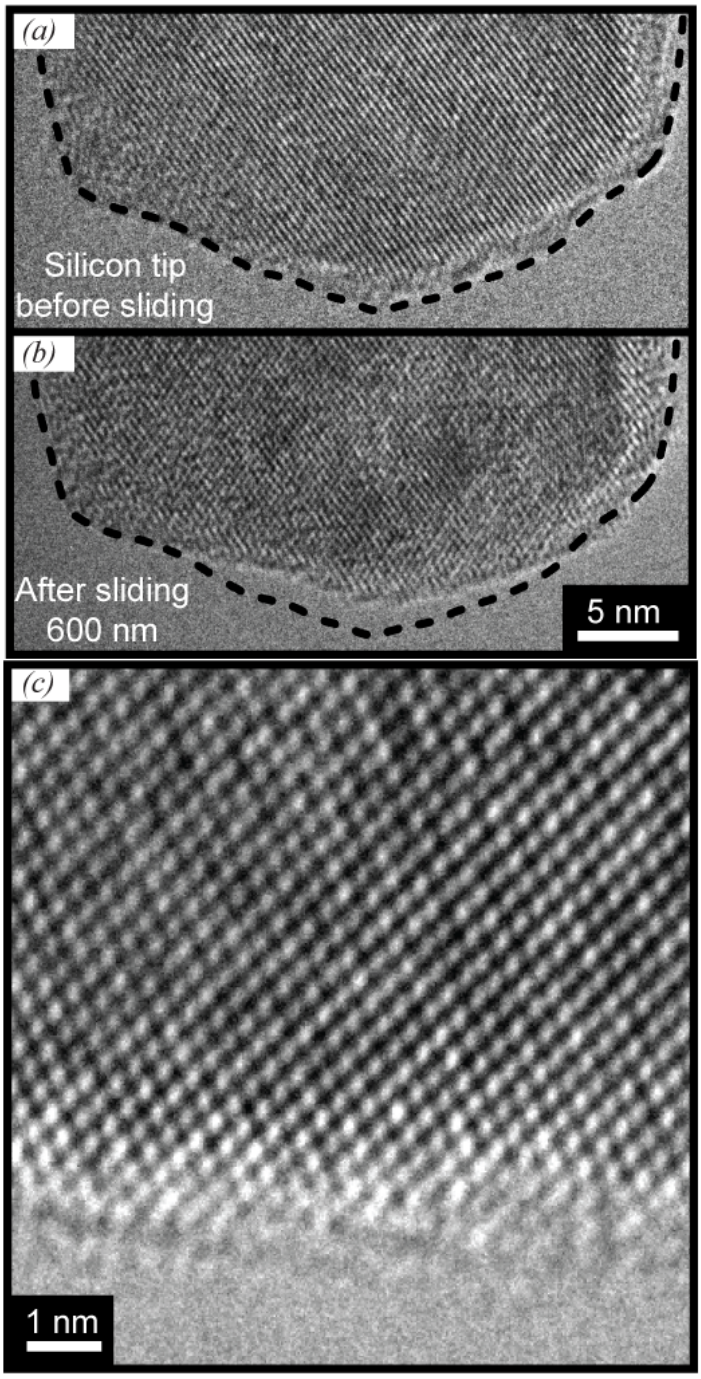

Figure 7.3: After three sliding intervals, each of 200 nm, the recession of the surface of the tip is approximately 1 nm, and the underlying lattice is undamaged. The wear was observed to be gradual and progressive, not showing sudden removal or preferred surface orientations. Additionally, a representative lattice-resolved image of the same asperity shows no evidence of dislocations or defects in the sub-surface silicon lattice, even in highly worn areas.

The one case where fracture clearly does occur is marked with an arrow in Fig. 7.2(b), and demonstrates sudden removal of a portion of the tip corresponding to roughly 7 nm of recession along the tip axis, together with a preferred crystallographic orientation of the fracture plane that is distinct from the sliding plane. This event occurred while a significant amount of oxide was still present on the tip and does not influence the analysis of subsequent wear of crystalline silicon for this tip.

In contrast to the crystalline silicon, the oxide behaved irregularly. Most frequently, it receded gradually like the silicon, as shown in Fig. 7.2(a,c-d). However, sometimes fracture occurred, as shown in Fig. 7.2(b), and other times it exhibited homogeneous deformation (plasticity). The latter behavior was most commonly observed at high beam currents – either in the 300 kV FEI microscope used at CINT or in the highest resolution images/videos taken on the 200 kV JOEL microscope at Penn. These results can be explained in the context of other previous results of the change in deformation behavior of silica under the electron beam (*3*). While silica is brittle under ambient conditions and fails by fracture, ductile behavior has been demonstrated under a sufficiently high-energy electron beam. This "superplastic deformation" is attributed not to heating, but to the generation of structural defects that allow bond reorganization and atomic-scale healing of incipient voids before they grow to a critical size for crack initiation (*3*). This explains the range of behaviors observed in silicon oxide. The now-ductile silica can simply flow plastically in an almost liquid-like fashion. Or, it can form a relatively tough bond at the interface with the diamond (or with additional silica material that has previously been transferred to the counter-surface) such that, as the cantilever is slid laterally, significant bending stresses can develop further up the high-

aspect ratio shank of the tip. These bending stresses can cause fracture in the silicon, which was never observed to become ductile by electron beam exposure. Such an event is shown in Fig. 7.2(b), where the apex of the tip was composed of oxide, while the location of fracture was located in the single crystal silicon. Finally, there were also many cases where the silicon oxide appeared to wear gradually (as shown in Fig. 7.2(c) and 7.2(b) (before fracture occurred), in accordance with an atom-by-atom mechanism. While it is possible that wear of the oxide also obeyed reaction rate theory in some cases, this analysis must be performed with caution since it is possible that multiple wear mechanisms were active simultaneously. This is discussed in more detail in Sect. 7-3

7-2: Quantifying the rate of wear of silicon and testing predictions based on reaction rate theory

In accordance with *ex situ* studies on silicon (*4*), wear progressed through the oxide and then through the underlying single crystal silicon. A principal advantage of performing wear tests with *in situ* imaging is the ability to distinguish between the wearing materials, and between different wear mechanisms. Therefore, only the wear of silicon is included in the quantitative reaction rate analysis in this section – any sliding involved in removing the oxide was excluded, and is analyzed in Sect. 7-3. There was no observable contamination on the surfaces of the tips; any contamination initially present would have been removed along with the oxide.

The volume lost for all four AFM probes was quantified by direct TEM imaging throughout the wear tests, as described in Chapter 3. Since it is expected that the

behavior and the kinetics of wear of silicon will be different from that of silicon oxide, then the two materials are analyzed separately. In the present section, the measurements and analysis are confined to the cases where the wearing material was single crystal silicon, as confirmed by direct observation in the TEM. Results are plotted against the cumulative sliding distance, as shown in Fig. 7.4(a). The volume removal rate (local slope of the data points) varied widely both for a given asperity and also amongst the four asperities. Traditionally, following the Archard law, the volume lost in a single sliding interval of a wear test is plotted *vs.* the product of sliding distance for that interval and the total normal load (in this case, adhesive force). While Archard's law is macroscopic in nature, for illustration purposes the data is presented in this way in Fig. 7.4(b). The individual datasets are clearly nonlinear with a large degree of scatter; the Archard equation cannot be used to describe the behavior. Further, widely divergent wear volumes are seen between the four asperities, thus no fundamental insight about wear is gained through an Archard-like presentation of the data.

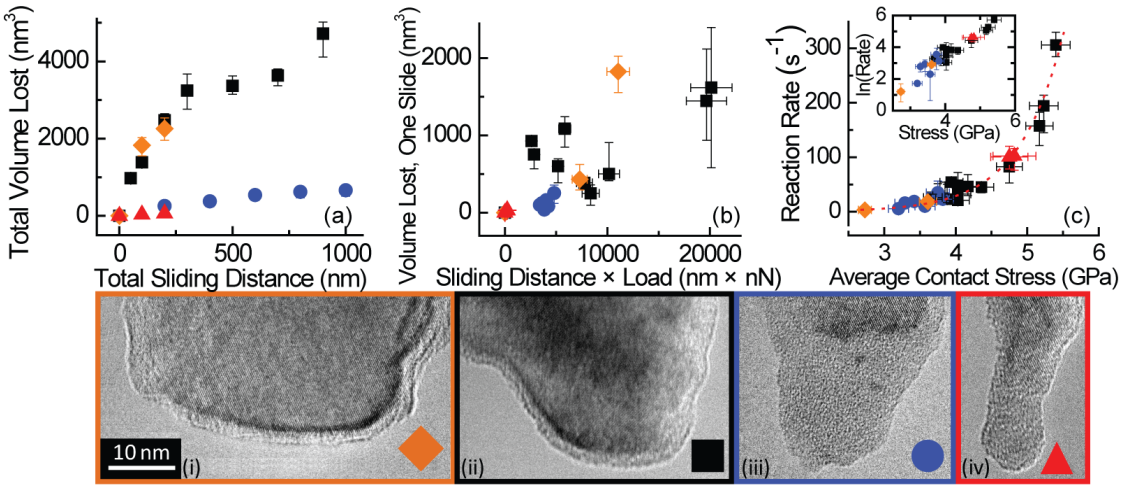

Figure 7.4: The volume of silicon lost due to wear has been quantified and is well described using a chemical kinetics framework. The cumulative volume lost due to wear is shown (a) for tests from four AFM probes for the first 1 μm of sliding (data beyond 1 μm is excluded for clarity). The distinct initial (pre-wear) geometries of the four different AFM tips are shown in TEM images (i–iv). These images are all displayed at a common magnification, and the shape and color of the corresponding data point are indicated in the image. The outer oxide layer is removed by sliding before this analysis and is not included in the measure of volume lost. To conform with the Archard equation, the data from a can be represented (b) as the volume lost in a single scan as a function of the product of the distance and load for that scan. This plot demonstrates that there is neither a linear relationship between these quantities (as predicted by the Archard equation), nor is there consistent behavior between tips. When the data for the wear of pure silicon are plotted (c) in accordance with stress-assisted chemical reaction kinetics, the four data sets collapse to a single curve that is fit well by an exponential relationship (Eq. 6.6), dashed line). Inset: the same data collapsing to a straight line on a log-linear plot. (Note that all data are included in c, not just the first 1 μm of sliding.)

Next, the data is analyzed in the context of reaction rate theory, which was presented in Chapter 6. To do this, the existing measurable quantities (geometry, volume loss, normal force, sliding velocity) must be converted into the reaction rate $k_{atom\text{-}loss}$ [s^{-1}] (the number of atoms removed per unit time in sliding contact, normalized by the number of atoms in contact) and a contact stress σ [Pa], in accordance with Eq. 6.6. The value of k_0 is assumed to be a typical lattice vibration frequency of 10^{13} s^{-1}. When this data was

previously published (*2*), a value of 10^{14} s^{-1} was used as an input value; however, since the typical phonon frequency in diamond is 3-4×10^{13} s^{-1} (*5*), then a lower value is considered more realistic and is used in the present work. Since the attempt frequency is outside of the exponential, extracted results are relatively insensitive to changes in input value.

7-2-1: Calculation of mean normal stress

It is not known *a priori* which stress component has the largest effect on the energy barrier. The mean normal stress σ_{normal} is hypothesized here to be the controlling value for this analysis based on the proposed reaction pathway presented in Fig. 6.3 where the compressive normal stress facilitates bonding across the interface. As discussed previously, the atomic wear process could be affected by other stress components, such as the local shear stress arising from interfacial friction, as proposed previously (*1*, *6*). In those prior analyses, the interfacial shear stress was assumed to possess a linear dependence on the normal stress (*7*, *8*); in such a case, a model based on σ_{normal} would describe the data equally well. Thus, although we propose a pathway depending on compressive normal stress, our analysis is general and applies to all mechanisms in which the energy barrier is modified by a stress component that is equal or proportional to the compressive normal stress. Further, while continuum contact mechanics models predict that normal stresses are spatially inhomogeneous, all compressive stresses in hard materials (DMT-limit, see Sect. 2-2-2) including the peak

value scale with the mean value. This further justifies the use of the mean normal stress for the analysis.

To calculate the mean normal contact stress and other contact parameters, a continuum contact mechanics model (Sect. 2-2-2) was used (specifically, the DMT model, as justified further below). It has been discussed previously (Sect. 2-2), that these contact mechanics models assume smooth surfaces with well-defined analytical shapes; further, it has been shown (Chapters 4-5) that these assumptions can lead to significant errors – at least in the analysis of pure adhesion tests. Therefore a brief comment is required on the rationale for using a continuum model (DMT) when analyzing wear. There are two distinct differences between wear testing and adhesion testing, which require this shift in analysis. First, it is likely that initial sub-nanometer-scale geometric fluctuations are less important in wear tests than in adhesion tests: in adhesion tests, a small local asperity may be sufficient to increase the overall separation of the bodies and thus decrease the pull-off force, whereas in a wear test, small local asperities will likely be quickly worn away, causing the whole profile to tend to smoothen during sliding contact. Second, unlike an adhesion test – where the profile is typically relatively unchanged – a wear test explicitly changes the surface profile as material is removed. Therefore, the exact instantaneous contour of the tip apex during testing is fundamentally unknowable, and the best approximation of it is given by the overall geometry of the tip, excluding local fluctuations. For these reasons, the overall tip shape is assumed to govern its behavior with respect to wear, even while instantaneous surface roughness and local fluctuations govern its adhesion (Chapters 4-5).

As discussed, the contact mechanics models require knowledge of the tip radius R_{tip}; this was measured from out-of-contact images using the manual tracing procedure described in Sect. 3-4-2, followed by the parabolic fitting described in Sect. 3-4-3. Profiles were traced up to a vertical height of roughly 5 nm, since tip/sample interaction stresses are predicted to be extremely small by this separation (see Chapter 4). Additionally, every profile was traced at least five separate times to ensure that the manual tracing routine was not introducing too much subjectivity into the measured radius. The average value of R_{tip} from these multiple traces was used in analysis, with the standard deviation as a measure of the uncertainty. Naturally, there were deviations away from the fitted parabolic shape due both to local fluctuations and due to overall tip shapes that were not perfectly paraboloidal; however these were always less than 1 nm in extent and often much less. The overall tip shapes were very well approximated by parabolas at all intervals throughout the wear tests, as shown in Fig. 7.5. Asperity shapes that remain parabolic despite large volumes of wear have also been observed in Ref. (*9*).

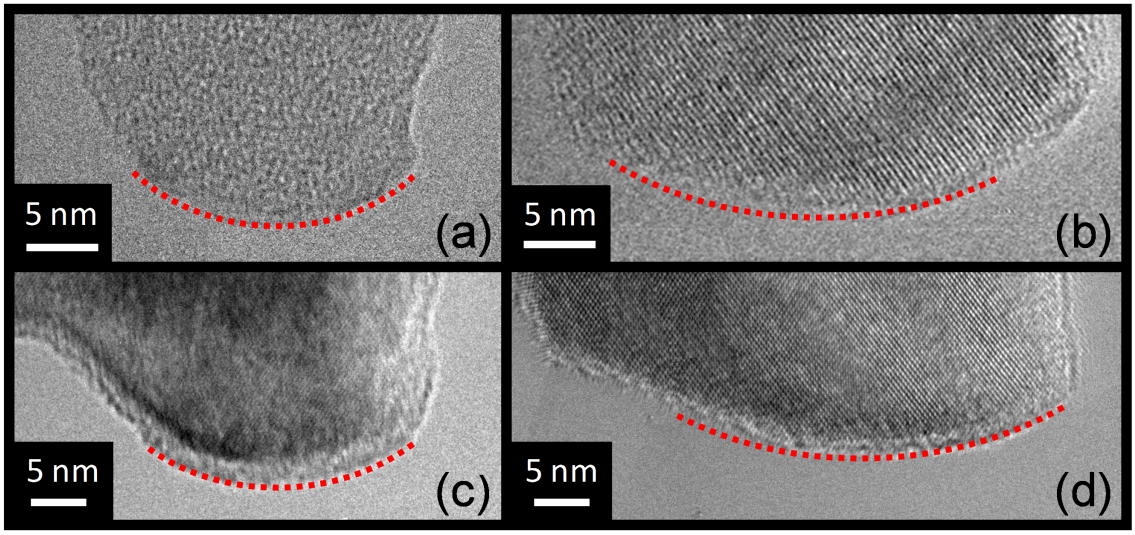

Figure 7.5: Parabolic profiles were fit to the near-tip geometry of the probe at every stage in the wear test. Tip profiles were extracted from high-resolution still images taken periodically throughout the sliding, and each profile was fit with a parabola. Two probes are shown here in their initial, pre-test states (a, c), and then the same probes are shown at the end of testing (b, d, respectively). It is clear from these representative images that the probes are well approximated by a parabola throughout the wear test.

As discussed in Sect. 2-2-2, in the DMT model, the total compressive force in the contact F_{total} is the sum of the applied load F_{applied} (zero in this case) and the adhesive load F_{adhesive}. The mean normal stress is thus calculated as:

$$\sigma_{normal} = \frac{F_{adhesive}}{A_{contact}}, \tag{7.2}$$

where $A_{contact}$ is the area of contact and is straightforwardly from the contact radius $a_{contact}$ (Eq. 2.1), and is therefore given by:

$$A_{contact} = \pi a_{contact}^2 = \pi \left(\frac{3R_{tip}F_{adhesive}}{4E^*} \right)^{2/3}. \tag{7.3}$$

The use of DMT contact mechanics is justified as the Maugis parameter (*10*) ($1.16\mu_T$, where μ_T is described in Eq. 2.7) is found to be approximately 0.3. This was calculated in a manner similar to Ref. (*11*) using literature values for elastic constants of diamond (*12*) and silicon (*13*) (specifically, $E_{diamond[100]}$ = 1050 GPa and $\nu_{diamond[100]}$ = 0.1, and $E_{silicon[100]}$ = 130 GPa and $\nu_{silicon[100]}$ = 0.28), a tip radius of 22 nm (the mean value throughout all testing), a work of adhesion of 0.66 J/m^2 and an equilibrium separation of 0.25 nm (as measured in Chapter 4). While 0.34 falls outside of the limit for DMT behavior of less than 0.1, the deviation in calculated parameters between λ=0.1 and λ=0.3 is only approximately 6% (*14*).

7-2-2: Calculation of the reaction rate

As discussed in Chapter 6, if wear is occurring in an atom-by-atom fashion, then the reaction rate $k_{atom\text{-}loss}$ [s^{-1}] can be calculated, and should have an exponential dependence on stress. Since the reaction rate is the time-rate of reaction for a single atom, it is determined by dividing the number of atoms removed by wear in a given measurement interval (N_{lost}) by the product of the number of atoms that were in contact ($N_{contact}$) and the sliding time of that interval (t_{slide}) as follows:

$$k_{atom-loss} = \frac{N_{lost}}{N_{contact} t_{slide}} = \frac{V_{lost}\rho_{Si}}{\left(A_{contact}\rho_{surf,Si(100)}\right)t_{slide}} = c\frac{V_{lost}}{A_{contact}t_{slide}}, \tag{7.4}$$

where N_{lost} is expanded as the product of the volume lost (V_{lost}) and the atomic density of silicon (ρ_{Si}), and likewise $N_{contact}$ is expanded as the product of the contact area ($A_{contact}$) and the areal atomic density of the silicon (100) surface ($\rho_{surf,Si(100)}$) (the tip's orientation

is verified by diffraction measurements in the TEM). For clarity, the density terms are collected as a pre-factor and replaced by the constant c [m^{-1}].

Equation 7.4 assumes that the rate of reaction is constant over one sliding interval. Since the radius of the tip, and thus its adhesion force and stress state, is evolving as wear occurs, this is not strictly correct. However, the sliding intervals were kept short – as low as 50 nm of sliding distance in the initial stages of wear when the tip is evolving the fastest – to minimize the error in this assumption.

This approach (calculating a rate of tip change that depends on *time*) thus predicts that for a fixed sliding distance, the volume removed will be inversely proportional to the sliding speed. To examine this, two sliding speeds were used (4 and 20 nm/s); both are included in the present analysis.

This approach is equivalent to that of Gotsmann and Lantz (Eq. 2.15) in every respect but one: Gotsmann and Lantz identified the frictional shear stress as the activating stress for wear, whereas in the present work, compressive stress is used for the reasons discussed previously. Furthermore, the shear stress can exhibit a dependence on speed (Sect. 6-3-4), and if so, that will add an additional dependence of wear on sliding speed. However, Gotsmann and Lantz's experiments were at constant speed, and thus the predicted speed dependence was not verified. There are only a few investigations into the effect of sliding speed on nanoscale wear. A speed dependence was seen experimentally for wear of a platinum tip sliding against diamond-like carbon by Bhushan and Kwak (*15*), whereby the worn volume increased roughly logarithmically with speed at low sliding speeds, then leveled off. This is in contrast with the present model and with our experimental results obtained at two speeds. However, in that work, the authors

mention that wear consists of adhesive, abrasive, and tribochemical wear, and they explicitly state that asperity fracture and particle generation occurs in their experiments, which are carried out at higher loads (50-100 nN) than the present work. Therefore, it is not surprising that a different speed dependence of wear is observed.

7-2-3: Results and discussion of reaction rate as a function of normal stress

Figure 7.4 also shows all data for the wear of silicon plotted in the context of reaction rate theory, as discussed in Sect. 6. The analysis demonstrates that an exponential dependence of reaction rate on the compressive stress clearly fits the data, consistent with the stress-assisted chemical kinetics model (Eq. 6.6). The data for all four silicon asperities, despite their widely varying geometries, collapse consistently onto a single curve, which is nearly linear when on a log-linear plot (inset in Fig. 7.4(c)). The data are extremely well-fit by Eq. 6.6 (correlation coefficient of 0.90) using ΔV_{act} and ΔU_{act} as fit parameters. Accounting for experimental uncertainty and reasonable attempt frequencies corresponding to atomic vibrations ($10^{13\pm1}$ s^{-1}), the fit yields ΔU_{act}=0.85±0.06 eV and ΔV_{act} = 6.7±0.3 $Å^3$. The activation volume corresponds to a barrier reduction of approximately 0.04 eV/GPa. These values are consistent with single atom dimensions and bond energies, and agree well with quantum mechanical predictions for stress-assisted chemical reactions in silicon – activation energy of 0.70 eV, with a stress-dependent reduction of 0.05 eV/GPa (Eq. 3 of Ref. (*16*), in the range of stress relevant to this investigation).

In comparing to previous work on tip wear, the energy barrier compares favorably to the value previously measured by Gotsmann and Lantz, 0.98 eV (*1*). However, our measurement of activation volume cannot be directly compared in a meaningful way to that study. In that work, the interfacial shear stress was assumed to be rate-controlling and to scale linearly with compressive stress (with proportionality constant ξ, as specified in Eq. 3 of Ref. (*1*)). The best-fit value extracted was $\xi \Delta V_{\text{act, shear stress}}=55\pm35$ Å^3. Comparing that activation volume to the present one is complicated by the fact that ξ is unknown and the silicon-polymer shear stress occurring in dry air or nitrogen for the experiments in Ref. (*1*) will be far different than the diamond-silicon shear stress in vacuum in the present tests. Several other differences, including assumptions about the tip geometry as it evolves, the assumption of direct proportionality between the pull-off force and the radius of the flattened tip, and different sliding speeds, render it uninformative to directly compare these activation volumes. Further experimental and simulation work is needed to identify the specific stress components responsible for reducing the relevant energy barrier in a particular set of conditions.

The specific unit process(es) leading to wear remain undetermined as the present *in situ* methodology does not resolve the behavior of individual atoms. One feasible process is a one illustrated in Fig. 6.3, whereby the rate-limited step is the formation of an atomic bond across the interface. As mentioned, this is supported by molecular dynamics simulations of diamond-like carbon sliding over diamond (*17*). The rate-limiting reaction for wear is further hypothesized to be the formation of the bond across the interface, and thus the extracted activation parameters describe the kinetics of this reaction. The values of the kinetic parameters obtained (energy barrier, activation volume) are consistent with

this picture. There are certainly many secondary events that will occur, including re-transfer of material back to the tip, surface reconstruction, diffusion, removal of groups of atoms, and so on, but the clear single-exponential behavior seen in Fig. 7.4 suggests that one mechanism dominates and controls the rate of wear.

7-3: Quantifying the rate of wear of silicon oxide

The kinetics of wear of the oxide must be analyzed with significantly more caution than was used when analyzing the wear of the silicon (Sect. 7-2). Not only has the deformation behavior of silicon oxide been demonstrated to be affected by the electron beam, but also there is clear evidence of both fracture and plastic deformation occurring (Sect. 7.1). For the present analysis, clear cases of fracture and gross shape change were excluded from the data and only cases that *appeared to be* consistent with gradual atom-by-atom removal were calculated.

Using the same analysis described in Sect. 7-2, the wear behavior of silicon oxide was analyzed in the context of reaction rate theory, as shown in Fig. 7.6. The results show a consistent super-linear dependence of reaction rate on stress, and may be consistent with exponential behavior. A fit to the data yields an activation energy $\Delta U_{act} = 1.38 \pm 0.16$ eV and an activation volume $\Delta V_{act} = 27 \pm 5.6$ Å^3. However, compared to the data for silicon, there is significantly more scatter in the data, fewer data points because there is a limited amount of oxide to wear through, and a narrower range of stress was explored. For these reasons, the exponential trend is not as clear and the uncertainty of extracted activation parameters is much larger.

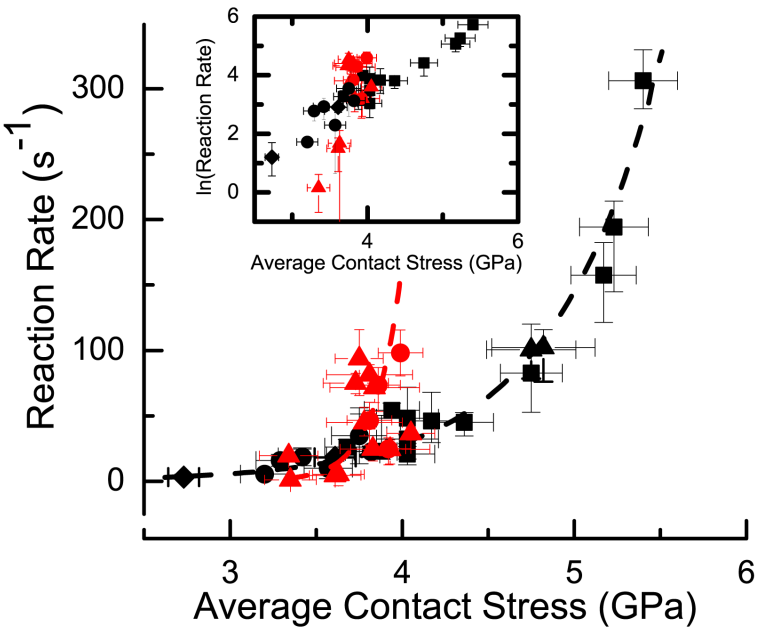

Figure 7.6: The wear data for silicon oxide can also be analyzed for those intervals where it appeared to be gradual. The measured wear data was analyzed using the method described in Sect. 7-2 and is shown in red above. The data from silicon (Fig. 7.4) is presented in black for comparison.

Despite the concerns mentioned above regarding the range of measurements for silicon oxide wear, the comparison between the silicon and silicon oxide behavior demonstrates the importance of understanding the underlying kinetics of wear and of measuring the activation parameters for a given system. The rate of wear of the oxide is lower than for Si at low mean contact stresses, but crosses over to a higher rate at approximately 3.6 GPa. From fitting the data, the calculated stress-free activation barrier is higher than for Si. This may naively seem to indicate that silicon oxide is a more wear-resistant material than silicon. However, the activation volume is larger, indicating that the energy barrier (and thus the wear rate) is much more sensitive to stress than for silicon. This is why there is a stress at which the two data sets cross, and at all higher stresses, the wear of the oxide is significantly faster. The knowledge of the activation

parameters allows the calculation of this behavior and the selection of the more appropriate material given the design stresses.

7-4: Conclusions

This chapter described a set of experiments in which the wear was carefully measured and analyzed in the context of reaction rate theory. There are two major advances provided by the present investigation. First, the *in situ* nature of this testing provides direct experimental evidence that significant nanoscale wear can occur in the absence of fracture or plastic deformation. This implies that atomic attrition can be quite significant in nanoscale contacts, and potentially a substantial wear mechanism at the micro-/macro-scale, even in brittle or ductile materials that fail by other means at higher stresses. Second, the atomic reaction rate has been directly calculated and plotted versus contact stress, explicitly demonstrating an exponential dependence over decades of reaction rate. This provides direct experimental validation for an atom-by-atom wear mechanism, and justifies the application of reaction rate kinetics in the analysis and prediction of some types of nanoscale wear. More broadly, when wear is being studied for a new set of materials or conditions, Figs. 7.4 and 7.6 provide examples of the analysis that can be performed to determine whether reaction rate theory is appropriate. Reliable values for the kinetic parameters from that analysis could then be used to predict wear for different loads and tip geometries.

7-5: References

(1) Gotsmann, B.; Lantz, M. A. Atomistic wear in a single asperity sliding contact. *Phys. Rev. Lett.* **2008**, *101*, 125501.

(2) Jacobs, T. D. B.; Carpick, R. W. Nanoscale wear as a stress-assisted chemical reaction. *Nature Nanotech.* **2013**, *8*, 108–112.

(3) Zheng, K.; Wang, C.; Cheng, Y.-Q.; Yue, Y.; Han, X.; Zhang, Z.; Shan, Z.; Mao, S. X.; Ye, M.; Yin, Y.; Ma, E. Electron-beam-assisted superplastic shaping of nanoscale amorphous silica. *Nat Commun* **2010**, *1*, 24.

(4) Chung, K.; Lee, Y.; Kim, D. Characteristics of fracture during the approach process and wear mechanism of a silicon AFM tip. *Ultramicroscopy* **2005**, *102*, 161–171.

(5) Pan, L. S. *Diamond: electronic properties and applications*; Kluwer Academic Pub, 1995; Vol. 294.

(6) Bhaskaran, H.; Gotsmann, B.; Sebastian, A.; Drechsler, U.; Lantz, M. A.; Despont, M.; Jaroenapibal, P.; Carpick, R. W.; Chen, Y.; Sridharan, K. Ultralow nanoscale wear through atom-by-atom attrition in silicon-containing diamond-like carbon. *Nature Nanotech.* **2010**, *5*, 181–185.

(7) Mo, Y.; Turner, K. T.; Szlufarska, I. Friction laws at the nanoscale. *Nature* **2009**, *457*, 1116–1119.

(8) Briscoe, B.; Evans, D. The shear properties of Langmuir-Blodgett layers. *Proc. Roy. Soc. A* **1982**, *380*, 389–407.

(9) Liu, J.; Notbohm, J. K.; Carpick, R. W.; Turner, K. T. Method for characterizing nanoscale wear of atomic force microscope tips. *ACS Nano.* **2010**, *4*, 3763–3772.

(10) Maugis, D. Adhesion of spheres: the JKR-DMT transition using a Dugdale model. *J. Coll. Int. Sci.* **1992**, *150*, 243–269.

(11) Grierson, D.; Flater, E.; Carpick, R. Accounting for the JKR-DMT transition in adhesion and friction measurements with atomic force microscopy. *J. Adhes. Sci. Technol.* **2005**, *19*, 291–311.

(12) McSkimin, H. J. Elastic Moduli of Diamond as a Function of Pressure and Temperature. *J. Appl. Phys.* **1972**, *43*, 2944.

(13) McSkimin, H. J. Measurement of Elastic Constants at Low Temperatures by Means of Ultrasonic Waves–Data for Silicon and Germanium Single Crystals, and for Fused Silica. *J. Appl. Phys.* **1953**, *24*, 988.

(14) Carpick, R. W.; Ogletree, D. F.; Salmeron, M. A general equation for fitting contact area and friction vs load measurements. *J. Coll. Int. Sci.* **1999**, *211*, 395–400.

(15) Bhushan, B.; Kwak, K. J. Velocity dependence of nanoscale wear in atomic force microscopy. *Appl. Phys. Lett.* **2007**, *91*, 163113.

(16) Zhu, T.; Li, J.; Lin, X.; Yip, S. Stress-dependent molecular pathways of silica–water reaction. *J. Mech. Phys. Sol.* **2005**, *53*, 1597–1623.

(17) Gao, G.; Mikulski, P.; Harrison, J. A. Molecular-scale tribology of amorphous carbon coatings: effects of film thickness, adhesion, and long-range interactions. *J. Am. Chem. Soc.* **2002**, *124*, 7202–7209.

CHAPTER 8: Conclusions and future work

The present set of investigations used studies performed inside of a transmission electron microscope to add previously inaccessible information – real-time, *in situ* measurement of the tip geometry – to the analysis of adhesion and wear. Although the apparatus used cannot resolve the behavior of individual atoms, visualization of the sub-nanometer-scale contact geometries and observation of the sub-surface atomic lattice enables novel, atomic-level insights into adhesion and wear to be gained. In this final chapter, the most relevant results regarding adhesion and wear will be briefly reviewed in Sect. 8-1, along with the perceived impact of the work in those specific fields. Section 8-2 presents larger conclusions that emerge from the work as a whole regarding the relevance of atomic-scale detail to all of nanotribology, and potentially to other areas of surface science. Finally, Sect. 8-3 presents significant questions opened or left open by the present work, followed by suggested future investigations into these.

8-1: Summary of results from nanoscale adhesion and wear, and broader impacts on those fields

8-1-1: The measurement of fundamental parameters governing adhesion

Significant prior work had demonstrated models for adhesion of continuum bodies and characterized the effect of roughness on adhesion for planar surfaces; the objective of the present investigations was to provide insight on nanoscale contacts – including the applicability of models, and the identification and measurement of relevant

parameters. Adhesion tests were performed with *in situ* high-resolution visualization of both sides of the contact. While the adhesion *parameters* (i.e. pull-off force and snap-in distance) could have been measured using a traditional atomic force microscope, the concurrent measurement of the detailed contact geometry allowed a previously unattainable analysis of adhesion in these contacts.

First, in Chapter 4, a method for integrating a surface interaction potential over measured sub-nanometer-scale topography was presented. This allowed the simultaneous computation of the strength and the length-scale of the adhesive interaction in one particular system (silicon in contact with diamond); this has not previously been experimentally possible for *any* system. Results validated previous estimates of the range of adhesion, while showing that previous measurements significantly underestimated the work of adhesion between silicon and diamond by failing to account for nanoscale roughness. Second, Chapter 5 described generalizing results beyond the measured geometries of a few probes to understand how adhesion is affected by atomic-scale surface roughness. Using adhesion tests between a diamond surface and probes of either diamond-like carbon or ultrananocrystalline diamond, this work demonstrated that even sub-nanometer-scale roughness on a curved asperity is sufficient to reduce measured values of work of adhesion by an order of magnitude below those of atomically smooth asperity surfaces. It further suggested a simple functional form to obtain a reasonable estimate of dependence of this reduction on the amplitude of the roughness. In sum, these results demonstrate methodology for the measurement of adhesion parameters for technologically relevant materials, and demonstrate how the strength of adhesion is

affected by nanoscale physical properties: adhesion range, tip shape, and surface roughness.

More broadly, these investigations demonstrate not only significant weaknesses in the typical treatment of nanoscale adhesion, but also enable pathways towards better understanding and even control of adhesion in the future. This investigation has shown that the present state-of-the-art method for measuring the work of adhesion – measurement of the pull-off force using an atomic force microscope probe of known radius, followed by calculation of work of adhesion using continuum contact mechanics (Eq. 2.5 or 2.6) – can be in error by a factor of ten because it fails to account for probe roughness. This extends prior continuum level studies (*1*, *2*) to the nanoscale, and demonstrates how theory from flat-flat contacts can be modified to apply to contacts using a nanoscale asperity. This presents an opportunity: the nanometer- and sub-nanometer-scale roughness on sharp asperities can be *designed in* to NEMS devices or probe-based nanomanufacturing techniques in order to minimize adhesion in cases where it is undesirable. Potential recipes are demonstrated for rationally choosing a surface topography – either by integrating a surface potential to predict adhesive forces, or by using the empirically supported equation for adhesion as a function of root-mean-square roughness (Eq. 5.4). Finally, while the integration of a surface potential to predict adhesive forces has only been demonstrated here for single asperity contacts, there is no fundamental reason preventing this method from being generalized to planar nanoscale contacts as well.

8-1-2: Concluding remarks on nanoscale wear

Significant prior work on nanoscale wear using the atomic force microscope had suggested atom-by-atom material removal and an exponential dependence on load or stress in the contact; however, these relied on significant assumptions about the mechanism and kinetics of material removal and lacked sufficient resolution to prove these. To address these, wear tests were performed in the present investigation using direct *in situ* visualization to concurrently characterize the detailed conditions under which sliding occurred and the evolution of the surfaces during that sliding. First, Chapter 6 presents the application of reaction rate theory to nanoscale wear, along with the basic assumptions, considerations, and interpretation of parameters. Based on this, a variety of investigations are suggested to establish the theory more firmly and extract useful quantities – one of these suggested investigations has been performed in the present work and is presented in Chapter 7. Here, nanoscale wear is characterized for silicon sliding against diamond in vacuum at low loads. The shape-evolution and kinetics of wear are well described using this framework of stress-assisted chemical reactions. Therefore, the fundamental parameters governing wear of silicon under these conditions were measured. These measurements have direct relevance for predicting lifetimes of silicon components in contact microscopy, such as AFM, and in certain device applications, such as probe-based data storage or probe-based nanomanufacturing.

More broadly, this work demonstrates a framework for predicting and controlling wear more generally. The reaction-rate analysis leads to specific considerations for selection or design of wear-resistant materials: not only must they possess high activation energies for atomic removal (ΔU_{act}), but equally important is a low activation volume

(ΔV_{act}) so that the barrier is not easily overcome in loaded conditions. In principle, the measurement of these two parameters enables the prediction of wear, at least in conditions where the underlying mechanism is unchanged, and the rational design of nanoscale devices, components, and sliding conditions to minimize wear. While the present work only investigates the behavior of a single nanoscale asperity, in many cases larger-scale contact is composed of such asperities, as discussed in Chapter 1. The equations and frameworks governing nanoscale wear in dry sliding contacts are not expected to apply *directly* to describe wear in micro- and macro-scale contacts, which are often rough and sometimes lubricated. However, these laws could be used as inputs into larger-scale models, such as those describing multi-asperity surfaces or the "boundary lubrication" regime, to describe the behavior of those portions of the surfaces that are in intimate contact during sliding.

8-2: Emergent conclusions from the work as a whole: Capturing the effect of atomic-scale detail

In addition to the conclusions that apply to the topics of adhesion and wear that were described above, there are two broad conclusions with potential application to all of nanotribology, and possibly to the wider topic of surface science at the nanoscale.

The first broad conclusion, drawn from these adhesion investigations, is that atomic-scale topography and atomic-scale reactions can have a significant effect on the behavior of the bodies in contact. For instance, the common assumption that a nanoscale AFM tip can be approximated by an analytical function has been shown to cause

significant errors in the measurement of adhesion parameters. Also, significant material removal and even shape change of nanoscale components can result from the action of individual atomic-scale bond-rearrangement. This conclusion of the importance of nanoscale structure and behavior has already been established using molecular dynamics simulations (Sect. 2-2-1); however, it has not been as clearly characterized in experimental investigations. The present work leverages real-time visualization of the contact to bridge the gap between nanotribological investigations performed using atomistic simulations and those performed using traditional experimental techniques (such as the atomic force microscope or the surface forces apparatus).

The second broad conclusion is that, while atomic-scale details cannot be ignored, there are generalizations that provide guidance in cases where the omniscience of atomistic simulations is not possible. For example, as mentioned, the modeling of an AFM tip as a smooth paraboloid will yield errors in the measurement of adhesion parameters. However, realistic measurement of the same adhesion parameters *can* be achieved using a hybrid continuum-scale/nanoscale approach, in which a surface interaction potential was integrated over the measured sub-nanometer-scale geometry of a real tip. The use of a surface interaction potential is a continuum concept that relies on significant assumptions (see Sect. 2-2-3), yet in this thesis is applied to measured nanoscale contacts and enables the accurate prediction of adhesive forces. This approach – the integration of stresses between contours – is a blunt instrument compared to the *summation* of *forces* between *atoms* that is commonplace in computer simulations. Yet excellent agreement between these techniques is achieved in two different sets of testing: in the comparison of the experimentally-determined range of adhesion (z_0) against the

value calculated based on constants from a well-established molecular dynamics potential (using the method discussed in Sect. 4-3-1); and in comparing observed trends of adhesion and roughness between numerical models (Fig. 5.1) and experiment/MD simulations (Fig. 5.6). It must be noted that, in all cases, the experimentally measured values yielded much higher degrees of scatter as compared to the atomistic approaches – it is left to further investigations to determine whether this is due to real changes in contact surfaces (with time or contact location), or whether this is caused by inaccuracies in the analysis approach.

Another example of generalizations of trends in adhesion that do not require full atomic-scale knowledge of the contact geometry is the demonstrated utility of root-mean-square probe roughness in predicting adhesion between silicon probes and a diamond surface. The root-mean-square (RMS) roughness is a calculated quantity that depends on the statistics of an entire surface; it is does not accurately describe the detailed geometry at the very apex of the probe (the only region that actually comes into direct contact). Mathematically, it can be shown that a wide variety of surfaces can share a single RMS roughness value. For these and other reasons, there is no reason a priori to assume that RMS roughness should be a useful metric for nanometer-sale probes. Yet, the combination of *in situ* experiments and atomistic simulations demonstrate consistent and monotonic changes in pull-off force (and thus measured work of adhesion) as a function of this parameter. Similar to the approach described in the previous paragraph, using RMS roughness to describe adhesion represents a hybrid continuum-scale/nanoscale approach – a nanoscale contour is used as an input, but the detailed geometry is averaged

out using the equation for RMS roughness, which fundamentally assumes a continuous, well-defined surface.

In summary, there are certain cases of contact – e.g. freshly cleaved, single-crystal, experimental surfaces in vacuum; or a fully-equilibrated contact pair created using a robust atomistic simulation – in which perfect knowledge of atomic positions is enjoyed. However, in a far larger number of cases – e.g. an atomic force microscope tip on a surface in dry air, or a finite element model of a MEMS component – in which atomic-scale knowledge is unattainable. The present work attempts to bridge the gap between these two sets of cases, and demonstrates three specific examples of how nanoscale and atomic-scale details might be incorporated: (1) a surface potential can be integrated over known (or estimated) surface geometry to calculate total adhesion forces; (2) the reduction in adhesion with surface roughness can be estimated based on known or estimated values of root-mean-square surface roughness; (3) atom-by-atom wear in regions of intimate contact, which can be the dominant mode at low loads and may still persist at high loads when plasticity and fracture also occur, can be predicted using the formalisms of reaction rate theory and known or estimated values of activation parameters.

8-3: Open questions and suggested future work

8-3-1: Open questions from the present investigation

A major question left open by the present analysis is the limits of the applicability of continuum concepts to nanoscale surfaces. There were several cases where

continuum-level concepts were applied – e.g.: the use of a surface potential to calculate stresses in Chapter 4; the calculation of root-mean-square roughness in Chapter 5; the computation of contact area using a continuum model in Chapter 7 – and in all of these cases, the computed results agreed well with theory or molecular dynamics simulations. However, previous atomistic simulations have discussed deviations from continuum predictions (*3*), and the complication of even calculating a reliable value for contact area (*4*). Thus, continuous concepts likely cannot be applied in all cases, and therefore future study is required to define the limits of applicability, including size and shape of the bodies, load and deformation of the contact, materials, environment, etc. Further, in cases of nanoscale contacts where continuum-level predictions do apply, an important question is *why do they apply so well*, given that many assumptions of continuum-based theory are violated.

More focused questions involve the general limits of applicability of particular equations for adhesion and wear that were discussed in this thesis. Specifically, Chapter 5 demonstrates the applicability of a previously proposed model of effective work of adhesion as function of tip roughness (Eq. 5.3). However, this model assumes that the roughness is on the surface (not the tip), that only van der Waals adhesion is acting, that all bodies are rigid, and that the actual roughness can be distilled to a single parameter: RMS roughness. This approach should not apply, for example, to soft materials outside of the Bradley or DMT limit, and should not accurately capture multiscale roughness. These limits must be explored further. Additionally, Chapter 7 demonstrates that the rate of wear varies exponentially with average normal contact stress. However, as discussed in Chapter 6, there remain significant questions about

which specific stress component(s) governs the wear event, and *why* it scales with average normal contact stress. In particular, the continuum model used to interpret that data predicts that stress is non-uniform inside the contact. One therefore expects that regions of high stress should contribute significantly more to overall wear than regions of low stress. However, this is not easily captured in an analytical model: the faster wear of these high-stress regions reduces the local stress, shifting the load to other regions, thus increasing the stress elsewhere and causing those regions to wear more quickly. The result is a dynamically evolving system that requires numerical modeling. Therefore, further experimental investigations is suggested, especially in conjunction with atomistic, finite element, and/or other simulation techniques as discussed in Sect. 6-3.

8-3-2: Suggested future work

Due to experimental constraints of the TEM, this work was focused on the adhesion and wear of single-asperity contacts of a relatively small number of materials. While the specific conclusions about those materials are well-supported, the applicability of the broad conclusions and application to more complex geometries and to other material systems must be extensively studied and demonstrated.

A straightforward extension of this work would be to investigate single asperity contacts of other materials. Atomic force microscope probes are inexpensive and easily obtained; they can be purchased commercially with a wide variety of coatings and they can also be easily coated with any conformal thin film. This renders the present technique ideal for investigation of a wide range of scientifically-relevant or

technologically-relevant films. However, a significant limitation arises due to the use of the transmission electron microscope, which requires probes to be conductive, non-magnetic, robust to electron-irradiation, and electron transparent (i.e. thin in the transverse dimension). This eliminates entire classes of materials including most polymers (non-conductive, beam-sensitive), many steels (magnetic), many amorphous oxides (at least somewhat beam-sensitive), and any films that cannot be deposited with less than ~100 nm thickness. Fortunately, rapid advancement of TEMs and the development of novel imaging conditions are constantly advancing the frontier of materials that can be imaged. For instance, using ultra-low-dose techniques, it is becoming feasible to image many polymers and even some biological materials.

A useful extension of the present investigation would involve combination with other *in situ* capabilities. For instance, a logical extension of the wear testing involves heating and/or cooling the contact to explore changes in the reaction kinetics. The stress-assisted thermally activated wear process should have a characteristic (Arrhenius) dependence on temperature, and performing measurements as a function of temperature should enable more robust and accurate determination of stress-free energy barriers. Additionally, adhesion could be explored in combination with electrical current passing through the contact. This would serve both to simulate typical mechanical switching elements used in NEMS/MEMS devices and would provide a second, independent measure of contact area. Finally, environmental species could be introduced into the TEM (using environmental TEM techniques) to simulate more realistic conditions than ultra-high vacuum and to determine the effect of ambient species such as oxygen or water on the chemical reaction process.

The most exciting extension of the present techniques explores the fundamental behavior of contact mechanics at the nanoscale. As reviewed in Sect. 2-2-2, there are clearly defined predictions from continuum contact mechanics for the contact stress, contact area, and body deformation as a function of load. As discussed in the same chapter, these predictions have been shown to break down for the very smallest contacts, particularly with certain surface structures. These represent limiting cases of behavior under extremes of contact size. However, there is also a wide range of intermediate cases where continuum contact mechanics *may* apply accurately, or where it applies with slight modifications – such as generalizations of behavior of atomistic surfaces (gleaned from simulations or experimental investigations such as the present one). The advancements in nanoscale and *in situ* experiments in parallel with the rapid expansion of computing power and the accuracy of large-scale atomistic simulations are finally making it possible to explore the basic questions of how to define contact at the atomic-scale and how to describe the physics that governs it.

8-4: References

(1) Fuller, K.; Tabor, D. Effect of surface-roughness on adhesion of elastic solids. *P Roy Soc Lond A Mat* **1975**, *345*, 327–342.

(2) Maugis, D. On the contact and adhesion of rough surfaces. *J. Adhes. Sci. Technol.* **1996**, *10*, 161–175.

(3) Luan, B.; Robbins, M. O. The breakdown of continuum models for mechanical contacts. *Nature* **2005**, *435*, 929–932.

(4) Cheng, S.; Robbins, M. O. Defining contact at the atomic scale. *Tribol. Lett.* **2010**, *39*, 329–348.